

The objective of this thesis is to elucidate the femtosecond dynamics of coupled low-energy excitations in both strongly correlated materials and artificially engineered quantum structures. By means of near-infrared pump/multi-THz probe spectroscopy and a series of technological innovations (a novel collinear four-pass Ti:Sapphire amplifier and shot-noise reduced electro-optic sampling), fundamentally new insights into the many-body physics of two representative strongly correlated materials are obtained:

- It is clarified which microscopic mechanisms underlie the formation of the charge density wave in the transition-metal dichalcogenide titanium diselenide ($1T\text{-TiSe}_2$).
- A study of the high-temperature superconductor YBCO reveals that there exists no temporal hierarchy between electron-electron and electron-phonon scattering processes in this system.

Furthermore, non-adiabatic activation of ultrastrong light-matter interaction between a tailor-cut photonic resonance and an electronic excitation is realized and studied on a sub-cycle timescale. This further paves the way towards the observation of novel quantum-electrodynamical phenomena.

Michael Porer

Michael Porer

Ultrafast low-energy dynamics of strongly correlated systems

Ultrafast low-energy dynamics of strongly correlated systems



Universität Regensburg
Institut für Experimentelle und Angewandte Physik
Lehrstuhl Huber

Ultrafast low-energy dynamics of strongly correlated systems



DISSERTATION
ZUR ERLANGUNG DES DOKTORGRADES DER NATURWISSENSCHAFTEN
(DR. RER. NAT.)
DER FAKULTÄT FÜR PHYSIK DER UNIVERSITÄT REGENSBURG

VORGELEGT VON
MICHAEL Porer
AUS GARMISCH-PARTENKIRCHEN
IM JAHR 2014

Das Promotionsgesuch wurde eingereicht am 06.06.2014

Die Arbeit wurde angeleitet von: Prof. Dr. Rupert Huber

Prüfungsausschuss: Vorsitzender: Prof. Dr. John Schliemann
1. Gutachter: Prof. Dr. Rupert Huber
2. Gutachter: Prof. Dr. Sergey Ganichev
weiterer Prüfer: Prof. Dr. Christian Schüller

Contents

1. Introduction	1
2. Ultrafast multi-terahertz spectroscopy	9
2.1. The Ti:sapphire amplifier system	9
2.1.1. The cavity-dumped Ti:sapphire oscillator	11
2.1.2. A novel collinear four-pass Ti:sapphire amplifier	12
2.1.3. Dispersion management	16
2.2. Femtosecond multi-THz spectroscopy	16
2.2.1. Generation and detection of phase-stable THz radiation	18
2.2.2. Two-time THz spectroscopy for pump-probe studies	22
2.2.3. Data acquisition and analysis	24
2.3. Shot-noise reduced electro-optic sampling	26
3. Transient separation of excitonic and structural order of the charge density wave in 1T-TiSe₂	33
3.1. 1T-TiSe ₂ and the family of transition-metal dichalcogenides	33
3.2. The CDW phase transition	35
3.2.1. Reconstruction of the crystal lattice and the electronic bands	35
3.2.2. Possible driving mechanisms	36
3.2.3. The infrared fingerprints of charge and lattice ordering	39
3.3. Paving the way for NIR-pump/THz-probe studies	41
3.3.1. Fabrication and properties of a thin film sample	41
3.3.2. Quantitative description of the plasma response	42
3.4. The electronic degree of freedom upon photoexcitation	44
3.4.1. Non-thermal recovery dynamics of the free carrier response	45
3.4.2. Signatures of excitonic order	47

3.4.3. The DC resistivity anomaly	51
3.4.4. Stability of the CDW gap	52
3.5. The periodic lattice deformation upon photoexcitation	53
3.6. Coupling of lattice and electronic orders	55
3.7. The results in the light of a 1D mean-field theory	59
3.7.1. Description of the model	59
3.7.2. The equilibrium phase diagram	62
3.7.3. Modeling NIR photoexcitation	63
3.8. The origin of the charge density wave in $1T$ -TiSe ₂	66
4. Phonon and quasiparticle dynamics in superconducting $\text{YBa}_2\text{Cu}_3\text{O}_{6.93}$	67
4.1. Unconventional superconductivity	67
4.1.1. A short overview	67
4.1.2. Cuprate superconductors and $\text{YBa}_2\text{Cu}_3\text{O}_{7-\delta}$	69
4.2. The spectral hallmarks of superconductivity in the dielectric response of $\text{YBa}_2\text{Cu}_3\text{O}_{6.93}$	70
4.3. Preparations for two-time THz studies	72
4.4. Phonons and quasi-particles after photoexcitation	74
4.5. Analysis of the transient phonon lineshapes	76
4.5.1. Excitation dynamics of the apex mode	76
4.5.2. Excitation dynamics of the bond-bending mode	79
4.6. Résumé: Electron-electron and electron-phonon scattering	80
5. Non-adiabatic switching of ultrastrong light-matter coupling	83
5.1. Regimes of light-matter coupling	84
5.2. A device for optical control of light-matter coupling	86
5.2.1. Design of the switchable matter excitation and the photonic mode	86
5.2.2. A switchable photonic bandstructure	90
5.3. Optical control of the light-matter coupling strength	94
5.4. Nonadiabatic switching of a photonic bandstructure	95
6. Summary and outlook	99
Appendices	103
Bibliography	115
Acknowledgments	135

Chapter 1

Introduction

Electromagnetism is one of the four fundamental interactions in nature and determines the structure of atoms, molecules and solids. On the quantum level, electromagnetic interactions between charged particles occur via the exchange of photons. Quantum-electrodynamics provides a mathematical description of this process and has proven to be one of the most accurate theories in physics. In condensed matter systems, where many charged particles (on the order of $10^{23}/\text{cm}^3$) are correlated via the infinitely ranged Coulomb potential, our understanding of the resulting many-body phenomena can be considered to be very basic, at best. Contemporary models allow one to explain many fundamental structural, magnetic and electronic properties of insulators, some semiconductors and simple metals by assuming non-interacting electrons [Kit04]. Even novel materials like graphene can be understood reasonably well from the single-particle point of view [Mor10]. The situation becomes more complicated when many-body interactions play the central role in determining the electronic, magnetic, optical, and sometimes even mechanical properties of a material [Dag05, Mor10]. In the simplest case, one particular interaction mechanism correlates electrons with each other. Already this is sufficient to yield fascinating phenomena such as BCS superconductivity [Onn11] or the spin-density-wave in elemental chromium [Faw88]. These effects are now well understood and can be modeled by incorporating the relevant electronic interaction mechanism into established single-particle models [Bar57, Faw88]. For strongly correlated materials, the situation is far less clear-cut. In these systems, the intricate low-energy electromagnetic interplay between many interacting electrons and a variety of elementary excitations, such as magnons, phonons, or excitons, often results in competing ground states with different symmetries, different macroscopic properties and different low-energy excitations. A phase transition between these ground states is often induced by slight changes to a tuning parameter,

such as temperature, pressure, or doping. Many of these phases and phase transitions bear great technological potential. Colossal magnetoresistance, an orders of magnitude change in resistivity associated with a magnetic-field-induced metal-to-insulator transition [Ram97], and high-temperature superconductivity are just two famous examples. Nonetheless, in order to exploit these phenomena for future technology, science first needs to obtain a microscopic understanding of the underlying mechanisms and to find out why it is often sufficient to slightly tune a parameter to tip the balance to favor one ground state over another. With sufficient knowledge, it may ultimately be possible to engineer systems with tailor-cut properties, e.g. an increased critical temperature for superconductivity.

These challenges call for experiments that are capable of directly accessing the underlying microscopic degrees of freedom in order to study their role in many-body interactions. Typically, the relevant elementary excitations in strongly correlated materials, such as phonons [Kli07], magnons [Hut72], intraexcitonic transitions [Lei08], and collective plasma excitations [Hub01] are resonant to far- to mid-infrared radiation with photon frequencies in the range of approximately 0.1 THz to 100 THz (1 THz = 10^{12} Hz). Other elementary excitations in the terahertz window of the electromagnetic spectrum such as internal transitions of artificial quasiparticles [Por12, Mén14] and vibrational transitions in large biomolecules [Ton07] are pivotal for many other scientific fields. In recent years, this has reliably spurred significant advances in the technology employed to study the terahertz spectral region [Lee00, Heb04, Gan05, Ton07, Kam13, Sch14, Eis14]. Fourier transform infrared spectroscopy and ellipsometry [Tom05] are widely employed time integrated techniques to study the spectral fingerprints of THz optical resonances in thermal equilibrium. However, time integrated spectroscopic approaches fail to capture the very essence of the microscopic physics in strongly correlated systems: The delicate and highly dynamical interplay of different types of elementary excitations that, in fact, occurs on femtosecond timescales ($1\text{ fs} = 10^{-15}\text{ s}$) [Ulb11]. The invention of mode-locked Ti:sapphire lasers [Spe91] together with the development of increasingly efficient emitters and detectors for THz radiation [Fer02, Ton07] paved the way for femtosecond optical-pump/multi¹-THz-probe spectroscopy. During the last decade, this technology has become a well established tool to study the ultrafast dynamics of low-energy elementary excitations [Hub01, Sch04, Ulb11, Kim12]. In these experiments, a femtosecond optical pump pulse prepares a non-equilibrium state of the system under study by either exciting a specific type of the correlated elementary excitations or by melting a correlation induced phase itself. A THz probe pulse that is offset by a given pump-probe delay time subsequently captures the momentary complex-valued dielectric response of the sample. By repeating this experiment as a function of the pump-probe delay time and recording the electric

¹The term *multi*-THz usually refers to photon frequencies above 10 THz.

field time-trace of the THz probe for each delay time, one obtains a femtosecond slow-motion picture of the ultrafast photoinduced dynamics of the full complex THz dielectric response [Hub01]. Femtosecond THz spectroscopy often allows one to separate spectrally overlapping resonances via their individual femtosecond dynamics and, most importantly, to resonantly monitor the femtosecond live interplay of low-energy excitations in strongly correlated materials after a controlled perturbation of the system.

In this work, optical pump/multi-THz-probe spectroscopy (introduced in *Chapter 2*) is technologically advanced [Por14b] and employed to elucidate the fundamental mechanisms in systems with strong coupling between their individual low-energy excitations. Crucial new insights are gained for two representative strongly correlated materials:

- It is clarified [Por14a] which microscopic mechanisms underly the formation of the charge density wave in the transition-metal dichalcogenide titanium diselenide ($1T\text{-TiSe}_2$). This study, presented in *Chapter 3*, is the main focus of this thesis.
- The investigation of phonon and quasiparticle dynamics in the high-temperature cuprate superconductor $\text{YBa}_2\text{Cu}_3\text{O}_{7-\delta}$, documented in *Chapter 4*, answers the question of whether there exists a temporal hierarchy between electron-electron and electron-phonon scattering processes in this system [Pas10].

A third experiment, discussed in *Chapter 5*, targets the ultrafast dynamics of low-energy elementary excitations in the regime of ultrastrong coupling:

- Non-adiabatic activation of ultrastrong light-matter interaction between a tailor-cut photonic resonance and an electronic excitation is implemented and studied on a sub-cycle timescale [Por12]. This part of the work further paves the way towards the observation of novel phenomena in non-adiabatic quantum-electrodynamics.

Separating structural and electronic order of the charge density wave in $1T\text{-TiSe}_2$

$1T\text{-TiSe}_2$ is a particularly interesting and intensely studied strongly correlated model material. Despite its relatively simple quasi-two-dimensional structure with a unit cell consisting of only three atoms, several many-body effects play important roles in defining its macroscopic properties. The most prominent phenomenon is the occurrence of a charge density wave. For more than 40 years, scientists have aimed to identify the microscopic origin of this phase transition. The solution of this enigma may not lead to immediate advances in our technology, yet it stands to reason that a comprehensive understanding of relatively simple model systems is an essential prerequisite on the route to understand and disentangle all the intertwined coupling mechanisms in more complex many-body systems, such as high-temperature superconductors.

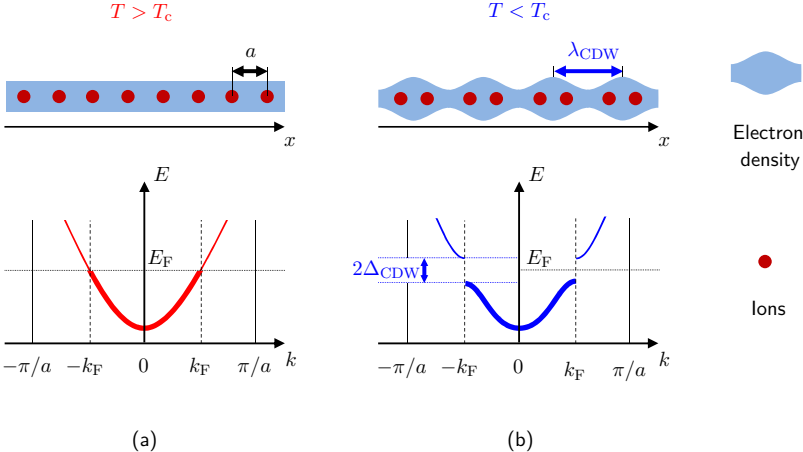


Figure 1.1: Schematic mechanism of a Peierls transition in a 1D metal. (a) Situation in the normal metallic phase: The free electrons (light blue) are homogeneously distributed throughout the crystal lattice (red dots) of period a . The half-filled conduction band (red line) is populated with electrons up to the Fermi energy E_F and the Fermi wavevector $k_F = \pi/2a$. In the charge ordered phase (b), the electron density is spatially modulated with a period of $\lambda_{CDW} = 2a$. The new Brillouin zone boundary at $k = k_F$, induced by the additional periodicity, yields the formation of a band gap $2\Delta_{CDW}$ and thereby energetically lowers the populated electronic states.

The basic concept of a Peierls-type charge density wave phase transition does not hold for the case of 1T-TiSe₂, yet it is well suited for introducing the fundamental features of the phenomenon: In 1930, Peierls proposed that a one-dimensional metal formed by an equally spaced chain with one electron per ion is unstable [Pei55]. For the normal metallic phase, the model system implies a half-filled conduction band with a Fermi vector of $k_F = \pi/2a$, where a is the lattice constant (see Figure 1.1(a)). In this case, the conduction electrons are free and delocalized throughout the crystal lattice. The instability comes from the fact that a periodic modulation of the crystal lattice with a wave vector of k_F (i.e. with a periodicity of $2a$) can lower the total energy of occupied electronic states by causing the formation of a band gap at the Fermi energy E_F (see Figure 1.1(b)). When the electronic energy gain outweighs the elastic energy associated with the periodic lattice distortion, the distorted phase represents the ground state of the system. The formation of a band gap at E_F makes the Peierls transition a metal-to-insulator transition. In real space, the renormalization of the electronic bands implies the localization of electrons (i.e. the formation of a charge density wave) with a periodicity of $2a$.

For 1T-TiSe₂, many different mechanisms have been proposed to explain the origin of the commensurate² charge density wave that emerges below a critical temperature of $T_c \approx 200$ K. Previous experimental results were mainly interpreted in favor of either a scenario that the charge density wave is a result of electron-phonon coupling analogous to a Peierls-type transition (e.g. [Hol01, Ros02b]) or that exciton-like coupling of free electrons and holes drives the phase transition (e.g. [Cer07, Mon10]). While low-energy excitations such as phonons, plasmons, charge density wave collective modes, and energy gaps provide unique THz fingerprints of lattice [Hol77, Sno03, MV11] and electronic orders [Li07b], their ultrafast dynamics have not been directly and simultaneously resolved so far. In this work, these degrees of freedom are monitored on the femtosecond scale after near-infrared (NIR) photoexcitation of the system. The novel experimental insights gained this way provide strong evidence that the concerted action of excitonic electron-hole correlations and a structural Jahn-Teller-like effect creates the charge density wave in 1T-TiSe₂. Furthermore, it is found that in the highly non-thermal transient state after photoexcitation, the structural component of the charge density wave can persist even when the excitonic effects are quenched. A quantum-mechanical theory based on the work from van Wezel *et al.* [Wez10b] corroborates the above conclusions.

Phonon and quasiparticle dynamics in superconducting $\text{YBa}_2\text{Cu}_3\text{O}_{7-\delta}$

Unconventional superconductors are materials in which the mechanism that stabilizes the Cooper-pairs is not exclusively based on BCS-like electron-phonon interactions. These synthetic materials have a rather complex crystal structure and bear a plethora of correlation induced phenomena. For the class of copper based “cuprate” high-temperature³ superconductors, these include commensurate and incommensurate spin and charge density waves, stripe-ordering, antiferromagnetic states and a peculiar pseudo-gap phase, that either stand in direct competition with the superconducting phase [Fau11, Cha12, Has14] or coexist with it [Hau10, Hay14, He14b]. Among the multitude of elementary low-energy excitations and their coupling mechanisms in these systems, the key ingredient for unconventional superconductivity has not yet been identified. Electron-phonon interactions, however, appear to be a pivotal factor. Although any type of purely phonon-based electron pairing mechanism fails to explain the defining property of high-temperature superconductors, evidence of significant electron-phonon contributions in cuprates has been found

²A charge or spin density wave is termed *commensurate* if its periodicity is a rational multiple of the lattice constant and is termed *incommensurate* if not.

³Systems that feature unconventional superconductivity with a critical temperature of $T_c \gtrsim 30$ K are usually referred to as *high-temperature* superconductors.

via various experimental techniques [Bat87b, Ope99, Rez06, Iwa08]. Pump-probe studies have been utilized with the goal of establishing a temporal hierarchy of microscopic interaction processes in order to qualitatively elucidate their potential relevance to the pairing mechanism. Near-infrared [Dem99, Kus08], mid-infrared [Kai00] and THz probe pulses [Ave01] as well as Raman scattering [Sai09] have allowed researchers to study the recombination of photogenerated quasiparticles and the recovery of the superconducting condensate following a strong optical perturbation. In a time- and angle-resolved photoemission spectroscopic (tr-ARPES) study of the system Bi-Sr-Ca-Cu-O the relaxation of the quasi-equilibrium electronic temperature was analyzed assuming a selective electron-phonon coupling [Per07]. However, since these experiments do not directly monitor the lattice degrees of freedom themselves, a more detailed picture of the role of the various phonon modes during an initial non-thermal regime has been beyond reach. Femtosecond electron diffraction has the potential to follow the evolution of the lattice directly [Ged07], but current sources are not yet sufficiently advanced to observe the key lattice modes that possibly assist the correlation of electrons in high-temperature superconductors [Sci11].

In this work, NIR-pump/multi-THz-probe spectroscopy is employed to address the question of whether there exists a temporal hierarchy between electron-electron and specific electron-phonon scattering processes in the prototypical high-temperature superconductor $\text{YBa}_2\text{Cu}_3\text{O}_{6.93}$ ($T_c = 92$ K). In order to study the ultrafast interplay between the electrons and lattice, femtosecond multi-THz probe pulses resonantly trace specific phonon modes and quasiparticles during a photoinduced transition to the normal state. The results demonstrate that in the system Y-Ba-Cu-O electron-phonon scattering occurs on a time scale comparable to that of the electron-electron scattering.

Femtosecond optical control and ultrafast dynamics of low-energy light-matter mixed states in the ultrastrong coupling regime

The detailed and proven understanding of fundamental electromagnetic interaction processes on the quantum level has led theoreticians to predict fascinating, fundamentally new quantum-electrodynamical phenomena (e.g. [Moo70, Ful76, Yab89, Lib07, Nat12, Wes14]). Many of these theories still await the development of novel technology that facilitates their experimental confirmation. One of the most prominent examples of the predicted phenomena is the dynamical Casimir effect: It describes the conversion of electromagnetic quantum fluctuations into real excitations when the vacuum ground state of a quantum system is modulated non-adiabatically (i.e. faster than a single oscillation of its fundamental electromagnetic eigenmodes). The first theoretical description of this process [Moo70] is based on the textbook scenario of the static Casimir effect. One considers two parallel,

perfectly reflecting uncharged metallic plates that are placed in vacuum. If the distance between the plates is sufficiently small, vacuum fluctuations yield a net “Casimir force” that measurably [Bre02] pushes the plates together. In this situation, the release of virtual electromagnetic excitations out of the quantum vacuum, as described by the dynamical Casimir effect, is predicted to occur when one of the mirrors undergoes a sufficiently accelerated motion at relativistic velocities [Moo70, Ful76]. Obviously, this intuitive model scenario cannot be realized in a laboratory. Fortunately, there are analogous systems that are technologically more feasible [Lib07, Wil11] to test this idea. Very promising in this respect are light-matter coupled intersubband cavity polariton systems in the regime of so-called ultrastrong coupling [Din03, Ciu05, Gün09]. Upon a sufficiently strong, non-adiabatic modulation of the light-matter coupling strength, virtual excitations of the THz electromagnetic eigenmodes are predicted to emit as Casimir photons into the external space [Ciu05, Lib07]. In a seminal work, Günter *et al.* [Gün09] demonstrated sub-cycle control of ultrastrong light-matter coupling in these systems. Yet, access to the relevant optical eigenmodes was rather limited and required highly complex experimental techniques. Since the virtual excitations are predicted to emerge as real excitations of the polaritonic eigenmodes [Lib07], full access to these modes constitutes an essential prerequisite for the detection of Casimir photons.

This work introduces a novel device that enables non-adiabatic optical activation of ultrastrong light-matter coupling between an eigenmode of a one-dimensional photonic crystal and an electronic intersubband resonance while providing straightforward access to all relevant eigenmodes. Femtosecond multi-THz spectroscopy is employed to demonstrate full access to the photonic band structure and to trace its non-adiabatic switching dynamics. Finite difference frequency domain (FDFD) simulations are in quantitative agreement with the experimental data and, additionally, allow for a microscopic understanding of the electromagnetic eigenmodes of the system.

Chapter 2

Ultrafast multi-terahertz spectroscopy

This chapter introduces the femtosecond multi-THz experimental techniques employed in this work. First, operational principles and modifications of the laser source, a home-built Ti:sapphire amplifier system, are discussed. Next, generation and detection of phase-stable THz pulses are explained along with a discussion on methods of two-time THz spectroscopy. Particular focus of this chapter is set on newly developed technology: A novel, high-gain collinear four-pass Ti:sapphire amplifier and a scheme to enhance the sensitivity of shot-noise limited field-resolved detection of THz radiation (published in *Optics Letters* [Por14b]).

2.1. The Ti:sapphire amplifier system

The accessible parameter space and noise characteristics of femtosecond multi-THz studies critically depend on the driving laser source. As will be seen in section 2.2.1, generation and field resolved detection of THz radiation require a pulse duration of the driving laser shorter than a half-cycle of the THz wave. Since detection of THz frequency components that approach the near infrared [Küb04] is an essential prerequisite for this work, the laser source must provide pulses with a duration of $\lesssim 15$ fs. Within the class of table-top lasers, this criterion can be met by setups based on mode-locked Ti:sapphire oscillators [Bal97, Ell01, Hub03, Sch03, Sud05] or fiber laser systems [Sel09, Kra10]. Another stringent requirement to the laser source is that it delivers a pulse energy high enough to optically manipulate correlation effects (e.g. to drive a phase transition). For most experimental scenarios, this excludes both fiber and Ti:sapphire oscillators with pulse energies typically far below $\sim 0.1 \mu\text{J}$. While current Ti:sapphire regenerative amplifier systems easily provide pulse energies up to several mJ, their noise characteristics renders them unsuitable for

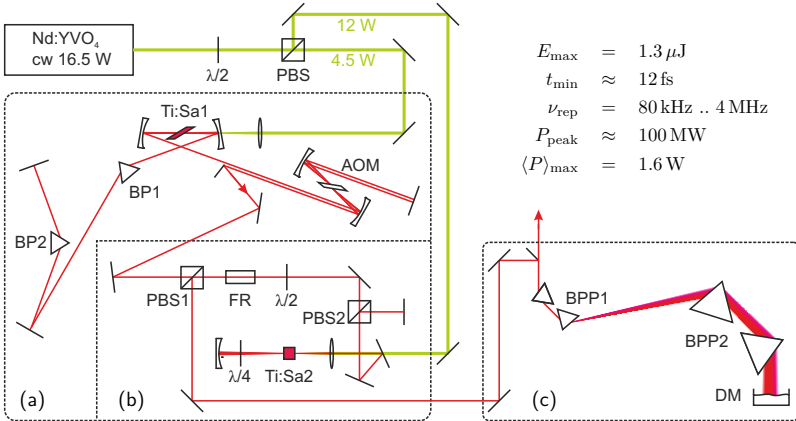


Figure 2.1: Layout and specifications of the Ti:sapphire amplifier system. (a) Cavity-dumped Ti:sapphire oscillator. BP1, BP2: Brewster-prisms. AOM: Acousto-optic modulator. (b) Novel collinear four-pass Ti:sapphire amplifier. PBS1, PBS2: Polarizing beam splitter cubes. FR: Faraday rotator. (c) Adaptive pulse recompression stage. BPP1, BPP2: Brewster-prism pairs. DM: Deformable mirror.

the studies performed here. Besides that, their comparably low repetition rate of a few kHz implies unfavorable measurement statistics.

To meet all experimental requirements for this work, a unique home-built Ti:sapphire amplifier system [Hub03] is employed. The system does not set a record with any individual feature, but closes the gap between Ti:sapphire oscillators and regenerative amplifier systems: It combines a high repetition rate of up to $f_{\text{rep}} = 4$ MHz with a pulse energy of up to $E_{\max} = 1.3 \mu$ J (see section 2.1.2) and a minimum pulse duration of $t_{\min} = 12$ fs. The central wavelength λ_c is tunable between 740 nm and 850 nm and a spectral bandwidth δ_λ of greater than 100 nm (full width at half maximum, “FWHM”) can be achieved. Excellent noise characteristics [Hub03] are maintained by employing a low noise Nd:YVO₄ continuous wave (CW) pump laser. Figure 2.1 shows the layout of the system: A cavity-dumped Ti:sapphire oscillator (a) generates seed pulses for a novel Ti:sapphire four-pass collinear amplifier (b). Dispersion of the amplified pulses is compensated in a pulse compression stage (c). Figure 2.2 depicts a typical spectrum and an interferometric autocorrelation of the pulses delivered by the system. The following sections elaborate on the components of the laser system in more detail.

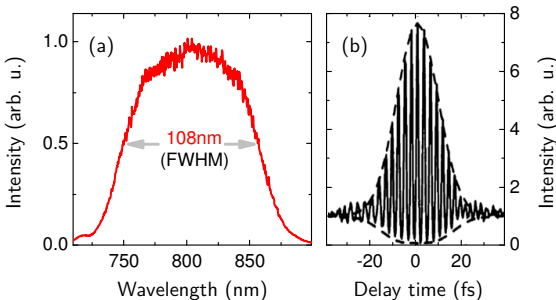


Figure 2.2: (a) Intensity spectrum and (b) interferometric autocorrelation of the pulses delivered from the Ti:sapphire amplifier system. (b) is reproduced from [Hub03]. A Gaussian fit to the autocorrelation (dashed line) reveals a pulse duration of 12 fs.

2.1.1. The cavity-dumped Ti:sapphire oscillator

A cavity-dumped, passively Kerr-lens mode-locked Ti:sapphire oscillator (figure 2.1(a)) based on the design by Pshenichnikov *et al.* [Psh94] forms the first element of the amplifier system.

Ti³⁺-doped sapphire (Al₂O₃) has become one of the most important gain media for femtosecond solid state lasers due to its outstanding optical [Mou86, Bra00] and mechanical properties. Since ultrashort laser pulses of duration Δt (standard deviation of the intensity envelope) comprise a large bandwidth of photon frequencies $\Delta\omega$ as demanded by energy-time uncertainty ($\Delta\omega\Delta t \geq 1/2$), the enormous fluorescence bandwidth of Ti:sapphire is key to the generation of femtosecond pulses: It allows for efficient amplification of longitudinal cavity modes with wavelengths ranging from 0.65 μm to 1 μm . The formation of femtosecond pulses requires a fixed phase-relation between the amplified modes. This is commonly achieved by exploiting the nonlinear Kerr effect [Mil10] in the Ti:sapphire gain medium itself: Intensity peaks resulting from constructive interference of the longitudinal modes are self-focused via a Kerr-lens (i.e. an intensity dependent refractive index profile with intensity dependent focal length) such that the spatial overlap of an intensity spike with the population inverted region in the gain medium is enhanced as compared to the situation in CW operation. Kerr-lens mode-locked Ti:sapphire lasers allow for the formation of near-infrared (NIR) laser pulses with a duration as short as 5 fs [Ell01].

Here, a highly doped (absorption coefficient $\alpha(532 \text{ nm}) = 6.27 \text{ cm}^{-1}$) Brewster angle cut Ti:sapphire crystal is pumped with a CW power of 4 W from a Nd:YVO₄ laser at a wavelength of 532 nm. The output power of the latest generation commercial pump source

is actively stabilized for frequencies up to 1 MHz (integrated rms-noise: 0.02%). This is tailor-cut for the operation with Ti:sapphire lasers, since pump noise at frequencies below ~ 1 MHz directly transfers to the output power of Ti:sapphire lasers [Mul08]. The lifetime of $\sim 4\ \mu\text{s}$ of the upper laser levels in Ti:sapphire [Mou86] accounts for this fact. An acousto-optic modulator (AOM) in the short arm of the laser cavity serves as pulse picker: An acoustic wave of nanosecond duration in a Brewster cut quartz crystal diffracts the intra-cavity laser pulse in double-pass geometry to the amplifier stage (figure 2.1(b)) with an efficiency of up to 70%. The radio frequency driver unit of the AOM is synchronized with the laser oscillator repetition rate $\nu_{\text{osc}} = 80\ \text{MHz}$. Laser pulses can be coupled out at an integer fraction of ν_{osc} . In addition, the AOM is used to initiate mode-locked operation. Astigmatism introduced by focal points of the cavity mode inside the Brewster cut optical elements is compensated with tilted folding mirrors [Kog72]. A fused-silica prism compressor (BP1, BP2) compensates intra-cavity group velocity dispersion. For further details on the oscillator and advantages of Ti:sapphire technology, see e.g. [Bra00, Hub03, Hub04, Küb07, Mil10].

2.1.2. A novel collinear four-pass Ti:sapphire amplifier

The energy of the pulses dumped from the oscillator via the AOM amounts to up to $\sim 35\ \text{nJ}$. To enable the class of experiments performed in this work (see chapters 3-5) a Ti:sapphire amplifier stage is employed to increase the pulse energy. Figure 2.1(b) shows the amplifier stage integrated into the laser system while Figure 2.3 depicts a detailed close-up view. In the first generation of the amplifier setup, a double pass geometry allowed for a maximum amplification factor of 16 for low average seed power [Hub03, Küb07]. A maximum pulse energy of $210\ \text{nJ}$ was reached in this scheme. Nevertheless, a yet higher pulse energy extends the experimental parameter space (e.g. by allowing for an increased photoexcitation intensity to melt more robust correlation induced phases) and improves the general flexibility of the system. For example, the output of the novel amplifier setup presented below would support the operation of up to six parallel beam lines in the formerly used configuration.

The main goal in the design of laser amplifiers is to achieve an efficient transfer of energy from the pump to the seed beam. Since the power of the seed light is usually limited, the common strategy underlying all amplifier designs is to maximize the spatial and temporal overlap of the seed photons with the population inversion in the gain medium. For efficient absorption of the pump light and a high spatial density of the population inversion, a highly doped gain medium is essential. At present, three different amplifier designs implemented with Ti:sapphire technology are common. When highest pulse energy

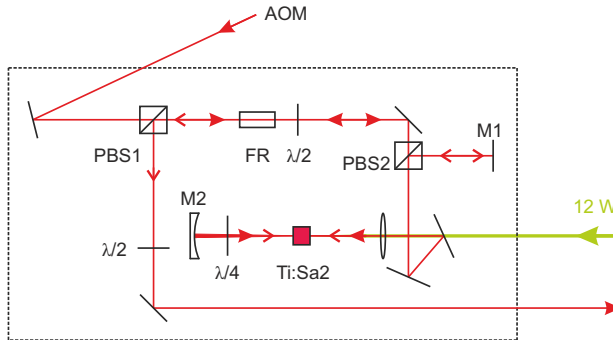


Figure 2.3: Close-up view of the collinear four-pass amplifier. AOM: Acousto-optic modulator of the Ti:sapphire oscillator (see Figure 2.1(a)). Ti:Sa2: Ti:sapphire gain medium. PBS1, PBS2: Polarizing beam splitter cubes. FR: Faraday rotator. M1, M2: Mirrors. Filled/open red arrows indicate the propagation direction of NIR pulses with horizontal/vertical polarization.

in the multi-mJ regime is of demand, it comes at the cost of a reduction in repetition rate to typically several kHz. Amplification in this regime is either accomplished with regenerative [Kme91] or non-collinear multi-pass [Bac95] chirped-pulse [Str85] amplifiers. In both cases, the effective spatial interaction volume for pump and seed beams is increased by sending the seed pulse multiple times through the population inverted region of the gain medium. In the case of regenerative amplifiers, an active element, such as a Pockels-cell, traps a seed pulse inside a laser cavity for several round-trips. In non-collinear multi-pass amplifiers the multi-pass beam path is set by geometrical means. Due to the lifetime of the upper laser levels of $4\,\mu\text{s}$ (for $T < 200\,\text{K}$ [Mou86]), pulsed pump lasers are necessary to maintain temporal overlap between population inversion and seed pulses at these repetition rates. When the repetition rate approaches the MHz regime, low-noise CW pumping of the gain medium becomes possible in combination with collinear amplification schemes [Hub03, Dan07, Oza10].

In this work, a novel collinear four-pass Ti:sapphire amplifier is developed. Apparently, this concept has never been applied routinely for the amplification of laser pulses, although a slightly different amplifier scheme is documented in the literature [And94]. Even though patented [McI93], no commercial Ti:sapphire laser system seems to make use of this approach.

For four-pass collinear amplification (see Figure 2.3), the horizontally polarized seed pulse is first transmitted through a Faraday isolator consisting of a polarizing beam splitter

(PBS1), a Faraday rotator (FR) and a half wave plate. In forward direction, the seed pulse experiences no change in polarization after passing these elements. After transmission through another polarizing beam splitter (PBS2), the first amplification pass through the CW-pumped Ti:sapphire amplifier crystal follows. Next, the combination of a quarter wave plate and a folding mirror (M2) rotates the seed polarization by 90° to vertical and focuses the beam back into the amplifier crystal for the second amplification pass. Thereafter, PBS2 and the end mirror M1 come into play by reflecting the vertically polarized seed pulse back into the amplifier crystal for the third pass. M2 and the quarter wave plate then rotate the polarization back to horizontal and send the seed pulse through the Ti:sapphire crystal for the fourth time. Now, the horizontally polarized amplified pulse again transmits through PBS2. In backwards propagation direction, the Faraday rotator and the quarter wave plate turn the polarization of the pulse to vertical and PBS1 finally separates the beam paths of incoming and outgoing pulses. In pass one and four, the seed pulse is polarized along the *c*-axis of the Ti:sapphire crystal, resulting in a higher gain in these passes due to a maximized gain cross section [Mou86].

The highly doped ($\alpha(532\text{ nm}) = 6.4\text{ cm}^{-1}$) Ti:sapphire amplifier crystal is pumped with a power of 12 W from the same pump laser as the oscillator and is mounted in an evacuated housing equipped with anti-reflection coated fused silica windows. The crystal is cooled to a temperature of 224 K via a cascade of Peltier elements to increase the lifetime of the upper laser levels and to reduce thermal lensing effects [Hub04]. An anti-reflection coated fused silica lens focuses the collinearly superimposed pump and seed beams to a focal beam waist of 20 μm (FWHM) inside the amplifier crystal. A custom made high power anti-reflection coating on both sides of the Ti:sapphire crystal allows for normal incidence of the beams without significant reflection losses. About 80% of the pump power of 12 W is absorbed in the 3 mm long crystal. This length is chosen to approximately match the two-fold Rayleigh length of the pump beam [Oza10]. Theoretically, even tighter focusing should increase the gain per pass [Oza10], but strong thermal lensing effects would be the consequence [Hub04] and impair the beam quality.

Figure 2.4 shows the amplification factor (blue dots) and average output power (red squares) of the laser system measured after the prism compressor stage as a function of the average seed power measured after the AOM. The low power amplification factor is close to 100. This represents a more than six-fold improvement compared to the performance of the previous double-pass design. With increasing seed power, the amplification factor decreases due to depletion of population inversion. The steep drop observed at comparably low seed power below 20 mW demonstrates an already very efficient depletion of the population inversion by stimulated emission. Consequently, the output power of the system scales strongly sub-linearly with the seed power. As an advantageous side effect,

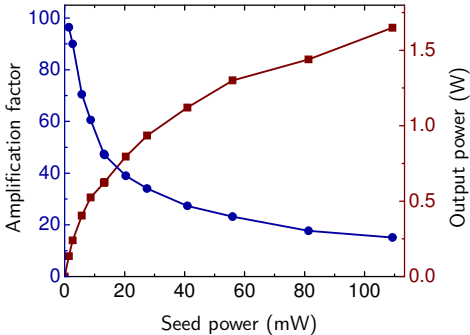


Figure 2.4: Net amplification factor (blue dots) and average output power (red squares) of the Ti:sapphire four-pass amplifier in combination with the pulse recompression stage as a function of the average incident NIR seed power at a repetition rate of $f_{\text{rep}} = 4\text{ MHz}$. The Ti:sapphire amplifier crystal is pumped with a CW power of 12 W.

the sub-linear scaling reduces the influence of seed power fluctuations on the output power. At the maximum cavity-dumping level at a repetition rate of 4 MHz, the average output power is as high as 1.6 W. A quantum efficiency of 23% for conversion of absorbed pump photons is reached in the amplifier in this case. With that, the presented four-pass amplifier operates at the same level of performance as state-of-the art regenerative amplifiers [Zha12]. A very interesting reference is given by the commercially available *Coherent RegA 9000* series: Its amplifier stage generates a maximum average output power of 1.6 W with a pump power of 12 W [Coh14], but only allows for amplification of pulses with a duration of $\approx 40\text{ fs}$ at much lower repetition rates.

An outstandingly simple alignment protocol is another advantage of the collinear four-pass amplifier design. Slight detuning of the quarter wave plate results in the formation of a laser cavity between M1 and M2 for a vertically polarized mode. This cavity can now be optimized by maximizing the laser power coupled out through PBS2. The diameter and the direction of the beam after PBS2 reveal the extra-cavity profile of the mode with maximum amplification and thus define the optimum beam parameters for the seed beam. In summary, for repetition rates typically used for experiments of 400 kHz, 800 kHz and 4 MHz, the maximum energy of the pulses delivered by the system is increased to $1.3\text{ }\mu\text{J}$, $1.0\text{ }\mu\text{J}$ and $0.4\text{ }\mu\text{J}$, respectively. This represents an up to six-fold increase compared to the double pass design [Hub03]. The other specifications of the system (see page 10) are defined by the Ti:sapphire oscillator and thus remain unchanged.

2.1.3. Dispersion management

For amplification, ultrashort pulses unavoidably pass through dispersive optical elements. Here, especially the two-fold transmission through the 2 cm long terbium-gallium-garnet [Sch94] Faraday rotator and multiple passes through the 5 mm thick polarizing beam splitters fabricated of SF2 glass induce optical chirp on the NIR pulses. This stretches the pulses to a calculated duration of 2.9 ps (total group velocity dispersion: $11.2 \times 10^3 \text{ fs}^2$, total third order dispersion: $5.8 \times 10^3 \text{ fs}^3$). Compared to the double pass setup [Hub03], the overall chirp in the new amplifier design is increased by only $\sim 20\%$.

For recompression of the pulses (figure 2.1(c)), the group velocity dispersion is compensated by two pairs of Brewster prisms (BPP1, BPP2) [Pro92]. A deformable mirror (DM) in the Fourier plane of the prism compressor allows for correction of remaining higher order chirp [Zee99]. A genetic optimization algorithm is employed to determine the surface profile of the deformable mirror which is controlled by 19 electro-static actuators. Feedback for the algorithm is given either by the intensity of optical second harmonic generation from the compressed pulses or the maximum electro-optically detected electric field amplitude of a generated THz electric field transient (see section 2.2.1).

2.2. Femtosecond multi-THz spectroscopy

The NIR femtosecond pulses delivered by the laser system described above are employed to operate the setup for femtosecond NIR-pump/multi-THz-probe spectroscopy. This technique is tailor-cut to study the live interplay of strongly correlated low-energy elementary excitations. In the experiment, a NIR pump pulse first induces a non-equilibrium state of the system under study. Then, a subsequent THz probe pulse captures the momentary dielectric response at a given delay time after photoexcitation. With field-resolved detection of the THz probe transients and variation of the pump-probe delay time, one obtains 2D-maps of the femtosecond evolution of the full complex THz dielectric response without the need for a Kramers-Kronig transformation. These datasets allow for investigation of the dynamic interplay of low-energy excitations via their transient THz spectral fingerprints.

In the following section, generation of phase-stable THz probe pulses from NIR femtosecond pulses via optical rectification as well as conventional electro-optic sampling (EOS) are summarized. The subsequent section elucidates the principles of two-time THz-spectroscopy. The experimental setup employed for this work is sketched and explained in Figure 2.5.

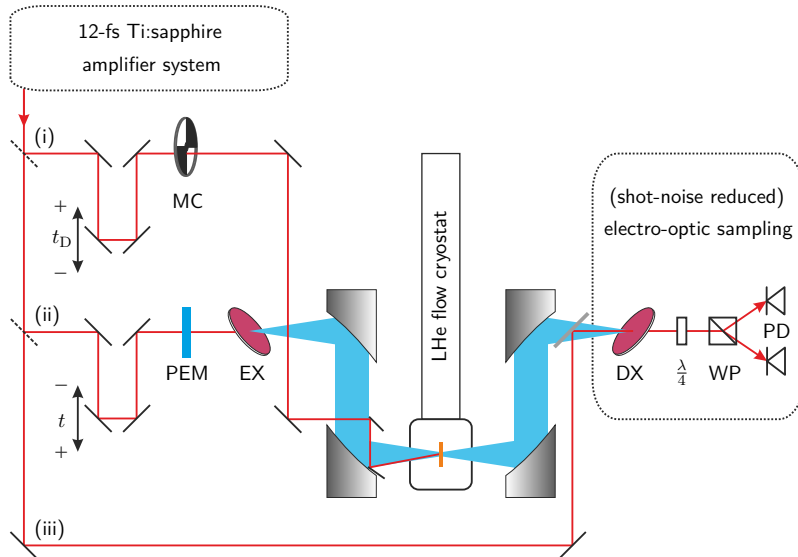


Figure 2.5: NIR-pump/multi-THz-probe setup. The 12-fs Ti:sapphire amplifier system (see section 2.1) serves as laser source. A first fraction of an incident NIR pulse photoexcites the sample (beam path (i)). A mechanical beam chopper (MC) switches the pump beam at a frequency of up to 1 kHz to facilitate lock-in detection techniques. A second portion of the NIR pulse (beam path (ii)) generates the THz probe (blue beam) via optical rectification (see section 2.2.1) in a nonlinear emitter crystal (EX). The polarization of the generation beam is periodically tuned with a photoelastic modulator (PEM) to modulate the emitted THz field amplitude at a frequency of $\nu = 84$ kHz for lock-in detection. A first set of parabolic mirrors focuses the THz probe beam onto the sample (orange box), which optionally can be cooled down to a temperature $T > 4$ K with a continuous flow helium cryostat. After interaction with the photoexcited sample (depicted for transmission geometry), the THz probe is focused on the nonlinear detector crystal (DX) via a second pair of parabolic mirrors. Here, the THz probe is spatiotemporally overlapped with the third fraction of the NIR pulse, the optical gate pulse (beam path (iii)) for (shot-noise reduced) EOS (see sections 2.2.1 and 2.3). Optical delay lines in branch (i) and (ii) set the pump-probe delay time t_D and the EOS delay time t , respectively.

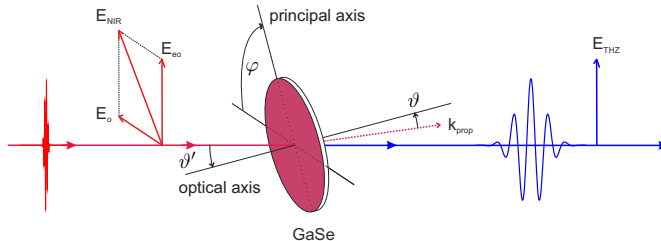


Figure 2.6: Geometry for the generation of phase-stable THz radiation (blue waveform) via phase-matched OR of a NIR pulse (red waveform) in a birefringent gallium selenide (GaSe) crystal. The NIR electric field (E_{NIR}) is comprised of extraordinary (E_{eo}) and ordinary (E_{o}) polarization components and the THz electric field (E_{THz}) is polarized extraordinary (i.e. “type II” phase-matching). ϑ' : External phase matching angle. ϑ : Internal phase matching angle. φ : Rotation of the crystal about its optical axis. k_{prop} : NIR wavevector inside the nonlinear crystal.

2.2.1. Generation and detection of phase-stable THz radiation

THz generation via optical rectification of femtosecond near-infrared pulses

In this work, tunable generation of ultrabroadband phase-stable THz pulses is realized by optical rectification (OR) of the 12-fs NIR laser pulses in a nonlinear THz emitter crystal (Figures 2.5 and 2.6). OR is a nonlinear optical $\chi^{(2)}$ -process that describes difference frequency generation (DFG) between frequency components contained in the spectrum of the driving laser pulse [Bon95]. Due to the large bandwidth of the 12-fs NIR laser pulses, difference frequencies as high as several ten THz can be generated this way. OR is most efficiently driven when the phase relation between the nonlinear difference frequency polarization and the intensity envelope of the NIR pulse is constant throughout the interaction length in the emitter crystal [Bon95]. This phase-matching condition can be naturally fulfilled in birefringent crystals when the polarization states of the generation and THz photons are suitably chosen with respect to the optical axis of the crystal [Hub00, Por14b]. A typical phase-matching configuration employed in this work is shown in Figure 2.6. Due to dispersion of the ordinary and extraordinary refractive indices, phase-matching cannot be fulfilled equally well for all THz frequencies. In a very inefficient case, the phase mismatch between the THz wave and the NIR pulse envelope accumulated at the exit surface of the crystal amounts to 2π and the THz wave generated in the first half of the crystal destructively interferes with the wave generated in the second half. Sufficiently thin crystals can minimize this effect and consequently permit the generation of THz pulses with a more broadband frequency spectrum.

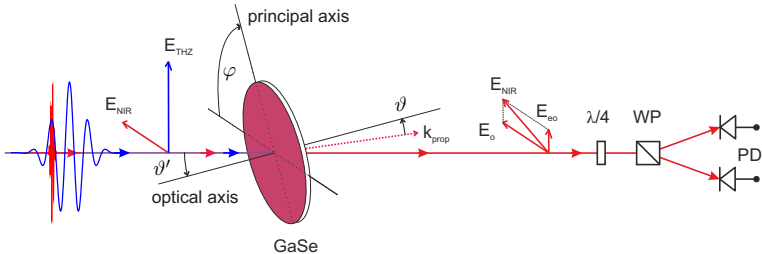


Figure 2.7: Geometry for type II phase-matched EOS of phase stable THz radiation (blue waveform) using a GaSe electro-optic sensor. For abbreviations see captions of Figures 2.6 and 2.5.

Since DFG in OR occurs between frequency components of a single NIR generation pulse, the non-stable NIR carrier-envelope offset phase [Mil10] cancels in the DFG process and the THz pulses generated via OR are inherently phase-stable, i.e. the transient electric field profile is identical in every THz pulse.

Electro-optic sampling of phase-stable THz radiation

One of the most important achievements of terahertz photonics is the possibility to detect free-space THz radiation with respect to the absolute phase and amplitude of its oscillating carrier wave [Fer02, Ton07]. In comparison to other technological implementations of field-sensitive detection, i.e. photoconductive antennas [Smi88] and plasma based methods [Dai06], electro-optic sampling [Wu95, Liu04, Küb04] stands out due to its excellent sensitivity. Besides its application in THz time-domain spectroscopy, EOS is widely used for sensing and imaging applications [Ton07, Moo12, Bla13]. Steady technological progress has pushed the frequency bandwidth accessible with EOS close to the near-infrared [Sel08b, Mat12]. It has been demonstrated, that for sufficiently strong THz fields, EOS readily allows for recording a full THz waveform with a single laser shot [Sha00].

For EOS, a phase-stable THz transient (blue waveform in Figure 2.7) is focused into a nonlinear optical detector crystal, where it co-propagates with an ultrashort NIR gate pulse (red waveform) [Gal99]. In a simplified picture, the THz electric field induces a quasi-instantaneous birefringence in the electro-optic sensor via the Pockels effect, leading to a phase retardation $\Delta\varphi$ between the linear polarization components of the gate pulse. This mechanism requires the gate pulse to be shorter than a half-cycle of the THz electric field. Phase matching can be employed to maximize the interaction length between the THz field and the gate pulse [Liu04, Küb04]. $\Delta\varphi$ is read out with an ellipsometer consisting

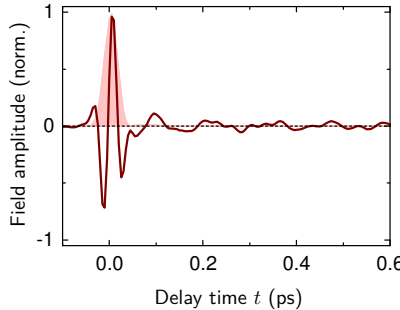


Figure 2.8: Single-cycle multi-THz field transient generated by phase-matched OR in a $15\text{ }\mu\text{m}$ thick GaSe crystal (type II phase-matching, $\vartheta' = 55^\circ$) and electro-optically sampled employing another GaSe crystal with the same thickness and orientation. The amplitude spectrum of the transient is shown in Figure 2.9. The shaded curve shows the intensity envelope with a duration (FWHM) of 35 fs.

of a quarter wave plate and a Wollaston prism (WP) (see Figure 2.7). The polarization optics split the gate power equally between two identical photodiodes (PD) as long as no THz field is applied, while a THz-induced phase retardation $\Delta\varphi$ causes an imbalance $S = I_a - I_b$ of the photocurrents (I_a, I_b) measured in the diode pair. Repeating this procedure as a function of the delay time t between the THz and the gate pulse results in a differential signal $S(t)$ that is directly proportional to the time trace of the THz electric field $E_{\text{THz}}(t)$.

Spectral coverage

In this work, NIR-pump/multi-THz-probe spectroscopy is accomplished in a frequency window ranging from 2 to 56 THz. For full coverage of this more than four optical octaves spanning frequency region, three different materials are employed as emitter and detector crystals. (i) Gallium phosphide (GaP) is suited for quasi-phase-matched OR and EOS for frequencies up to 7.5 THz. Transparency in the corresponding THz frequency window is the main advantage of the material and comes from the relatively high frequency phonon reststrahlen band beginning at ~ 9 THz [Bar68]. (ii) Gallium selenide (GaSe) is employed to cover frequencies from 8 to ~ 40 THz. Birefringent GaSe has become a standard material for multi-THz generation due to its wide phase-matching tuning range and its high nonlinearity [Liu04, Küb04]. (iii) Birefringent silver thiogallate (AgGaS_2 , AGS) is introduced with this work to cover frequencies above ~ 30 THz.

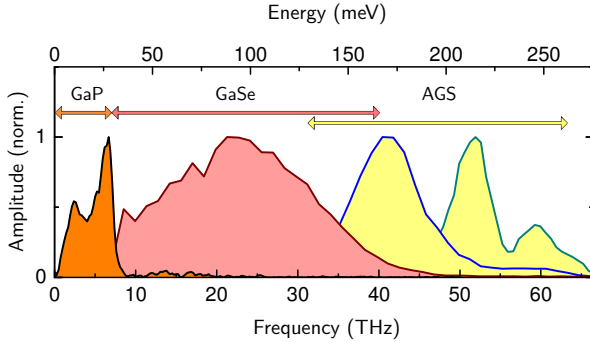


Figure 2.9: Linear amplitude spectra of THz transients recorded with EOS. The figure provides an overview of the spectral coverage of the experimental setup. Orange filled curve: $250\text{ }\mu\text{m}$ thick GaP crystals as emitter (EX) and detector (DX). Red filled curve: $15\text{ }\mu\text{m}$ thick GaSe as EX and DX, $\vartheta' = 55^\circ$ (spectrum of the single cycle transient shown in Figure 2.8). Yellow filled curves: AGS as EX and DX. Blue curve, yellow filling: $50\text{ }\mu\text{m}$ thick AGS crystals as EX and DX, $\vartheta = 53^\circ$, $\varphi = 45^\circ$. Green curve, yellow filling: $200\text{ }\mu\text{m}$ thick EX, $100\text{ }\mu\text{m}$ thick DX, $\vartheta = 60^\circ$, $\varphi = 45^\circ$. Horizontal arrows indicate the spectral range where OR and EOS is most efficient with the stated nonlinear crystal.

Figure 2.8 shows a typical multi-THz transient generated with phase-matched OR and recorded with phase-matched EOS. The duration of the waveform is practically bandwidth-limited and the electric field performs only one single optical cycle. The temporal intensity envelope (red shaded area) is as short as 35 fs (FWHM). GaSe is used as emitter and detector crystal. Phase-matching for OR and EOS is implemented in type II configuration (see Figures 2.6 and 2.7) with an external phase-matching angle of $\vartheta' = 55^\circ$. The ultrabroadband amplitude spectrum of the single-cycle THz transient is depicted in Figure 2.9 (red shaded curve). It contains frequency components from 8 to more than 40 THz . The type II phase-matching configuration together with the large external phase-matching angle close to the Brewster angle minimizes internal reflections in the z -cut GaSe crystals and thus suppresses undesired replicas of the main pulse [Küb07]. To fulfill phase-matching sufficiently for all THz frequency components contained in the spectrum, extremely thin GaSe crystals (thickness: $15\text{ }\mu\text{m}$) are employed. These single-cycle transients are used to probe the electronic degree of freedom in $1T\text{-TiSe}_2$. For further details on phase-matching geometries in GaSe for OR and EOS see e.g. [Hub04, Küb04, Liu04, Küb05, Küb07, Rei07]. The orange shaded curve in Figure 2.9 shows the amplitude spectrum of THz transients generated and recorded with $250\text{ }\mu\text{m}$ thick GaP as emitter and detector crystals. This

configuration covers the spectral range from 2 to 7.5 THz and is employed to study the lattice degree of freedom in 1T-TiSe₂.

THz transients with the amplitude spectra shown as yellow shaded curves in Figure 2.9 are generated and recorded using AGS as emitter and detector crystals. While the second order nonlinearity in AGS is estimated to be slightly lower than that of GaSe [Rot00, Küb04], its tuning range for phase-matching is even wider: The phase velocity of frequencies up to 90 THz can be matched with the group velocity of NIR femtosecond pulses. Despite this fact, application of AGS for OR and EOS has never been reported. Simulation of phase-matched OR [Bon95] in AGS based on a Sellmeier parametrization of its refractive indices [Fan84] reveals most broadband phase-matching in type I configuration (i.e. extraordinary and ordinary polarized NIR generation light, ordinary polarized THz radiation). This requires a crystal orientation of $\phi = 45^\circ$ [Rot00]. In contrast to GaSe, which can be cleaved only along the z -plane, single-crystals of AGS can be cut along any arbitrary plane and, hence, any internal phase-matching angle ϑ (angle between NIR/THz wavevector and optical axis) can be realized. In GaSe, ϑ is practically limited to 18° , resulting in a highest possible phase-matchable frequency of ~ 40 THz. By using AGS crystals with a thickness of 50 μm in the orientation described above and by setting $\vartheta = 53^\circ$, THz transients with an amplitude spectrum shown by the yellow shaded blue curve are obtained. More stringent phase-matching in thicker crystals (emitter: 200 μm , detector: 100 μm) tuned for even higher THz frequencies by increasing ϑ to 60° yields THz pulses with a center frequency as high as 52 THz. The yellow filled green curve shows the corresponding amplitude spectrum. In summary, by using AGS crystals for OR and EOS, the spectral range accessible for femtosecond spectroscopy with the present setup could be extended to cover photon frequencies of up to 56 THz.

2.2.2. Two-time THz spectroscopy for pump-probe studies

Probing the dielectric response of rapidly evolving non-equilibrium systems is a non-trivial task (for comprehensive reviews see e.g. [Kin99, Ném02, Ném05]). Conventional intensity based pump-probe experiments often suffer from limited time resolution and do not allow to directly access real and imaginary parts of the optical response functions simultaneously. In contrast, the unique possibility of two-time THz spectroscopy to resolve both the absolute phase and amplitude of a THz probe pulse that has interacted with a photoexcited sample at a given pump-probe delay time provides an ideal solution.

In an equilibrium system, the time-dependent polarization $P(t)$ induced by an electromagnetic waveform $E(t')$ is given by the convolution of the electric probe field with the

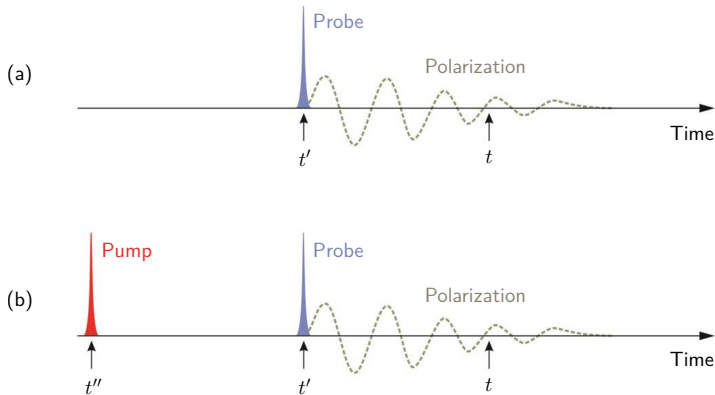


Figure 2.10: (a) In thermal equilibrium, a THz probe transient (depicted as a delta-like maximum, blue spike), incident at time t' , induces a polarization response, recorded electro-optically at time t with absolute amplitude and phase (green wave). (b) The non-equilibrium response following optical excitation with a pump pulse (red spike) at time t'' is probed by a THz field (blue spike) at time t' , and the subsequent polarization (green wave) is recorded electro-optically at time t .

time-domain dielectric response function $\varepsilon(t)$:

$$P(t) = \varepsilon_0 \int_{-\infty}^t E(t') [\varepsilon(t - t') - 1] dt' \quad (2.1)$$

Causality requires that the integral extends over all times t' prior to the time of observation t . Figure 2.10 (a) illustrates the situation for the case of a delta-like probe pulse. When the waveform of the incident probe field $E(t')$ is known, it is sufficient to measure the polarization $P(t)$. After Fourier transformation, the convolution decomposes into a product and the dielectric function $\varepsilon(\nu)$ is directly proportional to $P(\nu)/E(\nu)$. Both the probe $E(t')$ and the polarization trace $P(t)$ are captured with complete amplitude and phase information via EOS. This way, the full complex dielectric function is accessible without the need for a Kramers-Kronig transformation.

If photoexcitation induces a non-equilibrium state of the system, the response function itself may rapidly change while the induced polarization is recorded. This scenario is schematically depicted in Figure 2.10 (b): A pump pulse incident at time t'' drives the system out of equilibrium. Subsequently, an electric probe field (shown as a blue delta peak) at time t' induces a polarization response. Electro-optic sampling permits to capture this response with absolute amplitude and phase as a function of the EOS delay time $t - t'$.

It is important to note that the dielectric response of a non-equilibrium system cannot be described by a one-time-dependent dielectric function since the system evolves in time while its polarization is recorded. For a proper description, ε has to be represented by a function of two independent time intervals, namely $t - t''$ and $t - t'$, such that the polarization response of the photoexcited system reads [Kin99]

$$P(t, t'') = \varepsilon_0 \int_{-\infty}^t E(t') [\varepsilon(t - t', t - t'') - 1] dt' \quad (2.2)$$

It is not straightforward to retrieve the two-time response function from the above equation. In particular, it is not possible to deconvolve equation (2.2) by recording $P(t, t'')$ for a fixed pump time t'' and subsequently performing a Fourier transformation since both arguments of ε depend explicitly on t . It has been shown [Kin99], however, that this problem can be resolved when, instead of a single polarization transient $P(t, t'')$ with a set pump time t'' , one considers a set of data points taken from different pulses, measured with a fixed time delay $t_D = t - t''$ with respect to the pump pulse. Experimentally, acquisition of data in this way is achieved by keeping the relative arrival time between the pump and the electro-optic gate pulse fixed while the THz probe transient is continuously shifted in time. This is implemented in the setup (see Figure 2.5) by moving the delay line in branch (ii) and keeping the delay in branch (i) fixed. Ultimately, this approach allows one to retrieve

$$P(t, t - t_D) = \varepsilon_0 \int_{-\infty}^t E(t') [\varepsilon(t - t', t_D) - 1] dt' \quad (2.3)$$

Since t_D is kept constant, $P(t, t - t_D)$ can be deconvolved from $E(t')$ to yield $\varepsilon(t - t', t_D)$ or, after Fourier transformation, $\varepsilon(\nu, t_D)$. It is to note that the sampling delay time $t - t'$ and the pump-probe delay time t_D are not connected with each other by an uncertainty product. The maximum experimental time resolution is thus not limited by the duration of the probe pulse, but essentially set by the response time of the electro-optic detector [Kin99]. With a $15\text{ }\mu\text{m}$ thin GaSe sensor, the dynamics of $\varepsilon(\nu, t_D)$ can be retrieved with a time resolution of better than 40 fs.

2.2.3. Data acquisition and analysis

A THz probe transient acquired in the way described above directly encodes the polarization response of a photoexcited sample $P(t, t - t_D)$. In principle, by comparing this transient with a reference waveform recorded without the sample in place, the momentary dielectric response of the sample $\varepsilon(\nu, t_D)$ can be determined.

Another, experimentally more robust approach to measure $\varepsilon(\nu, t_D)$ is usually chosen when the dielectric response of the sample in thermal equilibrium $\varepsilon(\nu)$ is known. It is then sufficient to record the electric field that has interacted with the sample in thermal equilibrium E_{eq} and the pump-induced changes ΔE . With serial lock-in detection one can record both waveforms *simultaneously* [Küb07]. This approach is implemented as follows: A photoelastic modulator (PEM in Figure 2.5) modulates the THz pulse train with a frequency of 84 kHz. A first lock-in amplifier synchronously demodulates the current imbalance at the photodiodes and reads out the electro-optic signal. At the same time, the power of the NIR pump is modulated with a mechanical chopper (MC) at a much lower frequency of up to 1 kHz. Thus, for a sufficiently low integration time constant, the first lock-in amplifier measures alternately the electric field E_{eq} of a waveform that has interacted with the equilibrium sample and the electric field $E_{\text{xc}} = E_{\text{eq}} + \Delta E$ of a waveform that has interacted with the excited sample. While integration of the lock-in amplifier output yields the average reference field $E_{\text{avg}} = \frac{1}{2}(E_{\text{eq}} + E_{\text{xc}})$, demodulation of its output with a second lock-in amplifier at the frequency of the MC in the pump beam yields ΔE . From these quantities, E_{eq} and E_{xc} are directly calculated.

After recording the full waveforms, Fourier transformation along the time axis t for a fixed t_D yields $E_{\text{eq}}(\nu)$ and $E_{\text{xc}}(\nu, t_D)$. Since these quantities encode the polarization response of the entire probed volume, the exact geometry of the probe interaction of the THz pulse with the entire sample structure has to be taken into account for extraction of $\varepsilon(\nu, t_D)$. The optical transfer-matrix formalism is a convenient way to calculate the complex valued field transfer coefficient (i.e. the complex field reflection or transmission coefficient) of an arbitrary layered structure as a function of its refractive indices [Bor99]. It is employed here to express the field transfer coefficient of the excited sample

$$t_E(\nu, t_D) = \frac{E_{\text{xc}}(\nu, t_D)}{E_{\text{ref}}(\nu)} \quad (2.4)$$

as a function of $\varepsilon(\nu, t_D)$. In equation (2.4), $E_{\text{ref}}(\nu)$ corresponds to the reference electric field, that would be recorded without the sample in place. Since this quantity is usually not captured in the experiment, one may consider t_E factorized as

$$t_E(\nu, t_D) = t_{E,\text{pp}}(\nu, t_D) \cdot t_{E,\text{eq}}(\nu) = \frac{E_{\text{xc}}(\nu, t_D)}{E_{\text{eq}}(\nu)} \cdot \frac{E_{\text{eq}}(\nu)}{E_{\text{ref}}(\nu)}. \quad (2.5)$$

Here, the equilibrium complex field transmission coefficient $t_{E,\text{eq}}(\nu)$ can be expressed via the dielectric response of the sample in thermal equilibrium, eliminating E_{ref} . With the pump-induced change $t_{E,\text{pp}}(\nu, t_D)$ given by the experiment, the full field transfer coefficient of the photoexcited sample $t_E(\nu, t_D)$ is known and can be equated with the transfer-matrix expression. Numerical inversion of the transfer-matrix formalism then allows for extraction of $\varepsilon(\nu, t_D)$.

2.3. Shot-noise reduced electro-optic sampling

Currently, the ultimate limit of detector sensitivity in EOS is set by the quantum granularity, i.e. the shot-noise, of the gate laser pulses [Küb04, Mil10]. An overall increase of the sensitivity in EOS techniques may ultimately enable novel types of experiments in THz quantum optics including single-shot sampling of few-photon squeezed THz pulses or detection of THz photon bunches emitted from the quantum vacuum [Ciu05, Gün09, Por12]. Recent efforts to optimize the detector performance have aimed for improved detection electronics [Dar11], but have not diminished the shot-noise itself. This work presents a method that lowers the shot-noise in EOS and allows for reduction of the EOS acquisition time by more than one order of magnitude.

Balanced differential detection largely eliminates technical noise, such as excess power fluctuations of the gate pulses, since it typically affects the currents in both photodiodes equally. In state-of-the-art EOS, technical noise can be routinely suppressed to a level that the shot-noise of the gate pulses remains as the dominant noise source. Shot-noise arises from the quantization of the light field: The number of photons incident on each of the photodiodes follows a non-deterministic quantum distribution and can, hence, not be fully balanced. For a train of coherent gate pulses with an average power P_g , Poissonian statistics generates shot-noise Δ_S that scales with $\sqrt{P_g}$ [Mil10]. Since the electro-optic signal S itself is directly proportional to P_g [Gal99], the maximum signal-to-noise ratio (SNR) should, in principle, rise with $\sqrt{P_g}$. In practice, P_g is often limited by available laser power or undesired higher-order nonlinear processes in the DX (e.g. two-photon absorption). Furthermore, eliminating the excess noise sufficiently to reach the shot-noise level is more challenging for high P_g .

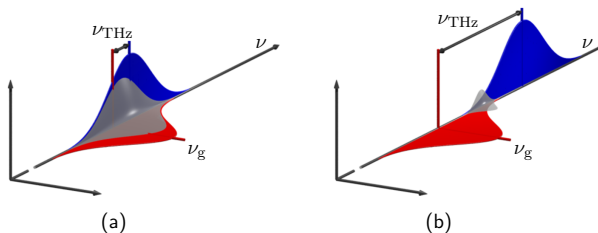


Figure 2.11: Schematic spectra and polarization directions of the incident gate pulse (red) (centered at ν_g) and of the sum frequency photons (blue) if the THz frequency ν_{THz} is small (a) and comparable (b) to the bandwidth of the gate spectrum. The electro-optic signal is located at the overlap of both spectra (gray shaded area).

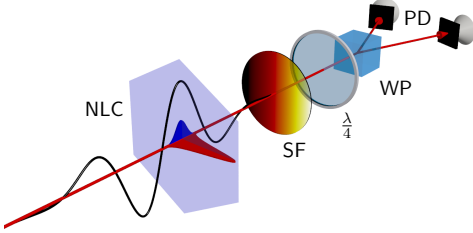


Figure 2.12: Setup for spectrally filtered EOS consisting of a nonlinear crystal (NLC) and an ellipsometer ($\lambda/4$ plate; Wollaston prism (WP); photodiodes (PD)). Black waveform: Schematic THz field transient. The nonlinear optical interaction of the linearly polarized incident gate (red pulse) with the THz wave generates new frequency components at perpendicular polarization (blue pulse). For spectrally post-filtered EOS, an optical spectral filter (SF) is inserted behind the NLC.

In the following it will be shown, that even for shot-noise limited detection the SNR can be further enhanced in commonly used EOS configurations. In order to explain the underlying idea, EOS is described in the more rigorous picture of frequency mixing between the gate and the THz photons [Gal99] (i.e. as the inverse quantum effect of optical rectification). Depending on the interaction geometry, the $\chi^{(2)}$ susceptibility of the DX can give rise to either sum or difference frequency generation between the gate and the THz pulse. These nonlinear interactions create a phase-coherent replica of the broadband gate spectrum which is up- or down-shifted by the THz frequency (see Figure 2.11). The newly generated photons contain polarization components perpendicular to the incident gate light. Interference of converted and fundamental photons alters the polarization state in the frequency region where both spectra overlap. When the resulting polarization is analyzed in a base rotated by $\pi/4$ with respect to the incident gate polarization, the phase difference between the orthogonal polarization components ($\Delta\varphi$) scales linearly and sign-sensitively with the THz electric field. Note that the electro-optic signal is solely generated by photons from the spectral overlap region. When the frequency of the THz photons ν_{THz} is small compared to the bandwidth δ_g of the gate spectrum, the interference occurs practically throughout the gate spectrum and the Pockels effect picture remains valid (see Figure 2.11(a)). If ν_{THz} is comparable to δ_g , the overlap region containing the electro-optic signal is located only at the wings of the gate spectrum and the electro-optic signal is reduced (see Figure 2.11(b)). In this situation, still all gate photons contribute equally to the shot-noise. Thus, a spectral filter (SF) inserted into the gate beam after the NLC (see Figure 2.12) can be used to select photons that contribute to the electro-optic signal and block those which only generate noise.

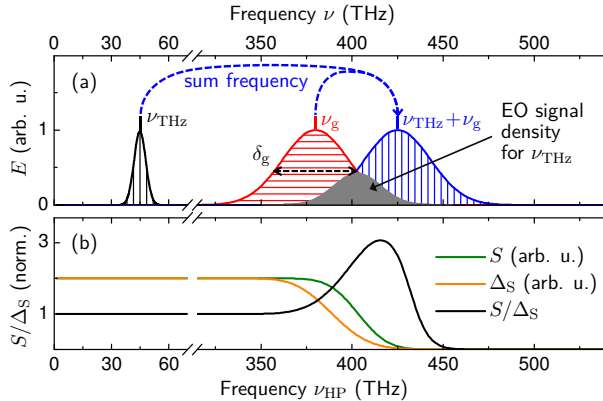


Figure 2.13: EOS in the case of sum frequency generation and $\nu_{\text{THz}} \approx \delta_g$. (a) Solid curves: Schematic amplitude spectra of the THz pulses (black), the incident NIR gate pulses (red) and the sum frequency replica of the gate spectrum (blue) for a given ν_{THz} . The hatching direction indicates the polarization direction in typical phase-matching geometries. Interference of the gate spectrum and its replica in the region of their spectral overlap (shaded area) yields elliptical polarization necessary for a field-sensitive electro-optic (EO) signal. (b) Spectrally integrated electro-optic signal for ν_{THz} (green curve) and shot-noise level (orange curve) as a function of the cut-on frequency of the high-pass spectral filter ν_{HP} , as calculated with the model described in the text. Black line: Normalized ratio between signal and shot-noise.

To quantify the influence of spectral filtering on the SNR, the following analysis assumes perfect phase-matching for sum frequency generation, a frequency independent nonlinear susceptibility $\chi^{(2)}$ and bandwidth limited pulse durations. Figure 2.13(a) schematically depicts typical spectra (solid lines) commonly seen in multi-THz spectroscopy based on Ti:sapphire lasers [Kuib04, Liu04]. The red line shows the field amplitude spectrum of the incident gate pulses $E(\nu)$ centered at a frequency of $\nu = \nu_g$. The sum frequency spectrum $A(\nu - \nu_{\text{THz}})$ and the THz spectrum $A_{\text{THz}}(\nu)$ are shown in blue and black, respectively. The sum frequency spectrum results from the gate spectrum and a given THz component ν_{THz} . Under the above assumptions, the spectral density of the electro-optic signal for a given frequency ν_{THz} (gray shaded area) is proportional to $\nu A(\nu) A(\nu - \nu_{\text{THz}})$ [Gal99]. Integrating over ν yields the electro-optic response as a function of ν_{THz} . In a conventional EOS setup, the photodiodes account for the spectral integration. If the gate pulses are spectrally filtered with a high-pass (HP) optical filter, the lower integration boundary is set by the cut-on frequency ν_{HP} . In summary, the spectral signal amplitude S then depends on the interacting pulses as follows:

$$S(\nu_{\text{THz}}) \propto A_{\text{THz}}(\nu_{\text{THz}}) \int_{\nu_{\text{HP}}}^{\infty} \nu A(\nu) A(\nu - \nu_{\text{THz}}) d\nu \quad (2.6)$$

The shot-noise amounts to:

$$\Delta_S \propto \sqrt{\int_{\nu_{\text{HP}}}^{\infty} \left((1-\eta) |A(\nu)|^2 + \eta |A(\nu - \nu_{\text{THz}})|^2 \right) d\nu} \quad (2.7)$$

Equation (2.7) explicitly takes into account that for large quantum efficiencies η of the sum frequency process, a large number of incident gate photons may be converted from frequencies below to above ν_{HP} and pass the filter. Figure 2.13(b) compares S (green curve) and Δ_S (orange curve) as a function of ν_{HP} for $\nu_{\text{THz}} = 45$ THz, the gate spectrum of Figure 2.13(a) and assuming $\eta = 1 \times 10^{-4}$. S remains unaffected for $\nu_{\text{HP}} \ll \nu_g$, but starts to decrease when ν_{HP} shifts through the overlap region between the fundamental and sum frequency spectra. In contrast, the noise drops faster with increasing ν_{HP} . A clear reduction already sets in when ν_{HP} reaches the low-frequency wing of the incident spectrum, i.e. below the overlap region with the sum frequency spectrum. This leads to an improvement of the SNR (black curve), which exhibits a well-defined maximum before it drops towards zero. If no other noise source becomes dominant for a lower overall photon fluence, this peak identifies the cut-on frequency for maximum SNR.

To test this idea experimentally, spectrally filtered EOS is implemented with a series of commercial standard optical high pass filters. To this end, THz pulses are generated by OR of the 12-fs NIR laser pulses in a $200\text{ }\mu\text{m}$ thick AGS crystal. A $100\text{ }\mu\text{m}$ thick AGS crystal is used for EOS. With phase-matching angles of $\phi = 45^\circ$ and $\vartheta = 57^\circ$ THz transients centered at 45 THz are obtained. To implement the sum frequency generation process in EOS, the polarization of the incident THz and gate pulse is set to ordinary and extraordinary, respectively. The energy, bandwidth and center frequency of the gate pulses are $E_g = 20\text{ nJ}$, $\delta_g = 42\text{ THz}$ and $\nu_g = 380\text{ THz}$. The calculated shot-noise relative to the overall current in the photodiodes amounts to $\Delta_S/(I_a + I_b) = 9 \times 10^{-9}\text{ Hz}^{-1/2}$. In order to visualize the corresponding experimental noise floor in the electro-optic signal, the THz power is attenuated to an estimated number of $\sim 10^6$ THz photons per pulse and a short lock-in integration time of $100\text{ }\mu\text{s}$ for a given delay time t is employed. This way, the same multi-THz waveform with three different choices of ν_{HP} is recorded (Figure 2.14(a)). As seen by comparison of the black waveform recorded with conventional EOS and the red waveform acquired with a HP filter in place ($\nu_{\text{HP}} = 375$ THz), spectral filtering strongly improves the SNR. Increasing ν_{HP} from 375 THz to 390 THz (blue waveform) yields further improvement. Quantitatively, the SNR increases by a factor of 2.9 for $\nu_{\text{HP}} = 390$ THz as

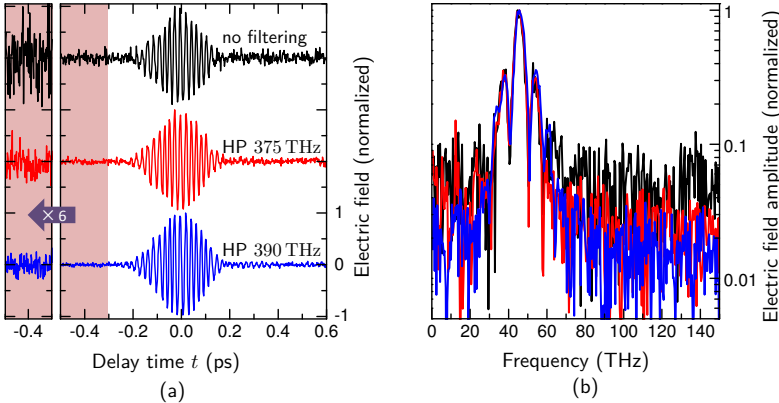


Figure 2.14: (a) Multi-THz field transients recorded with phase-matched EOS in AGS without spectral filtering (black curve) or employing high-pass filtering with a cut-on frequency of 375 THz (red curve) and 390 THz (blue curve). For better visibility of the noise floor, the THz pulse is attenuated before EOS. The panel on the left magnifies the amplitude in the red shaded time window by a factor of 6. (b) Amplitude spectra of the transients shown in (a) with the same color coding on a logarithmic scale.

compared to conventional unfiltered EOS. Figure 2.14(b) depicts the amplitude spectra of the three waveforms. The strongly suppressed noise background due to spectral filtering is equally well visible in frequency domain.

For the experimental parameters ($\nu_g = 380$ THz, $\nu_{\text{THz}} = 45$ THz, $\delta_g = 42$ THz, $\eta = 1 \times 10^{-4}$, $\nu_{\text{HP}} = 390$ THz), the theory predicts an improvement of the SNR by a factor of 1.9. The experimentally observed gain in SNR thus even exceeds the theoretical value. This fact can be attributed to the suppression of a remaining fraction of technical noise induced by fluctuations of the gate light. Without the spectral filter in place, the actual experimentally observed noise on the recorded transient is above the calculated shot-noise level by a factor of ~ 1.5 . Since the technical noise scales linearly with the power impinging on the photodiodes, reducing the overall photon fluence lowers the influence of technical noise as well. Accounting for both effects, the overall improvement by spectral filtering is perfectly explained.

Shot-noise reduction alone may even allow for larger improvement factors for other experimental parameters. For the assumptions made above, figure 2.15 summarizes the theoretical gain in the SNR as a function of the relative THz frequency $\nu_{\text{THz}}/\delta_g$ and the relative difference $(\nu_{\text{HP}} - \nu_g)/\delta_g$ and holds for $\delta_g \ll \nu_g$. The black curve in Figure 2.13(b)

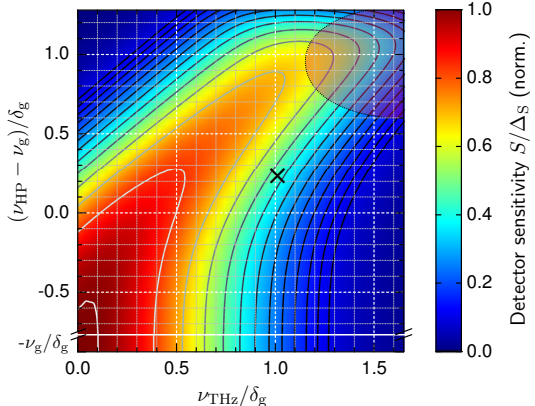


Figure 2.15: Calculated sensitivity S/Δ_S of spectrally post-filtered EOS for the sum frequency generation process. The abscissa represents the THz frequency ν_{THz} normalized to δ_g . The ordinate corresponds to the cut-on frequency of the HP filter ν_{HP} relative to ν_g in units of δ_g . The region below the vertical scale break corresponds to the sensitivity of conventional EOS. Contour lines are spaced by a factor of 1.2. The Figure holds for $\delta_g \ll \nu_g$ and $\eta = 1 \times 10^{-4}$. An increase of S/Δ_S by more than a factor of 5 can be obtained for configurations located in the purple shaded region. The coordinate corresponding to the experimental configuration with $\nu_{\text{HP}} = 390$ THz is marked with a black cross.

corresponds to a re-normalized vertical cut at $\nu_{\text{THz}}/\delta_g = 1$. For sampling of THz pulses centered at $\nu_{\text{THz}} = 1.3 \times \delta_g$, the SNR is expected to improve by a factor of 5.1 if the gate spectrum is high-pass filtered at $\nu_{\text{HP}} = \nu_g + \delta_g$.

In summary, this work introduces a universal method to enhance the sensitivity of EOS. It is shown, that this approach lowers the shot-noise significantly and is able to additionally suppress technical noise below a reduced shot-noise level. Existing EOS setups can be easily upgraded to enhance the SNR by up to 5 times saving as much as a factor 25 in measurement time, by adding a cost-effective spectral filter that can be selected with the presented analysis.

This novel concept has been employed consistently for the high-sensitivity studies of ultrafast photoinduced phase-transitions presented in the next chapter.

Chapter 3

Transient separation of excitonic and structural order of the charge density wave in 1T-TiSe₂

This chapter presents a femtosecond multi-THz study revealing the microscopic nature of the charge density wave (CDW) in 1T-TiSe₂. Ultrabroadband THz pulses are employed to simultaneously trace the ultrafast evolution of coexisting lattice and electronic orders. It is demonstrated that two components of the CDW order parameter – excitonic correlations and a periodic lattice distortion (PLD) – respond vastly differently to 12-fs NIR photoexcitation. Even when the excitonic order of the CDW is quenched, the PLD can persist in a coherently excited state. The underlying mechanism of the CDW formation is consistently identified as a cooperative coupling of excitonic correlations and a structural Jahn-Teller-like effect. A quantum-mechanical model [Wez10b] is employed to corroborate the interpretation of the experimental results. This part of the work has been published in *Nature Materials* [Por14a].

3.1. Transition-metal dichalcogenides and the role of 1T-TiSe₂

Transition-metal dichalcogenides (TMDs) are a family of layered compounds with chemical composition MX₂. M is a transition metal element (group 3 to 10 of the periodic table of the elements) and X is a chalcogen (group 16). Covalent bonds among the atoms result in layers of the form X–M–X with chalcogen atoms in two hexagonal planes separated by a plane of metal atoms. The layers themselves are weakly bound by Van der Waals interaction [Wil69]. The stacking of the layers is described by the polytype (e.g. 1T, 2H),

where the digit counts the number of layers per unit cell and the character abbreviates the symmetry of the unit cell (e.g. *T* for trigonal, *H* for hexagonal). Due to the weak interlayer coupling, TMDs can be considered as quasi two-dimensional structures.

The reduction of dimensionality has important consequences [Grü94]: Electronic correlations, random potentials and fluctuations have a more profound effect than in 3D systems. In TMDs, this leads to the formation of CDWs (e.g. in 1T-TiSe₂, 1T-TaS₂, 2H-TaSe₂ or 2H-NbSe₂) [Wil75], superconductivity (e.g. in 1T-TiSe₂, 1T-TaS₂ [Sip08] or 2H-NbSe₂ [Yok01]), room temperature excitons (e.g. in WSe₂ or MoS₂) [Coe87] or a Mott insulating state (in 1T-TaS₂) [Sip08]. A second asset of the weak out-of-plane interactions is the possibility to fabricate two-dimensional layers of single unit cell thickness via mechanical exfoliation techniques. Especially the rise of graphene [Gei07] attracted an increased interest in monolayered TMDs and their versatile electronic properties [Wan12]: One expects this class of two-dimensional systems to open up new possibilities in nano- and optoelectronics [Wan12] as well as in chemistry for batteries and supercapacitors [Chh13].

Among all TMDs, 1T-TiSe₂ has attracted special attention. Its distinctive, semi-metallic band structure [Zun78, Wez10a] facilitates remarkably strong electron-hole correlations [Cer07]. In addition, strong electron-phonon interactions are present [Web11]. Although the material has been studied since the 1960s, the simultaneous existence of both correlation effects has so far hindered the identification of the microscopic mechanism behind the formation of a commensurate charge ordered phase below $T_c \approx 200\text{ K}$. Recently, 1T-TiSe₂ regained interest due to the discovery of two superconducting phases and novel, chiral properties of the CDW [Ish10, Zen13]. A lattice incommensurate CDW phase constitutes the latest discovery in this material [Joe14]. Superconductivity in 1T-TiSe₂ is accompanied by suppression of the CDW and can be induced by pressure [Kus09] and impurity intercalation with Cu [Mor06] or Pd atoms [Mor10]. It remains elusive, whether both superconducting phases are part of the same superconducting region in the 3D pressure/Cu-intercalation/temperature phase space or if they underly completely different mechanisms. Impurity intercalation between the layers may increase the interlayer coupling, thereby reduce the 2D confinement for electrons and tip the balance in favor of 3D BCS-like superconductivity [Mor06]. This mechanism cannot account for pressure induced superconductivity, which is suggested to be of a rather unconventional, excitonic nature [Kus09]. However, it is assumed that superconductivity in both cases is closely related to the CDW phase [Mor06, Kus09]. A recent study suggests that phase fluctuations in CDW ordered domains may be connected to pressure induced superconductivity [Joe14]. In any case, to ultimately unravel the nature of the possibly unconventional superconductivity in 1T-TiSe₂, it is essential to understand the dominant correlation induced phenomenon first: The formation of a lattice commensurate CDW.

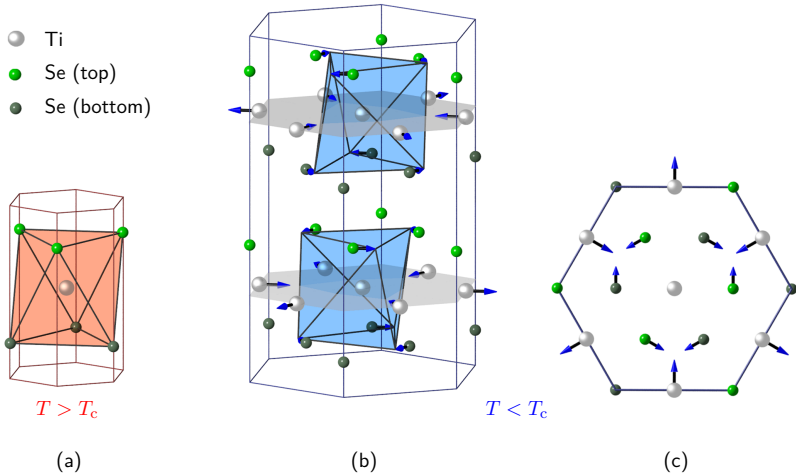


Figure 3.1: (a) Normal phase extended unit cell of 1T-TiSe₂. The red octahedron indicates the configuration of the Se ions around the central Ti ion. The red wire frame defines a normal phase primitive unit cell. In the CDW phase (b,c) the size of the unit cell is doubled in all three spatial dimensions. The periodic displacements of the Se and Ti ions are indicated by blue arrows (not true to scale). The blue body illustrates the distorted octahedral configuration of the Se ions around the Ti ion when the periodic lattice distortion is present at $T < T_c$. The blue wire frame shows a primitive unit cell in the CDW phase. In (c) one layer of the distorted structure is seen along the crystal c -axis (i.e. a top-view of one layer) to highlight the displacement pattern.

3.2. The CDW phase transition

3.2.1. Reconstruction of the crystal lattice and the electronic band structure

In its high-temperature phase, 1T-TiSe₂ belongs to the $P\bar{3}m1$ space group with three-fold symmetry about the c -axis. Figure 3.1(a) shows the normal phase unit cell of 1T-TiSe₂. The unit cell parameters are $a = b = 3.54$ Å (in-plane distance of Ti atoms) and $c = 6.001$ Å (out-of-plane distance of Ti atoms) [Rie76]. Upon cooling below $T_c \approx 200$ K, 1T-TiSe₂ undergoes a second-order phase transition into a commensurate CDW. The space group changes to $P\bar{3}c1$. Charge ordering is accompanied by the formation of a periodic lattice distortion corresponding to a structural $(2 \times 2 \times 2)$ superlattice [DS76, Hol77]. The phase transition doubles the size of the unit cell in all three spatial dimensions and, equivalently, halves the Brillouin zone (Figure 3.2). Figure 3.1(b) shows the unit cell in the CDW phase. The PLD is visualized by blue arrows showing the direction of displace-

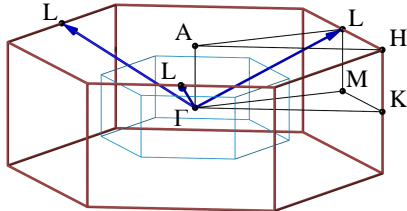


Figure 3.2:

Brillouin zone of 1T-TiSe₂ in the normal phase (red) and the CDW phase (light blue). The CDW wavevectors connecting the Γ and L points of the normal phase Brillouin zone are shown as blue arrows.

ment of the respective atoms (not true to scale). Figure 3.1(c) shows a top view of one Se-Ti-Se layer to highlight the displacement pattern. At a temperature of 77 K, the displacement amplitude of the Ti and Se atoms amounts to 0.04 Å and 0.014 Å, respectively [DS76]. The deformation pattern leads to a distortion of the Se octahedron (blue body in (b)) and implies three simultaneously present CDWs [Hol77]. In reciprocal space, the corresponding wavevectors q_{CDW} (blue arrows in Figure 3.2) connect the Γ and the three L points of the normal phase Brillouin zone. In the CDW phase, these high symmetry points are mapped on top of each other via the CDW wavevectors and form equivalent zone centers Γ' for the smaller CDW phase Brillouin zone (blue wire frame in Figure 3.2). 1T-TiSe₂ is a semimetal in both the normal and the CDW phase [DS76, Li07b]. Figure 3.3(a) illustrates the schematic band structure for $T > T_c$ in the vicinity of the high symmetry points related to the phase transition. At the Γ point a valence band of Se4p character reaches slightly above E_F , leading to the formation of a hole pocket. Electron pockets at the three L points originate from partially filled conduction bands of Ti3d character [Cer07, Roh11]. The periodic spatial reconstruction due to the CDW maps the bands at the Γ and the three L points on top of each other [Cer07, Roh11] and leads to the partial opening of an electronic energy gap, as illustrated in Figure 3.3(b) [Wez10b].

3.2.2. Possible driving mechanisms

On the search for the driving mechanism of the CDW phase transition various techniques have been employed. Superlattice peaks in neutron [DS76] or X-ray [Hol01, Web11, MV11] diffraction experiments allow one to identify the lattice distortion pattern and to study CDW induced changes in the phonon dispersion. Optical lattice resonances associated with the PLD can be observed with Raman scattering techniques [Sug80, Sno03] and, as explained in more detail below, via the THz optical response [Hol77]. The electronic degree of freedom was experimentally studied via DC transport measurements [Wil78b], the THz optical response [Wil78a, Lia79, Li07b] and time resolved [Roh11, Hel12] ARPES-experiments [Pil00, Kid02, Ros02b, Cer07]. Evidence for both excitonic and phononic

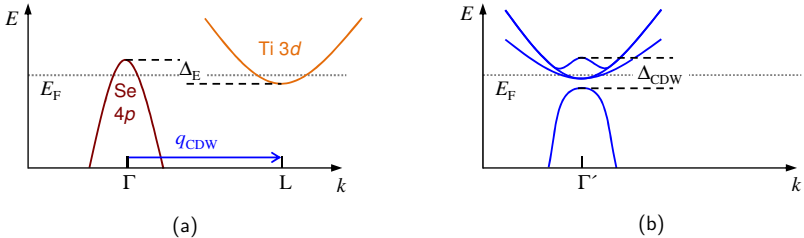


Figure 3.3: Schematic electronic band structure of 1T-TiSe₂ around the Fermi energy E_F at a temperature above (a) and below (b) T_c . Back-folding of the three symmetry equivalent Ti3d-like conduction bands (represented by an orange curve in (a)) from the L points by the CDW wavevectors q_{CDW} onto the zone centered Se4p-like valence bands (dark red curve in (a)) yields a gapped band structure (blue curves in (b)). Δ_E in (a) represents the small ‘negative’ band gap in the normal phase. Reconstruction of the band structure in the CDW phase as seen in (b) enables a direct transition from the valence to the conduction band across Δ_{CDW} . Illustration adopted from [Mon10].

contributions to the CDW phase transition was obtained in these experiments, leaving a controversial picture. Fermi surface nesting [Wha91, Joh08] was ruled out due to the lack of parallel Fermi surface contours between electron and hole pockets [Ros02b, Kid02]. In addition the latter mechanism usually leads to incommensurate CDWs. Ultimately, the following three scenarios remained under discussion:

(I) A band-type Jahn-Teller-like structural instability

The first model assumes electron-phonon coupling as the driving force and is based on a band-type Jahn-Teller effect [Hug77, Wha92]. This mechanism may be understood as the 3D analogue of the 1D Peierls instability: For an octahedral configuration of bound atoms, the Jahn-Teller effect describes the removal of degeneracy of electronic levels induced by a distortion of the octahedral structure. In 1T-TiSe₂, shortening of the Ti-Se bonds in the CDW phase [Wha92] is supposed to cause a Jahn-Teller-like energetic lowering of Se4p hole-like bonding bands [Ros02b] that stabilizes the distorted octahedral configuration. Experimentally, the important role of electron-lattice interaction in the phase transition is evidenced by the existence of a Kohn anomaly, i.e. a CDW related soft phonon mode [Hol01, Web11]. One can consider the PLD as superposition of three statically excited (“frozen”) L_1^- phonon modes with $k = q_{CDW}$ [Hol01]. The static amplitude of these modes and the electron-phonon coupling strength thus determine the amount of Jahn-Teller-like energetic lowering of the Se4p bands. Above T_c , static deformation of the lattice costs more energy than is gained from the concomitant lowering of the Se4p bands. Upon cooling

the system towards T_c , reduced thermal fluctuations allow for a more efficient electronic energy gain from population of the PLD constituent phonons. As a consequence, the overall energy needed to induce the PLD is reduced. Equivalently, the eigenfrequency of coupled oscillations of the PLD constituent phonons and the Se4p band energy (i.e. the soft phonon mode) shifts red. This coupled mode ultimately softens to zero frequency at $T = T_c$ [Hol01]. Below T_c , a static deformation of the lattice is energetically more favorable. The former L_1^- modes are now transformed into an A_{1g} CDW amplitude mode that describes the same deformation pattern but around the PLD equilibrium position. This mode stiffens when the temperature is further decreased [Bar08].

(II) The excitonic condensate scenario

This model assumes that the CDW transition is purely electronically driven [Pil00]. ARPES studies [Cer07, Mon10] revealed a remarkably strong back-folding of the electronic bands in the CDW phase. In addition, the opening of an electronic energy gap was observed. These findings could not be explained within the framework of a Jahn-Teller effect and were seen as evidence for spontaneous formation of bound electron-hole states (i.e. excitons) between the electron- and hole-like Fermi pockets. This excitonic instability is thought to drive a transition to a charge ordered state with a periodicity given by the spanning vectors connecting the valence band maximum at the Γ point with the conduction band minima at the three L points. The observations made in the ARPES experiments could be well reproduced by a theoretical model that accounts only for the presence of excitons [Mon09]. The PLD is considered as secondary effect induced via exciton-phonon coupling [Mon11]. However, the amplitude of the PLD and the soft phonon mode are not reproduced by this model. The term “condensate” does not refer to a macroscopic phase coherence of the excitons, but is used to account for the presence of free carriers [Mon10] that distinguishes the system from an excitonic insulator [Jér67].

(III) Combination of electron-phonon coupling and excitonic correlations

A third scenario proposes a combination of the above mechanisms. Van Wezel *et al.* [Wez10a, Wez10b] introduced a 1D model accounting for both a Jahn-Teller-like structural instability and exciton-like electron-hole correlations. This model directly captures the occurrence of the PLD and should in principle explain the observations made in the ARPES experiments [Wez10a]. In section 3.7, it is tested whether this model correctly reproduces the observations made in this work. A more detailed 3D model [Zen13] follows the same approach and additionally captures the chiral properties of the CDW. The latter is associated with different ordering amplitudes along the three CDW wavevectors.

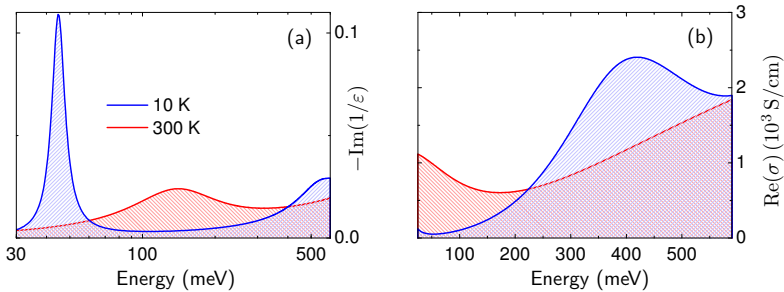


Figure 3.4: (a) Mid-infrared energy loss function $-\text{Im}(1/\varepsilon)$ in the normal ($T = 300 \text{ K}$, red curve) and the CDW phase ($T = 10 \text{ K}$, blue curve) according to the model function by Li *et al.* [Li07b]. The curve for $T = 10 \text{ K}$ results from a numerical adaption to the infrared reflectance of the sample under study (see Figure 3.7). (b) Corresponding curves of the real part of the optical conductivity $\text{Re}(\sigma)$ in the same mid-infrared window.

3.2.3. The infrared fingerprints of charge and lattice ordering

The transition to the CDW phase modifies the THz optical response in three distinct ways, enabling one to separately study the electronic and lattice degrees of freedom:

(i) Electronic order manifests itself most accessibly as a dramatic modification of the free carrier plasma response. The physical eigenfrequency of collective plasma oscillations (i.e. the screened plasma frequency) is marked by a zero crossing of the real part of the dielectric function ε . For a descriptive study of the plasma response, the energy loss function $-\text{Im}(1/\varepsilon)$ is much better suited [Hub01, Li07b], since a zero crossing of ε emerges as a characteristic pole in $-\text{Im}(1/\varepsilon)$. In the normal phase of $1T\text{-TiSe}_2$, collective plasma oscillations of free electrons and holes (compare Figure 3.3(a)) cause a broad plasmon pole in $-\text{Im}(1/\varepsilon)$ at a central energy of $\hbar\omega_{p,\text{norm}} = 145 \text{ meV}$ (Figure 3.4(a), red curve). The effective combined free carrier concentration n (see section 3.3.2) amounts to $n_{\text{norm}} = 7.1 \times 10^{20} \text{ cm}^{-3}$ [Li07b]. The spectral width of the plasmon pole is set by the free carrier scattering time $\tau_{\text{norm}} = 40 \text{ fs}$ [Li07b]. Below T_c , n strongly decreases due to renormalization of the electronic band structure (see Figure 3.3(b)), leaving behind a dilute electron gas with $n_{\text{CDW}} = 9 \times 10^{19} \text{ cm}^{-3}$. As a consequence, the screened plasmon pole shifts to an energy of $\hbar\omega_{p,\text{CDW}} = 45 \text{ meV}$ (Figure 3.4(a), blue curve). The reduced phase space for scattering in the ordered state increases τ to $\tau_{\text{CDW}} = 0.9 \text{ ps}$, causing a dramatic narrowing of the plasmon pole to a linewidth of 7 meV (FWHM).

(ii) The mapping of the L point onto the Γ point in the CDW phase enables a direct interband single-particle transition from filled Se4p to empty Ti3d derived bands across

the CDW gap. While a collective plasmon mode is studied most accessibly via $-\text{Im}(1/\varepsilon)$, a single-particle resonance appears most prominently as maximum in the absorption coefficient α and in the real part of the optical conductivity $\text{Re}(\sigma)$. As reported by Li *et al.* [Li07b] the transition across the CDW gap at $T = 10$ K prominently manifests itself in $\text{Re}(\sigma)$ as a broad maximum centered at an energy of 0.4 eV (Figure 3.4(b), blue curve). Importantly, the low-energy spectral wing extends to photon energies down to 0.1 eV. At $T = 300$ K, this single-particle resonance is absent (Figure 3.4(b), red curve). Note here that in $-\text{Im}(1/\varepsilon)$ the single-particle transition across the CDW gap emerges only as a relatively weak shoulder at an energy of 0.55 eV. Conversely, the sharp plasmon pole that dominates $-\text{Im}(1/\varepsilon)$ at a $T = 10$ K exhibits no tangible spectral feature in the corresponding spectrum of $\text{Re}(\sigma)$. Only at higher temperatures, the conductivity of free carriers yields an increase of $\text{Re}(\sigma)$ for photon energies up to $\hbar\omega_{\text{p, norm}}$.

(iii) The PLD affects the far-infrared response by inducing modifications of the phonon spectrum, as seen best via the imaginary part of the dielectric response function $\text{Im}(\varepsilon)$. Figure 3.5 depicts $\text{Im}(\varepsilon)$ in a far-infrared spectral window measured at various temperatures. Above T_c , a single transverse optical phonon resonance at 17 meV is observed (red curves). The mode of E_u symmetry involves an opposing in-plane motion of the Ti atom versus two Se atoms [Hol77]. Below T_c , PLD induced back-folding of the uppermost acoustic branch of B_u symmetry from the Brillouin zone boundary to the Γ point [Hol77] yields the additional IR-active in-plane mode at 19 meV (indicated by black arrows). The weaker peak at 22 meV (gray arrows) most likely originates from a folded optical branch [Hol77]. The absence of both PLD induced modes in the normal phase is highlighted by red crosses. The far-infrared dielectric response of 1T-TiSe₂ in thermal equilibrium shown in Figure 3.5 was measured via the complex valued THz field transmission through an 80 nm thin film of stoichiometric 1T-TiSe₂ (see section 3.3.1).

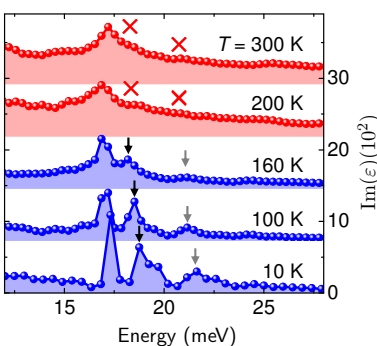


Figure 3.5:

Imaginary part of the far-infrared in-plane dielectric function of 1T-TiSe₂ measured with THz time-domain spectroscopy. At all temperatures, an IR-active E_u transverse optical phonon mode at an energy of ≈ 17 meV is visible. In the CDW phase, at temperatures $T < T_c$, (blue curves), additional resonances due to back folded phonon branches (indicated by black and gray arrows) attest to the presence of the PLD. For $T \gtrsim T_c$ (red curves), the PLD induced peaks are absent (red crosses).

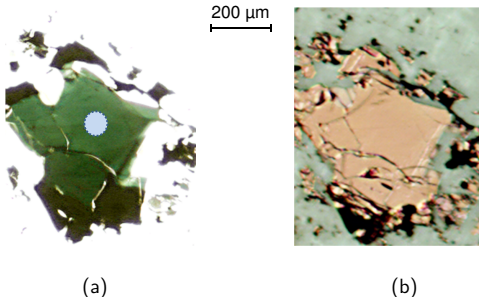


Figure 3.6: Optical microscopy image of a flake of $1T\text{-TiSe}_2$ on a diamond substrate taken with illumination from (a) below and (b) above the sample. The circle in (a) indicates the position of the probed spot and the size of the THz focus of $70\text{ }\mu\text{m}$ (FWHM) for photon energies around 45 meV . The thickness of the film at the probed spot is $\sim 80\text{ nm}$.

3.3. Paving the way for NIR-pump/THz-probe studies

3.3.1. Fabrication and properties of a thin film sample

The single-crystal of $1T\text{-TiSe}_2$ under study is grown by iodine vapor transport¹. Excellent stoichiometry of the sample (i.e. the absence of significant Ti-excess) is confirmed by its temperature dependent DC in-plane resistivity [DS76] (see also section 3.4.3) and the narrow plasmon pole observed at $T = 10\text{ K}$ (compare the corresponding curves in Figures 3.4(a) and 3.7 with the data presented in [Li07b] and [DS76]).

Spectroscopy of a non-transparent bulk crystal in thermal equilibrium is readily performed in reflection geometry. In contrast, THz probing of a photoexcited bulk sample of $1T\text{-TiSe}_2$ in reflection geometry would imply several issues: Since the penetration depth of the pump photons is much smaller than that of the THz photons, extraction of the dielectric function of the photoexcited sample from the pump-induced changes in the THz polarization response would have to account for an inhomogeneous excitation profile. Furthermore, due to the semi-metallic character of $1T\text{-TiSe}_2$, THz photons with energies above and below the plasma edge have dramatically different penetration depths and thus would effectively probe different excitation profiles. These complications can be avoided by probing a thin film in transmission geometry that is sufficiently transparent for all relevant photon energies.

¹Bulk samples have been provided by K. Rossnagel, Institute of Experimental and Applied Physics, University of Kiel, 24098 Kiel, Germany.

To this end, an 80 nm thin film of 1T-TiSe₂ with a lateral size of 0.2 mm × 0.2 mm is prepared. As a first step, a thin layer of the bulk sample is mechanically exfoliated onto commercially available adhesive tape². Repeated cleaving of the layer eventually results in thin, optically transparent films affixed to the tape. A selected film is then contacted to a CVD-grown diamond substrate by van der Waals bonding. Finally, the adhesive tape is dissolved with methanol. The single-crystal thin film sample of 1T-TiSe₂ on diamond substrate used for this work is depicted in Figure 3.6.

The film thickness of 80 nm is measured via optical transmission at a probe wavelength of 532 nm. The sample geometry and the refractive index at the probe wavelength [Bus93] are thereby taken into account via a transfer matrix formalism. Atomic force microscopy is employed to verify the optically measured thickness.

In the following, the NIR photoexcitation intensity is stated as absorbed pump fluence Φ . For the thickness of the studied sample, 1 μJ/cm² of incident pump fluence corresponds to an absorbed fluence of 0.44 μJ/cm² (calculated via a transfer matrix formalism) and an average energy deposition per room temperature unit cell (UC) of 2.4×10^{-5} eV/UC.

According to a finite difference frequency domain simulation (see chapter 5) that takes into account the refractive index at the pump wavelength [Bus93], the excitation density in the vicinity of the exit surface of the pump beam (i.e. the sample/diamond interface) is still 60% of the average excitation density throughout the sample. To ensure a homogeneous lateral excitation profile, the diameter of the pump focus is kept at twice the size of the THz spot.

3.3.2. Quantitative description of the plasma response

The screened plasma frequency ω_p and the free carrier scattering time τ provide a measure of electronic order, as discussed in section 3.2.3. To quantitatively link the above variables to the spectral shape of the plasma response, the following parameterization of the dielectric function introduced by Li *et al.* [Li07b] is employed:

$$\varepsilon(\omega) = \varepsilon_{\infty} - \frac{\omega'_p}{\omega^2 + \frac{i\omega}{\tau}} + \sum_{j=1}^2 \frac{S_j^2}{\omega_j^2 - \omega^2 - \frac{i\omega}{\tau_j}} \quad (3.1)$$

The three terms on the right hand side describe the background dielectric constant ε_{∞} , the Drude response of free carriers (second term, ω'_p : unscreened plasma frequency) and the two energetically lowest interband resonances parametrized by a sum of two Lorentzian oscillators (third term). The interband resonance with the lower frequency accounts for the single-particle transition across the CDW gap centered at $\omega_{\text{gap}} = \omega_1$ with a spectral width

²Best results with tesafilm®, ord. no. 57370-02, tesa SE.

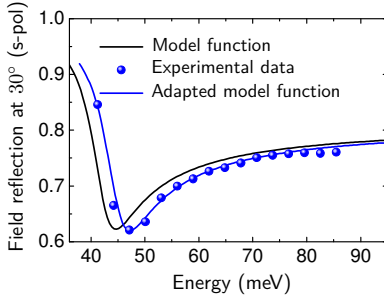


Figure 3.7: In-plane THz field reflection of 1T-TiSe₂ at $T = 10$ K for s-polarization and an angle of incidence of 30° . Black line: Calculated spectrum based on the model function and parameters by Li *et al.* [Li07b]. Blue dots: Experimental data of the sample under study. Blue line: Model function after numerical adaption of the plasma frequency and the free carrier scattering time.

of $\tau_{\text{gap}} = \tau_1$. The parameters ω_2 and τ_2 phenomenologically account for the contribution of the next higher interband transition associated with bands that are not directly related to the CDW phase transition.

The free carrier density n is inferred via

$$n = \frac{\omega_p^2 \varepsilon_0 \varepsilon_r m^*}{e^2} \quad (3.2)$$

employing the relation between screened and unscreened plasma frequency $\omega_p = \omega'_p / \sqrt{\varepsilon_r}$, using a relative permittivity of $\varepsilon_r = 60$ (extracted from [Li07b]) and assuming an effective free electron mass $m^* = m_e$ [Li07b].

For acquisition of the transient dielectric function $\varepsilon(\hbar\omega, t_D)$ as described in section 2.2.3, the model function is employed to describe the dielectric response of the unexcited sample for photon energies above the phonon reststrahlen band. Since most parameters of equation (3.1) are not explicitly stated by Li *et al.* in reference [Li07b], the model parameters are acquired by re-fitting the data presented in the reference. To account for the possibility of a slightly different equilibrium plasma response of the sample under study, its plasma edge in the reflectivity spectrum at a temperature of $T = 10$ K is measured (blue dots in Figure 3.7). To this end, the amplitude spectrum of a single-cycle transient reflected off a bulk sample is referenced against the amplitude spectrum of a transient reflected off a gold coated region of the sample surface. ω_p and τ are then numerically adapted so that the model function reproduces the measured reflectivity spectrum for photon energies from 40 meV to 85 meV (blue curve in Figure 3.7).

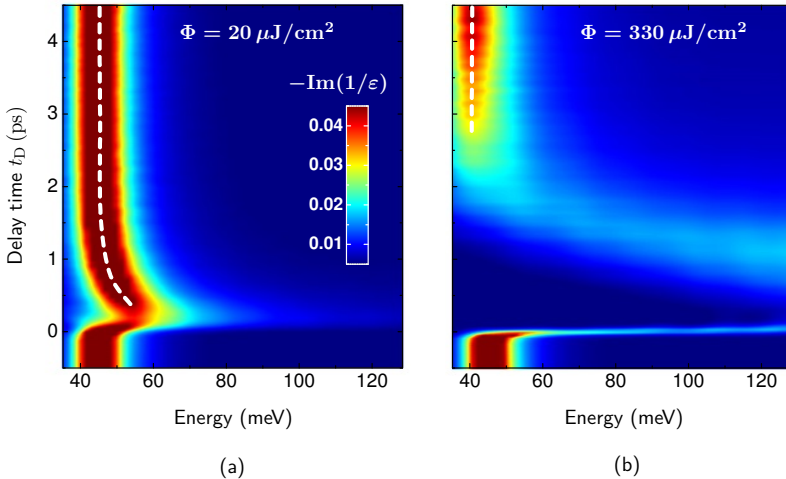


Figure 3.8: 2D-maps of the transient energy loss function $-\text{Im}(1/\varepsilon)$ as a function of photon energy and pump-probe delay time t_D following NIR photoexcitation at a temperature of $T = 10$ K. The figure depicts the situation for two representative excitation intensities: The dataset shown in (a) is acquired with an absorbed pump fluence of $\Phi = 20 \mu\text{J}/\text{cm}^2$ while (b) is measured with more intense photoexcitation with $\Phi = 0.33 \text{ mJ}/\text{cm}^2$. White dashed lines are guides to the eye tracing the center of the plasmon pole.

3.4. The electronic degree of freedom upon photoexcitation

As elaborated in section 3.2.3, charge and lattice ordering of the CDW in 1T-TiSe₂ manifest themselves as characteristic features in the THz dielectric response. This work harnesses these signatures for NIR-pump/THz-probe studies to separately monitor the femtosecond dynamics of electron and lattice order parameters after a controlled perturbation of the CDW ordered phase.

A first series of experiments targets the electronic degree of CDW ordering. It is analyzed on the femtosecond scale how the electronic order recovers from a perturbation induced by a NIR pump pulse and under which excitation conditions the electronic order is fully quenched. Ultrabroadband single-cycle transients (see Figure 2.8) are employed to probe the momentary dielectric response after photoexcitation. The temporal resolution of the experiments of 40 fs is set by the bandwidth of the electro-optic detector (see section 2.2.2). A reduced repetition rate of 400 kHz of the laser system ensures a complete thermalization of the sample with the diamond substrate between two laser shots.

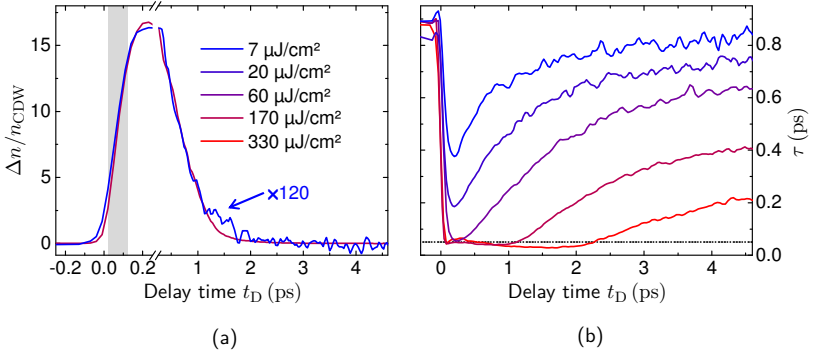


Figure 3.9: (a) Transient change in the free carrier density Δn relative to n_{CDW} and (b) transient free carrier scattering time τ . The curves are extracted from the complex transient energy loss function acquired for a series of pump fluences and a temperature of the sample of $T = 10$ K. The curve in (a) showing the change in n measured with $\Phi = 7 \mu\text{J}/\text{cm}^2$ is upscaled by a factor of 120 for quantitative comparison with the situation at $\Phi = 170 \mu\text{J}/\text{cm}^2$. The gray shaded time window in (a) highlights the rise time of Δn of 100 fs (from 20% to 80% of the maximum change).

3.4.1. Non-thermal recovery dynamics of the free carrier response

For photoexcitation of the charge ordered phase, the sample is kept at a temperature of $T = 10$ K. Figure 3.8(a) shows the measured spectra of $-\text{Im}(1/\varepsilon)$ as a function of t_D for an absorbed pump fluence of $\Phi = 20 \mu\text{J}/\text{cm}^2$ (the raw data of this experiment are shown in appendix A). At negative pump-probe delay times, the system is in thermal equilibrium characterized by the sharp plasmon pole at $\hbar\omega_{p,CDW} = 45$ meV. Upon photoexcitation, this peak rapidly blue-shifts and subsequently recovers within 1.5 ps. The pole remains narrow during the entire dynamics, indicating that the electronic order remains largely intact while photogenerated free electron-hole pairs elevate the plasma frequency. An increased fluence of $\Phi = 0.33 \text{ mJ}/\text{cm}^2$ induces a qualitatively different dynamics (Figure 3.8(b)). The plasmon pole shifts above the measurement window and stays strongly broadened during the subsequent relaxation. As discussed in more detail below, these signatures reflect the complete destruction of the electronic order. After a delay of $t_D \approx 2.5$ ps, a sharp plasmon pole re-emerges at its equilibrium position.

The model dielectric function denoted in equation (3.1) is also an excellent description of the non-equilibrium system. This enables a quantitative analysis of the photoinduced free carrier plasma response: For extraction of the transient plasma frequency $\omega_p(t_D)$ and the transient free carrier scattering time $\tau(t_D)$, the model function is adapted to the measured

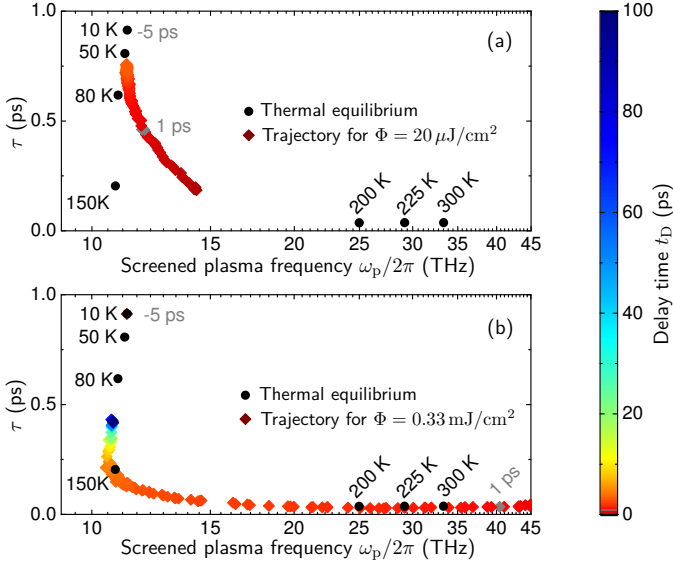


Figure 3.10: Plasma frequency ω_p and scattering time τ plotted as phase space coordinates of the free carrier system. Black spheres in (a) and (b) show combinations of ω_p and τ occurring in thermal equilibrium at the indicated temperatures. Transient states during the relaxation of the electronic system after photoexcitation are color coded with the pump-probe delay time t_D . Excitation with (a) $\Phi = 20 \mu\text{J}/\text{cm}^2$ yields non-thermal states, while the free carrier response traverses through thermally accessible states after excitation with (b) $\Phi = 0.33 \text{ mJ}/\text{cm}^2$.

transient dielectric response via both the real and imaginary parts of $1/\varepsilon(\hbar\omega, t_D)$ in an energy window from 40 meV to 100 meV (see appendix B for the quality of the fit curves). The transient free carrier density $n(t_D)$ is inferred from $\omega_p(t_D)$ via equation (3.2).

The transient change of the free carrier density $\Delta n(t_D) = n(t_D) - n_{\text{norm}}$ extracted from $1/\varepsilon(\hbar\omega, t_D)$ is shown in Figure 3.9(a) for a series of pump fluences measured at a sample temperature of $T = 10 \text{ K}$. After photoexcitation, Δn rises within 100 fs, as highlighted by the gray shaded time window. This delayed onset may be attributed to a cascaded relaxation of photoexcited charge carriers with high excess energy that leads to a measurably delayed generation of secondary free charge carriers. An exponential decay with a time constant of 0.5 ps follows. This dynamics of Δn is virtually identical for all fluences tested. In contrast, as seen in Figure 3.9(b), the temporal evolution of τ critically depends on Φ . Starting at $\tau_{\text{CDW}} = 0.9 \text{ ps}$, τ drops rapidly after photoexcitation and recovers on

a fluence-dependent ps timescale (a quantitative discussion follows in section 3.4.2). For $\Phi \leq 20 \mu\text{J}/\text{cm}^2$, τ remains distinctly above τ_{norm} for all delay times, indicating that the electronic order is not completely destroyed. In the case of $\Phi \geq 60 \mu\text{J}/\text{cm}^2$, the system temporarily reaches normal state conductivity with $\tau = 40 \text{ fs}$ and remains there for a duration of up to $\sim 2.5 \text{ ps}$, depending on Φ .

It is instructive to compare the photoinduced plasma response with the situation found in thermal equilibrium. In the latter, τ and the screened plasma frequency ω_p form a characteristic pair of values for a given temperature. Selected thermal combinations of ω_p and τ are shown as black spheres in the ω_p — τ diagrams of Figure 3.10 (value pairs for $T \geq T_c$ are taken from [Li07b]). This way of visualizing the parametrization of the plasma response allows one to readily identify non-thermal combinations of ω_p and τ that may be observed after photoexcitation of the system. Figure 3.10(a) depicts the value pairs of ω_p and τ observed after photoexcitation of the CDW phase with $\Phi = 20 \mu\text{J}/\text{cm}^2$ color coded with the pump probe delay time in the range of $0.2 \text{ ps} < t_D < 4.9 \text{ ps}$. The characteristic trajectory obtained this way clearly reveals that non-thermal combinations of ω_p and τ occur during the entire relaxation process. τ remains elevated indicating a persisting lack of scattering channels due to the partial survival of the electronic order. At the same time, optically generated free electron-hole pairs elevate the plasma frequency. In contrast, as seen in Figure 3.10(b), strong excitation with $\Phi = 0.33 \text{ mJ}/\text{cm}^2$ fully quenches the electronic order as indicated by a normal phase plasma response. The relaxation of the free carrier system occurs only through thermally accessible states including $T > T_c$. At the highest measured delay time of $t_D = 100 \text{ ps}$, the plasma response has settled to a state found at an equilibrium temperature³ of $T = 108 \text{ K}$ (deduced by interpolation of τ as a function of temperature). At this stage, the electronic system and the crystal lattice have fully thermalized and the whole system remains heated due to the optical deposition of energy. The sample thermalizes with the diamond substrate to $T = 10 \text{ K}$ before the next pump pulse arrives.

3.4.2. Signatures of excitonic order

The analysis presented above mainly focuses on two regimes of photoexcitation of the CDW phase: A slight optical excitation that leaves the electronic order partly intact and a comparably strong excitation that fully quenches the electronic order for several picoseconds. To study the role of the excitation density on the suppression of the electronic order in greater detail, n and τ are measured as a function of Φ (Figure 3.11). The delay

³This is in excellent agreement with the temperature of 99 K expected as a result of optical energy deposition [Cra78] by the NIR pump pulse, proving the consistency of the analysis.

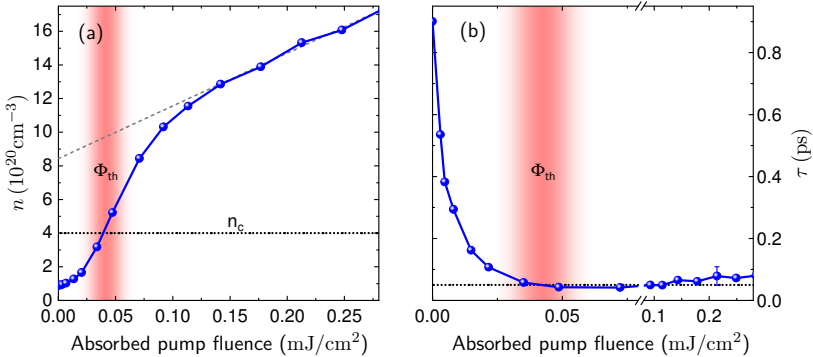


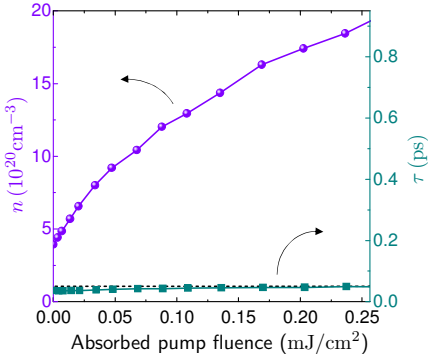
Figure 3.11: (a) Free carrier density n and (b) free carrier scattering time τ as a function of the pump fluence measured at a pump-probe delay time of $t_D = 0.2 \text{ ps}$ at a temperature of $T = 10 \text{ K}$. Vertical shaded lines indicate the threshold fluence $\Phi_{\text{th}} = 40 \mu\text{J/cm}^2$ required for transient suppression of the excitonic correlations. Horizontal dotted line in (a): Critical free carrier density $n_c = 4 \times 10^{20} \text{ cm}^{-3}$. Gray dashed line: Linear regression of $n(\Phi)$ in the high fluence regime ($\Phi > 0.14 \text{ mJ/cm}^2$). The horizontal dotted line in (b) marks the normal phase free carrier scattering time.

time is fixed at $t_D = 0.2 \text{ ps}$ such that the measured pump-induced changes have reached their maximum levels (compare Figure 3.9).

When exciting the system in the CDW phase ($T = 10 \text{ K}$), n first grows superlinearly with Φ , then changes its curvature at a threshold fluence $\Phi_{\text{th}} \approx 40 \mu\text{J/cm}^2$, and finally approaches a linear dependence for $\Phi > 140 \mu\text{J/cm}^2$ (Figure 3.11(a)). Simultaneously, τ decreases with Φ , reaches the normal phase limit, and then levels off for the highest pump fluences (Figure 3.11(b))). The fluence required to switch to normal state conductivity coincides with the inflection point Φ_{th} of the function $n(\Phi)$. Excitation below Φ_{th} leaves the electronic order partly intact, since τ remains above its normal state value. As studied already for a representative pump fluence in section 3.4.1, the electronic system in this excitation regime cannot be described by a thermal states.

Figure 3.12 shows the results of an analogous study starting from the normal state ($T = 205 \text{ K}$). The superlinear increase of n is not present in this case (purple dots) and τ remains at its normal phase value for all fluences (cyan squares).

The observed curve of $n(\Phi)$ for $T = 10 \text{ K}$ is consistent with the picture of charge-transfer excitonic correlations: The NIR pump generates primary electron-hole pairs with densities

**Figure 3.12:**

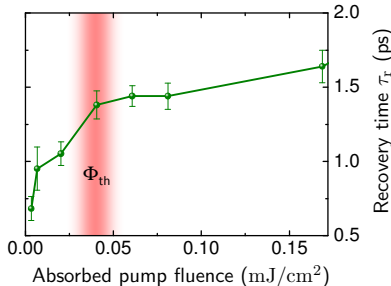
Dependence of the free carrier density n (purple dots) and scattering time τ (cyan squares) on the pump fluence for photoexcitation of the normal phase ($T = 205 \text{ K}$) measured at a pump-probe delay time of $t_D = 0.2 \text{ ps}$. The horizontal dotted line marks the normal phase free carrier scattering time.

scaling linearly with Φ . Their excess energy is relaxed via cascaded electron-electron scattering, which multiplies the quasiparticle density. For low excitation density ($\Phi < \Phi_{\text{th}}$), the photogenerated carriers screen electron-hole Coulomb interactions and thus reduce the excitonic binding potential. As a consequence, part of the bound pairs break into free carriers leading to an additional fluence dependent increase of n . This explains the superlinear rise of n . As soon as the photoinduced carrier density exceeds a critical value n_c for $\Phi > \Phi_{\text{th}}$, excitonically bound electron-hole pairs can no longer exist, τ assumes its normal state value (Figure 3.11(b)) and the superlinear scaling of n stalls (Figure 3.11(a)). Upon full suppression of all remaining excitonic Coulomb correlations (i.e. electron-hole fluctuations that are also present in the high-temperature phase [Cer07, Mon10]), only the linear dependence of n on Φ remains (dashed curve in Figure 3.11(a)). Consequently, the superlinear increase of n is absent if the system is excited in the normal phase, since no additional carriers are released from excitonically bound electron-hole pairs.

The idea that Coulomb screening affects the strength of excitonic correlations is widely discussed in literature [Li07b, Mon10]. Here, the effects of photoinduced Coulomb screening are quantitatively analyzed via the Thomas-Fermi screening length r_{TF} . This measure describes the effective range of a Coulomb potential in the presence of free carriers:

$$r_{\text{TF}}(n) = \sqrt{\frac{\pi^2 \hbar^2 \varepsilon_0 \varepsilon_r}{m^* e^2} (3\pi^2 n)^{-\frac{1}{3}}} \quad (3.3)$$

Using the same values for ε_r and m^* as in equation (3.2) and $n = n_{\text{CDW}}$, a screening length of $r_{\text{TF}} = 1.34 \text{ nm}$ is obtained for the system in the CDW phase. This value allows for efficient Coulomb attraction between electrons and holes on a length scale larger than the in-plane and out-of plane CDW wavelength of 1.23 nm and 1.2 nm , respectively. At the critical density of $n_c \approx 4 \times 10^{20} \text{ cm}^{-3}$, the screening length is reduced to 1.05 nm . Thus, electron-hole attraction on a length scale related to the CDW period should be strongly

**Figure 3.13:**

Recovery time constant τ_r of the excitonic order as a function of the pump fluence. The red shaded vertical line indicates the threshold fluence Φ_{th} . Error bars indicate the 95% confidence interval.

suppressed. This is in line with the experimental observation of quenched excitonic order for $n > n_c$.

An analysis of the y -intercept of the linear fit of $n(\Phi)$ for $\Phi_{th} > 140 \mu\text{J}/\text{cm}^2$ underpins the above picture. Extrapolation of the linear dependence to zero fluence yields $n_{\text{extrap}} = 8.5 \times 10^{20} \text{ cm}^{-3}$. This value describes the hypothetical free carrier density after a quench of all electron-hole correlations without the presence of primary photogenerated carriers. If the above picture is valid, this state of the free carrier system should be comparable to a situation in thermal equilibrium when no electron-hole correlations are present, as it is the case for $T \gtrsim 300 \text{ K}$. Indeed, the values of n_{norm} observed at $T = 300 \text{ K}$ and n_{extrap} are in good agreement.

As mentioned in section 3.4.1, the recovery of τ after photoexcitation of the CDW phase occurs on a fluence dependent timescale. Remarkably, the threshold behavior described above manifests itself also in the recovery dynamics of τ . Figure 3.13 shows the recovery time constant of τ as a function of Φ acquired by numerical adaption of an exponential decay to the curves shown in Figure 3.9(b). For each value of Φ , only those sections of $\tau(t_D)$ are considered, in which τ is rising towards its low-temperature value. The time constant τ_r thus describes the recovery of the excitonic order once this process has set on. Importantly, τ_r reflects the same threshold behavior as already discussed above. A fast recovery is found when the system is excited below Φ_{th} . In this case, part of the excitonic order remains present and long range order does not have to be newly established from spontaneous fluctuations. Above Φ_{th} , the recovery time features a plateau at $\tau_r = 1.5 \text{ ps}$. This value reflects the recovery time constant of the excitonic order after a full quench.

In conclusion, the observed photoinduced modifications of the low-temperature plasma response discussed in this section can be consistently explained by the existence of excitonic charge ordering in 1T-TiSe₂. The next section tests whether this interpretation is compatible with the well known DC resistivity anomaly of 1T-TiSe₂.

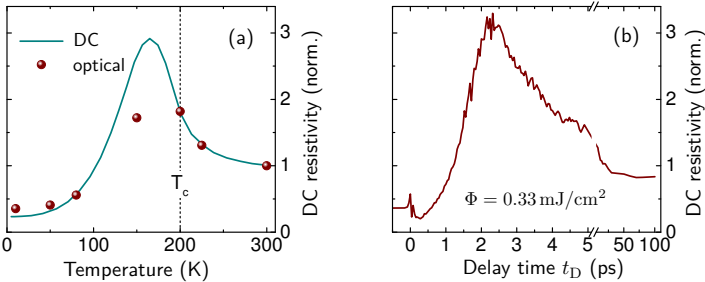


Figure 3.14: (a) Cyan curve: Equilibrium in-plane DC resistivity⁴ of the sample under study as a function of temperature normalized to the value at $T = 300$ K. Red dots: DC resistivity calculated from the equilibrium values of ω_p and τ via equation (3.1). The dashed vertical line indicates the inflection point of the DC resistivity at T_c . (b) Ultrafast evolution of the DC resistivity calculated from $\omega_p(t_D)$ and $\tau(t_D)$ measured with $\Phi = 0.33 \text{ mJ/cm}^2$ at $T = 10$ K.

3.4.3. The DC resistivity anomaly

The DC resistivity of $1T\text{-TiSe}_2$ exhibits an anomalous temperature dependence: Unlike other semimetals or metals, the resistivity does not monotonically decrease upon cooling from room temperature, but instead traverses a pronounced maximum below T_c [Wil78b, Lia79, Mor06, Kus09] (Figure 3.14(a)). The CDW phase transition occurs at the inflection point on the high temperature side [Wil78b]. Cooling from high temperature to T_c first increases the resistivity due to a reduction of the effective free carrier concentration. Upon further cooling, the loss of scattering channels [Li07b] due to stabilization of CDW long range order increases the free carrier scattering time and thereby reduces the resistivity. The anomaly vanishes together with the CDW order e.g. upon substitution of Se with S [Wil78b], Cu-intercalation [Mor06] or application of pressure [Kus09]. Here, the transient DC resistivity is extracted from the time resolved THz spectroscopic data by extrapolating the adapted free carrier plasma response to zero frequency [Lia79]. For the equilibrium spectra, this approach is able to qualitatively reproduce the DC resistivity anomaly (see Figure 3.14(a)). Since the optical conductivity after excitation with $\Phi = 0.33 \text{ mJ/cm}^2$ mimics thermal states, including $T > 300$ K, during its relaxation (see Figure 3.10), it immediately follows that the transient DC conductivity traverses the anomalous maximum, as indeed seen in Figure 3.14. At early delay times, the resistivity is reduced due to additional photogenerated electron-hole pairs. At $t_D \approx 1.1$ ps, the transient resistivity corresponds to an equilibrium resistivity measured at a temperature

⁴Data have been provided by C. Sohrt, Department of Physics, University of Kiel, 24118 Kiel, Germany.

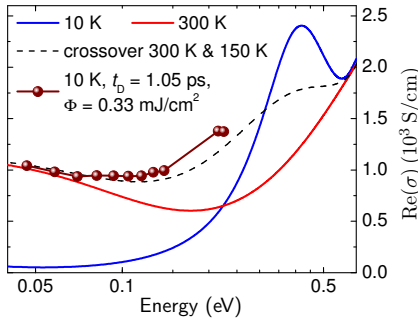


Figure 3.15: Solid lines: $\text{Re}(\sigma)$ in thermal equilibrium reproduced from Figure 3.4(b). Red dots: $\text{Re}(\sigma)$ measured after photoexcitation with $\Phi = 0.33 \text{ mJ/cm}^2$ at a delay time of $t_D = 1.05 \text{ ps}$ and a temperature of $T = 10 \text{ K}$. The two data points around a photon energy of 0.22 eV were acquired in a separate experiment using AGS as THz emitter and detector. Dashed line: Hypothetical conductivity of a crossover phase exhibiting a free carrier response as observed at $T = 300 \text{ K}$ in combination with a CDW gap transition as seen at $T = 150 \text{ K}$.

of $T = 300 \text{ K}$. The anomalous maximum is traversed at $t_D = 2.5 \text{ ps}$. When one considers the DC resistivity anomaly as a fingerprint of excitonic charge order, this time trace can be understood in line with the interpretation of the recovery dynamics of the multi-THz plasma response (see section 3.4.1). Intense photoexcitation with $\Phi = 0.33 \text{ mJ/cm}^2$ quenches the excitonic order and thereby induces a DC resistivity characteristic for the normal phase. Recovery of the electronic order occurs through states that can be characterized by a quasi-temperature of the electronic system (compare Figure 3.10). The DC resistivity reflects this trend by traversing the anomalous maximum.

3.4.4. Stability of the CDW gap

As seen above, intense photoexcitation of the CDW phase at $T = 10 \text{ K}$ with a fluence of $\Phi = 0.33 \text{ mJ/cm}^2$ temporarily induces a free carrier response characteristic of the normal phase. To test whether this observation indicates a photoinduced transition to the normal phase of the system, it is analyzed if the single-particle transition across the CDW gap is suppressed under the same excitation conditions.

To this end, the effects of optical pumping and thermal heating on the single-particle CDW gap transition are compared via the real part of the optical conductivity $\text{Re}(\sigma)$. Figure 3.15 reproduces the conductivity spectra for normal (red curve) and CDW phase (blue curve) from Figure 3.4(b). In addition, it shows the conductivity measured after

optical excitation of the CDW phase at $T = 10\text{ K}$ with $\Phi = 0.33\text{ mJ/cm}^2$ (dark red data points). The delay time of $t_D = 1.05\text{ ps}$ is chosen such that the free carrier conductivity corresponds to a temperature of $T = 300\text{ K}$ implying a full suppression of excitonic order. Intriguingly, the onset of the interband transition across the CDW gap remains clearly visible in this situation. The transient conductivity spectrum may be compared to a scenario, where optical pumping induces a hypothetical crossover phase (dashed line) that combines a free carrier response as expected at a temperature of $T = 300\text{ K}$ with an interband transition across the CDW gap characteristic for $T = 150\text{ K}$. The resulting conductivity spectrum closely resembles the measured data.

This observation gives a strong hint that part of the CDW order must remain present while the free carrier system exhibits an optical response characteristic for the normal phase. Thus, electronic correlations cannot be the sole cause for the band structure folding that enables the interband transition. To further corroborate this conclusion, it is analyzed how the lattice degree of freedom behaves under the same excitation conditions.

3.5. The periodic lattice deformation upon photoexcitation

While the plasmon pole witnesses the electronic order and the single-particle transition across the CDW gap is indicative for a folding of the band structure, the polarizability of back-folded phonon branches enables one to simultaneously follow the PLD [Hol77].

Figure 3.16 summarizes the phonon response of the photoexcited sample for $T = 10\text{ K}$ and $\Phi = 0.33\text{ mJ/cm}^2$, i.e. after complete quenching of excitonic correlations. Surprisingly, the PLD induced mode at $h\nu = 19\text{ meV}$ (see also Figure 3.5) remains virtually unaffected at all

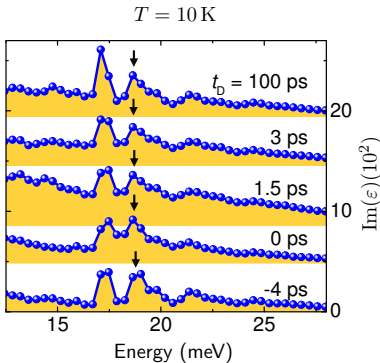


Figure 3.16:

Imaginary part of the far-infrared dielectric function at selected pump-probe delay times t_D after NIR excitation with $\Phi = 0.33\text{ mJ/cm}^2$ at $T = 10\text{ K}$. At all delay times, the phonon resonance originating from the back-folded acoustic branch remains visible (black arrows), proving the persistence of the PLD. The elevated optical conductivity found at $t_D = 1.5\text{ ps}$ (see Figure 3.8(b)) accounts for the increased background of the corresponding curve.

times t_D . This unexpected observation demonstrates that the PLD remains stable, even though Φ is sufficiently high to keep the excitonic order molten for several ps (compare Figures 3.9 and 3.10). If excitonic correlations were the main driving force of the PLD, this would be enough time for the lattice to relax into its undistorted state. Yet this is not observed. In order to achieve a melt-down of the PLD with the maximal excitation density available, the sample has to be heated to $T = 150$ K (see Figure 3.17). In contrast, the electronic order is quenched with fluences lower by one order of magnitude, even at much lower temperature.

It is instructive to compare the energy per room-temperature unit cell (UC) required to optically and thermally melt the PLD. Optical excitation with $\Phi = 0.33$ mJ/cm² corresponds to an energy deposition of ~ 15 meV/UC. In contrast, it follows from the temperature dependent specific heat [Cra78], that an energy density of 30 meV/UC is required to induce the phase transition thermally by heating the system from $T = 150$ K to $T = T_c$. This apparent discrepancy has been observed before in time resolved x-ray studies [MV11]. In light of the above results, such behavior may indeed be expected: Quenching of the excitonic order selectively excites the PLD related lattice modes to a temporarily increased quasi-temperature sufficient to melt the PLD. In addition, due to the suppressed excitonic contribution, the critical temperature of the remaining component of the CDW order may be temporarily lowered.

The far-infrared equilibrium dielectric response required for extraction of the transient phonon spectra is measured via the complex valued THz field transmission through the sample. The THz probe transients are generated and electro-optically detected using GaP as THz emitter and detector (see section 2.2.1). The time resolution in this configuration permits to trace photoinduced changes in the dielectric function occurring on a timescale of shorter than 1.5 ps (compare Figure 3.16).

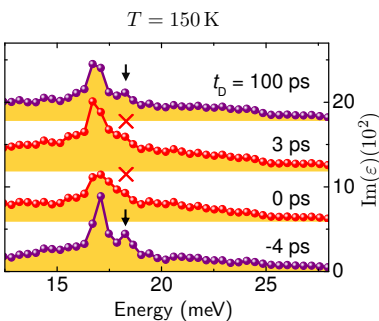


Figure 3.17:
Far-infrared spectra of $\text{Im}(\epsilon)$ after NIR excitation with $\Phi = 0.33$ mJ/cm² measured at $T = 150$ K. The suppression of the PLD-related phonon (red crosses) for $t_D = 0$ ps and 3 ps attests to a complete melting of the PLD within the corresponding time window.

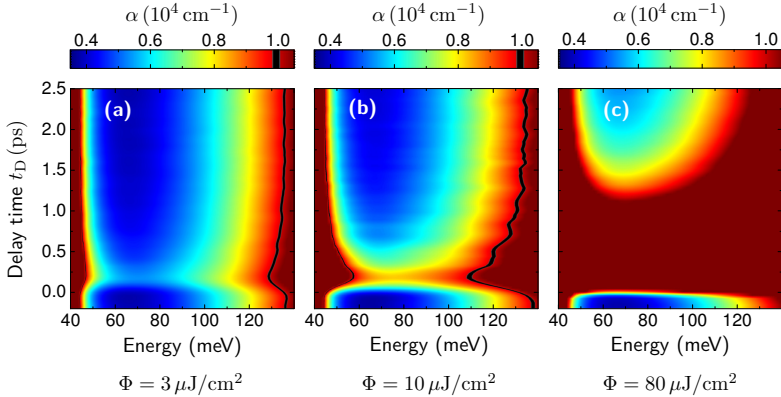


Figure 3.18: 2D-maps of the transient absorption coefficient $\alpha(\hbar\omega, t_D)$ measured at a temperature of $T = 10$ K with various pump fluences. Photoexcitation with (a) $\Phi = 3 \mu\text{J}/\text{cm}^2$ and (b) $\Phi = 10 \mu\text{J}/\text{cm}^2$ lie below the threshold fluence for suppression of the excitonic correlations while a pump fluence of (c) $\Phi = 80 \mu\text{J}/\text{cm}^2$ exceeds the threshold by a factor of 2.

3.6. Coupling of lattice and electronic orders

Both the remaining PLD and the CDW gap demonstrate that the CDW phase can exist without excitonic order. Nonetheless, lattice and electronic orders do couple, as seen next.

Optical excitation of the CDW phase at $T = 10$ K induces changes of the collective free carrier response as well as the single-particle excitations while the PLD appears unaffected. In the discussion so far, each degree of freedom is analyzed separately. In this section, the THz absorption coefficient α is studied, since it intuitively captures the absorption associated with both the free carriers and the transition across the CDW gap. Figure 3.18 shows 2D-maps of the absorption coefficient α as a function of the photon energy and the pump-probe delay time for three characteristic excitation densities. At low fluence with $\Phi = 3 \mu\text{J}/\text{cm}^2$ (Figure 3.18(a)), photoexcitation yields an increase of absorption both on the low and on the high energy side. These dynamics attest to modifications of the plasma response as discussed above and, additionally, to a red-shift of the onset of the interband transition across the CDW gap. The dynamics of $\alpha(\hbar\omega, t_D)$ on the high-frequency side monitoring the single-particle excitation gap is even more interesting for larger Φ (Figure 3.18(b)): The spectral weight above a photon energy of 100 meV is increased further, indicative of a further reduction of the energy gap. In addition, the dynamics of the CDW gap is visibly superimposed with coherent oscillations at a frequency corresponding to the

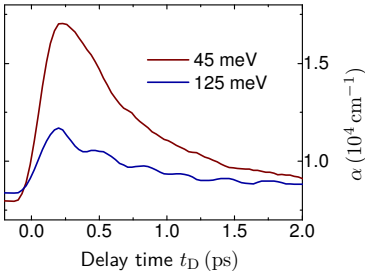


Figure 3.19:

Cuts through the 2D-map $\alpha(\hbar\omega, t_D)$ of Figure 3.18(b) recorded with an excitation fluence of $\Phi = 10 \mu\text{J}/\text{cm}^2$ at a temperature of $T = 10 \text{ K}$ along the t_D time axis at photon energies of 45 meV (red line) and 125 meV (blue line).

A_{1g} CDW amplitude mode (see below). A black contour line highlights this feature. Note that the low-frequency plasma response does not exhibit this coherent dynamics. Upon excitation with $\Phi > \Phi_{\text{th}}$ (Figure 3.18(c)) the free carrier absorption overlaps with the single-particle absorption of the CDW gap.

When one considers the CDW in 1T-TiSe₂ as the result of concerted action of excitonic correlations and Jahn-Teller-like effects, these observations can be well understood:

Optical excitation breaks the excitonically bound electron-hole pairs and thereby increases the free carrier density and decreases a jointly formed energy gap. Consequently, the plasmon pole shifts higher while the additional spectral weight from single-particle excitations extends towards lower frequencies. Upon approaching the critical excitation fluence, the collective plasma response should effectively screen low-energy transitions associated with the excitonic component of the CDW gap comparable to an excitonic Mott transition [Zim78]. The consequences are apparent in Figure 3.11(a): Excitonic correlations that contribute to the stabilization of the CDW gap are more effectively screened with an increasing density of free carriers n . Thus, charge carriers in this situation are more readily released from the bound states and add to the primary photogenerated free carriers, leading to the observed superlinear increase of n with Φ .

The coherent oscillations visible in Figure 3.18 complete this picture. Cuts through the data of Figure 3.18(b) along the time axis t_D at two representative photon energies are shown in Figure 3.19. The coherent amplitude oscillations strongly modulate the mid-infrared absorption at a photon energy of 125 meV (blue curve), while the low-frequency response at 45 meV (red curve) is not affected. When optical excitation quenches part of the excitonic correlations, the equilibrium position of the remaining CDW is suddenly relaxed, such that a coherent oscillation of the A_{1g} CDW amplitude mode around the new equilibrium position is triggered non-adiabatically. This coherent A_{1g} phonon field forces the remaining CDW order periodically out of its momentary energy minimum and thereby modulates the Jahn-Teller component of the CDW gap.

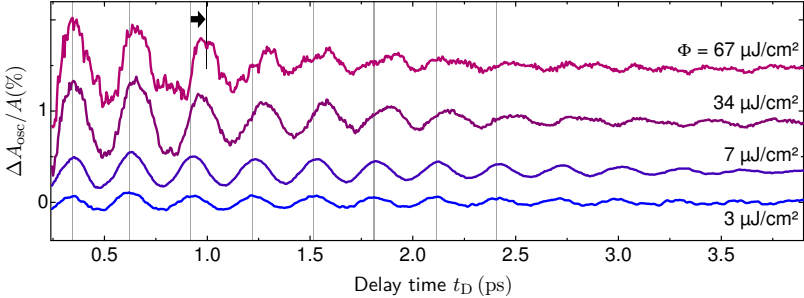


Figure 3.20: Oscillatory component $\Delta A_{\text{osc}}(t_{\text{D}})$ of the pump-induced THz transmission change $\Delta A(t_{\text{D}})$ recorded at a temperature of $T = 10\text{K}$ and various pump fluences. ΔA results from a 1D pump-probe experiment and refers to an integrated spectral range covering photon energies from 40 meV to 140 meV . Vertical gray lines mark the maxima of the waveform recorded with $\Phi = 3\text{ }\mu\text{J}/\text{cm}^2$. The black vertical line and the black arrow indicate the time difference required for three full oscillation cycles during persistent ($\Phi = 3\text{ }\mu\text{J}/\text{cm}^2$, blue line) and suppressed excitonic order ($\Phi = 67\text{ }\mu\text{J}/\text{cm}^2$, purple line).

With the physical origin of the periodic modulation for the THz response following NIR photoexcitation identified, a spectrally integrated time resolved THz transmission experiment [Kim12] is now performed to measure details of the transient oscillatory response as a function of the excitation intensity. For this study, the electro-optic sampling time t is fixed to measure the maximum field transmission amplitude A while the pump-probe delay time t_{D} is varied. This procedure captures the spectrally integrated pump-induced transient transmission change through the sample $A(t_{\text{D}})$. The oscillatory component $\Delta A_{\text{osc}}(t_{\text{D}})$ superimposed in the dynamics of $\Delta A(t_{\text{D}})$ shown in Figure 3.20 has been isolated by subtraction of exponentially decaying components from $\Delta A(t_{\text{D}})$.

$\Delta A_{\text{osc}}(t_{\text{D}})$ exhibits a frequency of 3.4 THz , for $\Phi = 7\text{ }\mu\text{J}/\text{cm}^2$ (Figure 3.21(a)), which is characteristic of the well-known A_{1g} CDW amplitude mode [Sno03, MV11]. While the oscillation is still observed for excitation densities above Φ_{th} , its amplitude increases with Φ only up to Φ_{th} (Figure 3.21(b)). This behavior is indeed expected when the CDW gap is jointly formed by excitonic correlations and Jahn-Teller effects. Following impulsive weakening of the excitonic order, the remaining PLD oscillates around a slightly relaxed potential energy minimum. This coherent dynamics modulates the Jahn-Teller component of the CDW gap. Following a complete quench of excitonic correlations, the new equilibrium position of the PLD is stabilized by Jahn-Teller effects and the oscillation

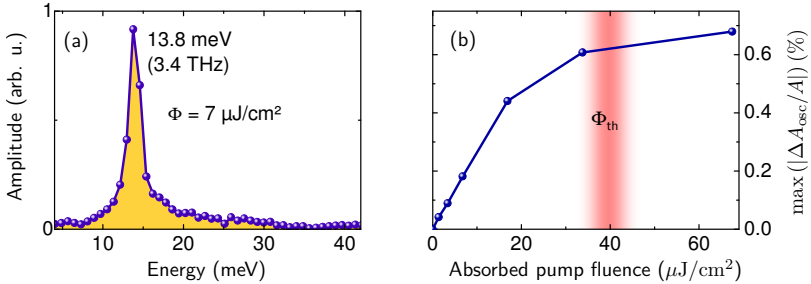


Figure 3.21: (a) Frequency spectrum of the coherent oscillations observed with a pump fluence of $\Phi = 7 \mu\text{J}/\text{cm}^2$ (compare Figure 3.20). The position of the single peak at 13.8 meV identifies the well-known A_{1g} CDW amplitude mode [MV11]. (b) Maximum amplitude of ΔA_{osc} as a function of Φ . The curve flattens at a fluence coinciding with Φ_{th} (red shaded vertical line).

amplitude, given by the pump-induced shift of the equilibrium position, remains at its maximum level. This interpretation is supported by a theoretical model (see section 3.7) predicting a reduced, but finite PLD when the excitonic order is quenched. The precise traces of the coherent oscillations are recorded at different excitation densities (Figure 3.20). The initial phase of the coherent oscillation is constant for all fluences. Yet, its frequency slightly decreases when excited with $\Phi = 67 \mu\text{J}/\text{cm}^2$ as compared to $\Phi = 3 \mu\text{J}/\text{cm}^2$. The change in frequency eventually leads to a phase retardation of $\pi/2$ after three oscillation periods at $t_D = 1 \text{ ps}$ (black arrow in Figure 3.20). Since $\Phi = 67 \mu\text{J}/\text{cm}^2$ effectively quenches excitonic correlations within this initial time window (compare Figure 3.9(b)), the restoring force in this case is mainly given by a remaining Jahn-Teller mechanism. As discussed in the next section, the pump-induced softening of the A_{1g} amplitude mode suggests a cooperative coupling between excitonic correlations and Jahn-Teller effects.

As a remark it is noticed here, that for low intensity photoexcitation, the center energy of the transition across the CDW gap may be extracted from the transient dielectric response (see appendix C). The observed behavior is in line with the above interpretation.

From the experimental point of view, all key observations can be consistently explained in the picture of combined action of excitonic correlations and a structural Jahn-Teller like effect in the formation of the CDW. In the next section it is tested whether this interpretation of the experimental results is compatible with a recent theoretical model that accounts for both contributions.

3.7. The results in the light of a 1D mean-field theory

Extensive theoretical work has aimed for a better understanding of the microscopic mechanisms that lead to the CDW phase transition in 1T-TiSe₂ [Mon09, Wez10b, Mon11, Call11, Zhu12, Zen13]. This section compares the results obtained in this work to the predictions of a mean-field model introduced by van Wezel *et al.* [Wez10b]. Both Jahn-Teller and excitonic components of the CDW order parameter are considered in this model.

3.7.1. Description of the model

The equilibrium Hamiltonian

$$H = H_0 + H_X + H_{e-l} \quad (3.4)$$

models two coupled chains of atoms with one orbital per lattice site i as schematically shown in Figure 3.22. The upper chain represents the interacting Se4p orbitals (green shapes), created by c_i^\dagger (valence electrons) and the lower chain represents the Ti3d orbitals (gray shapes), created by d_i^\dagger (conduction electrons). The energetic distance between the two atomic levels is denoted by Δ . The noninteracting tight-binding Hamiltonian H_0 describes the band structure close to the Fermi energy, with nearest-neighbor intra-chain hopping of amplitude $t/2$ in both chains and inter-chain nearest-neighbor hopping of amplitude t' . H_0 also includes local phonon modes in the c - and d -chains (phonon energy $\hbar\omega_{ph}$), created by b_i^\dagger and a_i^\dagger , respectively. The interaction terms H_X and H_{e-l} account for the nearest-neighbor couplings of the atoms of the two chains. Excitonic effects are induced by the screened Coulomb interaction potential V between a d -conduction electron and a c -valence hole:

$$H_X = -V \sum_i d_i^\dagger d_i \left[c_i c_i^\dagger + c_{i-1} c_{i-1}^\dagger \right]. \quad (3.5)$$

The Jahn-Teller electron-lattice local couplings are described by

$$H_{e-l} = \alpha \sum_i \left[(X_i^a + X_i^b)(d_i^\dagger c_i + c_i^\dagger d_i) - (X_{i+1}^a + X_i^b)(d_{i+1}^\dagger c_i + c_i^\dagger d_{i+1}) \right] \quad (3.6)$$

where α is the electron-phonon coupling constant and

$$X_i^a = \sqrt{\frac{\hbar}{2ma_L^2\omega_{ph}}}(a_i + a_i^\dagger) \quad (3.7)$$

is the displacement field operator of the atom i with mass m . a_L denotes the lattice constant.

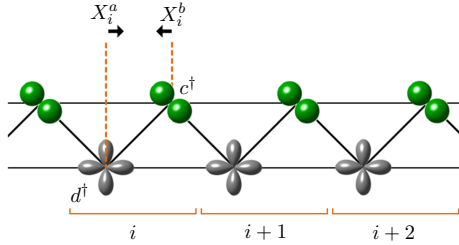


Figure 3.22: The one-dimensional double chain model introduced by van Wezel *et al.* [Wez10b] employed to analyze the influence of Jahn-Teller-like and excitonic effects on the CDW formation. Gray and green shapes correspond to Ti3d and selected Se4p orbitals, respectively. i enumerates the lattice sites. c^\dagger and d^\dagger create electrons in the Se4p and Ti3d states, respectively. The X operators describe the displacement amplitude of the corresponding atom.

Van Wezel *et al.* treat the many-body interactions H_X and H_{e-l} within the Hartree-Fock approximation and employ the Bloch theorem to derive a fully decoupled mean-field Hamiltonian that describes the charge density formation:

$$H_{\text{MF}} = \sum_{\mathbf{k}} \left(\epsilon_{\mathbf{k}} c_{\mathbf{k}}^\dagger c_{\mathbf{k}} + \eta_{\mathbf{k}} d_{\mathbf{k}}^\dagger d_{\mathbf{k}} + \beta_{\mathbf{k}} e^{i\phi_{\mathbf{k}}} d_{\mathbf{k}}^\dagger c_{\mathbf{k}} + \beta_{\mathbf{k}} e^{-i\phi_{\mathbf{k}}} c_{\mathbf{k}}^\dagger d_{\mathbf{k}} \right) + \sum_{\mathbf{k}} \hbar \omega_{\text{ph}} (a_{\mathbf{k}}^\dagger a_{\mathbf{k}} + b_{\mathbf{k}}^\dagger b_{\mathbf{k}}) + 2\alpha\tau_{\delta} \sqrt{N} (a_{\mathbf{k}=0}^\dagger + a_{\mathbf{k}=0} + b_{\mathbf{k}=0}^\dagger + b_{\mathbf{k}=0}) \quad (3.8)$$

The mean-fields are given by the average electron density per lattice site

$$\rho_c = \langle c_i^\dagger c_i \rangle \quad \rho_d = \langle d_i^\dagger d_i \rangle, \quad (3.9)$$

the charge transfer within (τ_{in}) and between (τ_{out}) the unit cells

$$\tau_{\text{in}} = \langle c_i^\dagger d_i \rangle \quad \tau_{\text{out}} = \langle c_i^\dagger d_{i+1} \rangle \quad (3.10)$$

and the mean-field lattice distortion

$$u = u_a + u_b = \langle X_i^a \rangle + \langle X_i^b \rangle. \quad (3.11)$$

The energies of the conduction and valence bands, including the excitonic energy contribution when inter-chain electron-hole pairs are present and $\rho_c \neq 1$, $\rho_d \neq 0$ are given by

$$\epsilon_{\mathbf{k}} = t \cos(ka_{\text{L}}) - \frac{\Delta}{2} + 2V\rho_d \quad \text{and} \quad \eta_{\mathbf{k}} = t \cos(ka_{\text{L}}) + \frac{\Delta}{2} + 2V(\rho_c - 1) \quad (3.12)$$

The two chains are coupled via the tight-binding band structure described by t' and, most importantly, via the electron-lattice and excitonic interactions:

$$\beta_{\mathbf{k}} e^{i\phi_{\mathbf{k}}} = t'(1 + e^{ika_{\text{L}}}) + \alpha u(1 - e^{ika_{\text{L}}}) - V(\tau_{\text{in}} + e^{ika_{\text{L}}}\tau_{\text{out}}) \quad (3.13)$$

While the band structure contribution t' dominates at $k=0$, close to the Brillouin zone boundary at $k = \pi/a_{\text{L}}$, the coupling of the two chains is dominated by both excitonic and electron-lattice interactions characterized by αu and $V\tau_{\delta}$. Here, $\tau_{\delta} = \text{Re}(\tau_{\text{in}} - \tau_{\text{out}})$ describes the inter-chain electron-hole coherence.

The above mean-field Hamiltonian is diagonalized via a standard Bogoliubov transformation [Bog47] to obtain the quasiparticles (created by $A_{\mathbf{k}}^{\dagger}$ and $B_{\mathbf{k}}^{\dagger}$) describing the hybridized excitations:

$$c_{\mathbf{k}}^{\dagger} = e^{i\phi_{\mathbf{k}}/2} \left(\cos \theta_{\mathbf{k}} A_{\mathbf{k}}^{\dagger} - \sin \theta_{\mathbf{k}} B_{\mathbf{k}}^{\dagger} \right), \quad d_{\mathbf{k}}^{\dagger} = e^{-i\phi_{\mathbf{k}}/2} \left(\sin \theta_{\mathbf{k}} A_{\mathbf{k}}^{\dagger} + \cos \theta_{\mathbf{k}} B_{\mathbf{k}}^{\dagger} \right)$$

where

$$\tan(2\theta_{\mathbf{k}}) = \frac{2\beta_{\mathbf{k}}}{\epsilon_{\mathbf{k}} - \eta_{\mathbf{k}}}. \quad (3.14)$$

After introducing shifted phonon operators ($\alpha_{\mathbf{k}}^{\dagger}$ and $\gamma_{\mathbf{k}}^{\dagger}$) the Hamiltonian can be expressed in diagonal form:

$$H_{\text{MF}} = -\frac{8\alpha^2\tau_{\delta}^2 N}{\hbar\omega_{\text{ph}}} + \sum_{\mathbf{k}} \left(E_{\mathbf{k}}^A A_{\mathbf{k}}^{\dagger} A_{\mathbf{k}} + E_{\mathbf{k}}^B B_{\mathbf{k}}^{\dagger} B_{\mathbf{k}} \right) + \sum_{\mathbf{k}} \hbar\omega_{\text{ph}} \left(\alpha_{\mathbf{k}}^{\dagger} \alpha_{\mathbf{k}} + \gamma_{\mathbf{k}}^{\dagger} \gamma_{\mathbf{k}} \right) \quad (3.15)$$

The energy dispersion of the two quasiparticle branches is given by

$$E_{\mathbf{k}}^{A,B} = \frac{1}{2} \left[(\epsilon_{\mathbf{k}} + \eta_{\mathbf{k}}) \pm \text{sgn}(\epsilon_{\mathbf{k}} - \eta_{\mathbf{k}}) \sqrt{(\epsilon_{\mathbf{k}} - \eta_{\mathbf{k}})^2 + (2\beta_{\mathbf{k}})^2} \right]. \quad (3.16)$$

In the zero temperature ground state, the lower branch is fully occupied and the higher branch is empty.

The values of the mean-fields are now determined by minimizing the total energy given by H_{MF} for each combination of the excitonic binding potential V and the Jahn-Teller coupling strength α with the mean-fields as free parameters. Thereby, ρ_c , ρ_d , τ_{in} and τ_{out} describe two coupled qubits and are constrained by translational invariance along the chains and conservation of the particle number (see appendix D).

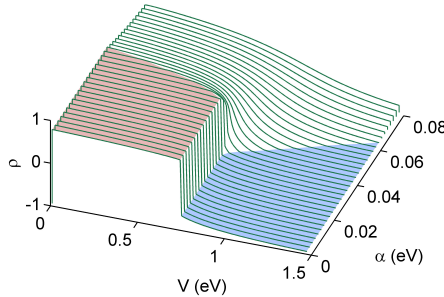


Figure 3.23: Charge transfer $\rho = \rho_c - \rho_d$ between the two bands considered in the model. The normal phase is characterized by $\rho \approx 1$ (red shaded region) while $\rho \approx -1$ describes the excitonic insulator phase (blue shaded region). The figure reproduces the results by van Wezel *et al.* for comparison (see Figure 5 in [Wez10b]).

3.7.2. The equilibrium phase diagram

The mean-fields $\rho = \rho_c - \rho_d$, τ_δ and u constitute the components of the order parameter of the model system and define the equilibrium phase diagram. Figure 3.23 and Figure 3.24 provide an overview of the different phases described by the model.

As the first component of the composite CDW order parameter, the excitonic charge transfer ρ from the valence to the conduction band as a function of V and α is reproduced (Figure 3.23). The normal phase with electrons effectively only populating the valence band is characterized by $\rho \approx 1$ (red shaded region). For a sufficiently high value of V , an excitonic insulator is formed when α is sufficiently low. This phase is characterized by $\rho \approx -1$ (blue shaded region) and describes an almost complete charge transfer from the valence to the conduction band corresponding to the existence of excitonically bound electron-hole pairs.

To capture all components of the CDW order parameter, the analysis of van Wezel *et al.* [Wez10b] is extended by calculation of the PLD mean-field amplitude u for each combination of V and α (Figure 3.24(a)). Without excitonic effects ($V = 0$), a positive u ($\alpha > 0.045$ eV) describes a purely Jahn-Teller-like structural phase transition. For nonzero V , both cooperation and competition between excitonic and Jahn-Teller effects can occur: In the range $0 \text{ eV} < V < 0.75 \text{ eV}$, an increase of V enhances the PLD and lowers the critical value of α for the structural CDW phase transition. Thus, in this region of V with a nonzero PLD present, excitonic correlations and Jahn-Teller effects cooperate to form a combined Jahn-Teller excitonic CDW. In contrast, upon further increase of V ,

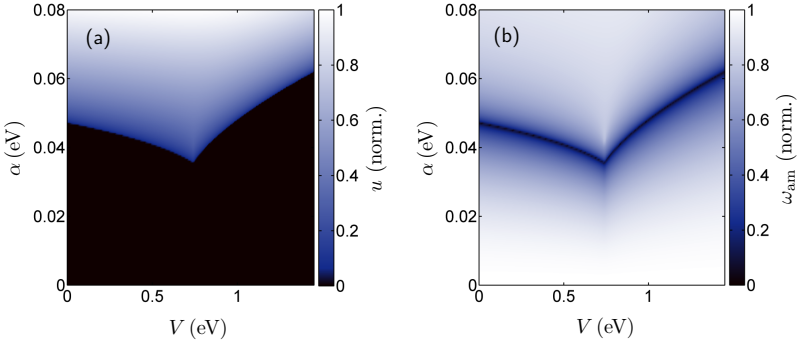


Figure 3.24: (a) 2D-map of the mean-field lattice distortion u as a function of V and α . For $V > 0$, a finite value of u characterizes a CDW resulting from both Jahn-Teller and excitonic contributions. (b) 2D-map of the CDW amplitude mode frequency ω_{am} normalized to the uncoupled oscillation frequency of the normal phase. The mode softens to zero frequency at the structural phase transition.

excitonic order and Jahn-Teller effects compete, as apparent from the formation of more excitons at the expense of a reduced PLD (compare Figures 3.23 and 3.24(a)). Ultimately, in the excitonic insulator phase, the PLD is zero since no direct exciton-phonon coupling is considered in the model.

To qualitatively compare the experimentally observed softening of the CDW amplitude mode, the frequency ω_{am} of the amplitude mode as a function of V and α is calculated by variation of u around its equilibrium value (Figure 3.24(b)). As one would expect for a mean-field transition, a softening to zero frequency occurs at the onset of the structural phase transition. When u becomes nonzero, the mode changes its symmetry from a normal phase lattice mode to the CDW amplitude mode.

3.7.3. Modeling NIR photoexcitation

To compare the model predictions with the experimental data, the components of the order parameter are associated with experimentally accessible quantities. The free carrier density n can be related to ρ since both are directly connected to the exciton density (both n and ρ are reduced/increased by exciton formation/destruction). As discussed in section 3.6, the low-energy spectral wing of the single-particle transition across the CDW is observed in the experiment. In the model, this transition corresponds to the lowest energetic distance between the two quasiparticle branches, occurring at $k = \pi/a_{\text{L}}$. This

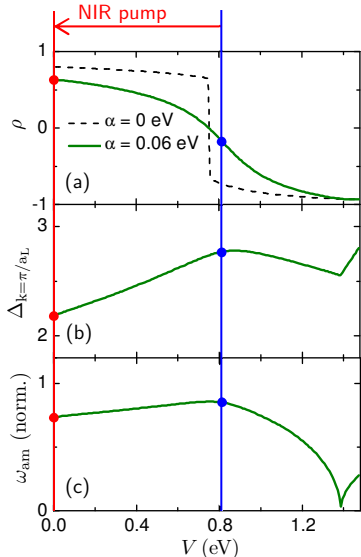


Figure 3.25:

(a) ρ as a function of V for two selected values of α . Reduction of V by Coulomb screening due to optically generated free carriers leads to an increase of ρ . This holds for both the excitonic insulator ($\alpha = 0$, dashed line) and the coupled Jahn-Teller excitonic CDW ($\alpha = 0.06$ eV, dark green line). The blue vertical line indicates a possible value of V before a pump-induced quench to $V = 0$ (red vertical line). (b) Energy gap at $k = \pi/a_L$ as a function of V . For a cooperatively coupled CDW ($V \lesssim 0.8$ eV), the quench of V reduces the gap. (c) Frequency of the amplitude mode w_{am} as a function of V . For an initial value of $V \lesssim 0.8$ eV, the quench reduces w_{am} . At the structural phase transition from a combined CDW to an excitonic insulator ($V \approx 1.4$ eV) the amplitude mode softens to zero frequency and changes its symmetry to a normal phase lattice mode.

energy gap, $\Delta_{k=\pi/a_L}$, also scales with both V and α . The frequency of the A_{1g} amplitude mode is directly captured by the model via the PLD amplitude mode frequency ω_{am} .

NIR photoexcitation creates high energy electron-hole pairs with an energy much larger than the CDW gap. These carriers relax by electron-electron scattering, exciting further low-energy quasiparticles via cascading effects. The following analysis assumes that photogenerated free carriers lead to a reduction of the excitonic electron-hole interaction potential by Coulomb screening. This scenario is modeled by a reduction of V while keeping α fixed. The pump-induced change in the exciton energy V may be thought of as an “interaction quench” with a finite duration. A direct change of the charge imbalance $\rho_c - \rho_d$ by excitation of charge carriers that do not directly participate in the formation of the CDW is not considered here.

Even with this simplest possible approach the model qualitatively accounts for all observations made in the experiment. A very general prediction is the release of free carriers induced by the destruction of excitons following a reduction of V , independent of the exact value of α (Figure 3.25(a)). In the case of $\alpha = 0$ (dashed line), a step-like increase of n is expected upon optically induced suppression of V below the critical value required to stabilize the excitonic insulator phase. For $\alpha = 0.06$ eV (green line), the increase of n at a reduction of V is more continuous. This aspect enables a qualitative understanding of the

dependence of n on the excitation fluence Φ (Figure 3.11(a)): A linear component in $n(\Phi)$ accounts for the primary photogenerated free carriers, while the superlinear dependence seen at low fluences is a result of an increasing destruction of excitons. Upon approaching a full quench of V to zero, the number of additional free carriers released from excitons levels off until ultimately no more excitons can be broken and only the linear dependence remains. Furthermore, the approach correctly reproduces the behavior of the CDW gap. As shown in Figure 3.25(b), in the regime of a cooperative Jahn-Teller excitonic CDW ($V < 0.8$ eV for $\alpha = 0.06$ eV), a reduction of V continuously decreases $\Delta_{k=\pi/a_L}$ (green line). Notably, even at a full quench of V , indicated in Figure 3.25 by the transition from $V = 0.8$ eV (blue vertical line) to $V = 0$ (red vertical line), the gap remains at an elevated value due to the remaining Jahn-Teller component of the CDW (compare Figure 3.15).

As shown next, with this remaining component of the CDW order, the model also explains the experimentally observed softening of the A_{1g} amplitude mode after photoexcitation. Figure 3.25(c) shows the frequency of the model CDW amplitude mode ω_{am} as a function of V for $\alpha = 0.06$ eV. Excitonic correlations stiffen the amplitude mode in the regime of a cooperative CDW ($V < 0.8$ eV). For higher values of V , the mode softens due to the competition of Jahn-Teller effects and excitonic correlations. Thus, assuming photoinduced reduction of V in the cooperative CDW regime, the model correctly accounts for the observed softening of the amplitude mode after photoexcitation. Furthermore, the saturation of the oscillation amplitude at Φ_{th} (see Figure 3.21(b)) can be identified as another consequence of a quench of V . Since the maximum amplitude of the PLD oscillation is given by the photoinduced shift of the PLD equilibrium position, the increase of the oscillation amplitude stalls when the new equilibrium position, given by a purely Jahn-Teller stabilized CDW, becomes more robust against photoexcitation.

Finally, the coherent excitation of the A_{1g} amplitude mode can be modeled by forcing u out of its minimum energy value by Δu (with $\Delta u \ll u$). For minimized total energy with constrained u , the relative change of $\Delta_{k=\pi/a_L}$ is one order of magnitude larger than the relative change of ρ . This is in line with the observation that the energy gap is visibly modulated by the coherent oscillations of the amplitude mode while the free carrier response remains unaffected (compare section 3.6). Thus, it is the Jahn-Teller component of the CDW gap that is modulated by the coherent oscillation of the amplitude mode.

In conclusion, a quench of the excitonic component of a cooperatively coupled excitonic Jahn-Teller CDW, modeled by a quench of the excitonic binding potential, qualitatively explains the key experimental observations. In perspective, the presented data may provide a foundation and benchmark for the development of advanced quantum-kinetic theories. If based on a full 3D model such as introduced recently by Zenker *et al.* [Zen13], even a quantitative agreement with the results presented in this work may be achieved.

3.8. The origin of the charge density wave in 1T-TiSe₂

In conclusion, the microscopic origin of the lattice commensurate charge density wave in 1T-TiSe₂ is consistently identified in this work by means of femtosecond NIR-pump/multi-THz-probe spectroscopy. Electronic ordering and a reconstruction of the crystal lattice, two coupled components of the CDW order parameter, are separately monitored via their individual THz fingerprints after controlled perturbation of the system with a 12-fs NIR pump pulse. The free carrier plasma response is employed as a measure of the electronic component of charge ordering. The observed photoinduced modifications of the free carrier system attest to an excitonic contribution to charge ordering. In addition, back folded phonon modes are harnessed as a measure of the structural component of the charge density order parameter. It is demonstrated, that photoexcitation can drive the system into a highly non-thermal phase in which the structural component of the charge ordered phase persists in a coherently excited state even when the excitonic order is quenched. The experimental results strongly indicate, that the joint action of excitonic electron-hole correlations and a structural Jahn-Teller-like effect induces the charge density wave phase transition in 1T-TiSe₂. A quantum-mechanical mean-field model [Wez10b], which is extended to describe the influence of photoexcitation on the excitonic and structural degrees of freedom, strongly corroborates this interpretation of the experimental data.

Chapter 4

Phonon and quasiparticle dynamics in superconducting $\text{YBa}_2\text{Cu}_3\text{O}_{6.93}$

This chapter presents a multi-THz study of femtosecond phonon and quasi-particle dynamics in superconducting $\text{YBa}_2\text{Cu}_3\text{O}_{6.93}$. Following NIR photoexcitation, the THz probe pulse simultaneously traces the spectral signatures of the superconducting gap, quasi-particle excitations and two specific phonon modes. The dynamics of the phonon line shapes permits monitoring vibrational occupations with a femtosecond resolution and to single out the coupling to the electronic system. The data indicate extremely fast electron-phonon scattering in $\text{YBa}_2\text{Cu}_3\text{O}_{7-\delta}$ in contrast to the usual assumption of a two-temperature model [All87, Kab08]. This part of the work has been published in *Physical Review Letters* [Pas10].

4.1. Unconventional superconductivity

4.1.1. A short overview

The strength of a purely phonon-based mechanism for the formation of superconducting Cooper-pairs is limited by the phonon frequencies in solids. In terms of the BCS theory, this insight fueled the widespread assumption that a transition temperature for superconductivity of $\gtrsim 30\text{ K}$ should not be observable [Car03]. This conception was falsified in 1986, when Bednorz and Müller discovered high-temperature superconductivity in cuprates [Bed86]. The researchers expected superconductivity in these materials due to strong electron-phonon coupling indicated by a huge Jahn-Teller distortion. Initially, Bednorz and Müller found an inexplicably high critical temperature of 30 K in the system

Ba-La-Cu-O. Shortly after, a transition temperature of 93 K was reported for Y-Ba-Cu-O [Wu87]. Currently, the highest transition temperature of 164 K is achieved in Hg-Ba-Ca-Cu-O under pressure [Gao94]. Bednorz and Müller were awarded with the Nobel prize already one year after their discovery. The latest experimental milestone was set in 2008, when Kamihara *et al.* [Kam08] reported a superconducting phase at 26 K in fluorine-doped La-Fe-As-O. This marked the beginning of worldwide efforts to investigate the new family of iron-based “pnictide” superconductors [Pag10, Dai12, Kim12]. Given the strong magnetism of iron and considering the usually antagonistic relationship between superconductivity and magnetism, the observation of high transition temperatures in these systems was completely unexpected. This again proved, that the fundamental understanding of the origins of unconventional superconductivity needs significant improvement [Pag10].

After almost thirty years of extensive research, the mechanism that leads to the formation of an unconventional superconducting condensate still remains elusive. Besides the relevance of a variety of many-body phenomena, such as spin-, charge- or stripe-ordered phases or the pseudo gap, also the role of electron-phonon coupling in the pairing mechanism remains debated. Some theories assume that high-temperature superconductivity may occur entirely without the influence of lattice vibrations. In these scenarios, the virtual exchange bosons that bind the electrons into Cooper-pairs are sought among purely electronic elementary excitations, such as fluctuating magnons [And07, Mon07] or interorbital pair hopping excitations [Ste11]. A certain role of phonons in the formation of a superconducting condensate in some cuprates is evidenced by various experiments, including ARPES [Lan01, Cuk04, Iwa08], inelastic neutron scattering [Rez06], tunneling [Lee06] and Raman [Ope99] spectroscopic techniques. The presence of an isotope effect on the transition temperature [Bat87a, Bat87b] and strong anomalies of certain phonon modes in cuprates across the phase transition [Ber00] indicate appreciable interaction between the condensate and the lattice vibrations. Time-resolved photoemission results have suggested that there is a subset of phonon modes (about 20% of total number) which exhibit stronger coupling to the electrons [Per07]. As this evidence was indirectly deduced from the evolution of a quasi-equilibrium electronic temperature, the character of the strongly and weakly coupled phonons could not be identified.

Here, femtosecond multi-THz spectroscopy is employed to study the ultrafast interplay of electrons and two specific phonon modes in optimally doped $YBa_2Cu_3O_{6.93}$. This experiment aims to answer the question of whether there exist separate timescales (i.e. a temporal hierarchy) of the electron-electron and electron-phonon scattering processes in the non-equilibrium system. It is shown, that both scattering processes occur at the same timescale of 150 fs, demonstrating extremely fast electron-phonon scattering. This stands in contrast to the assumptions of two- or three-temperature models [Kab08, Per07].

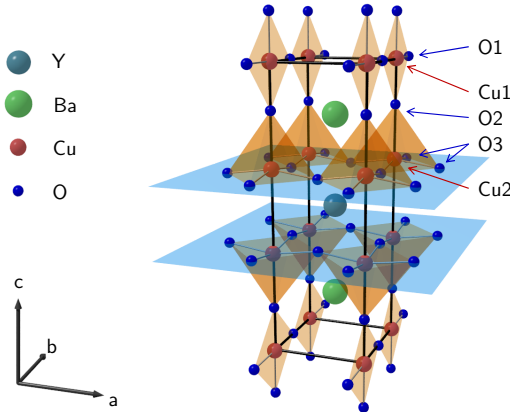
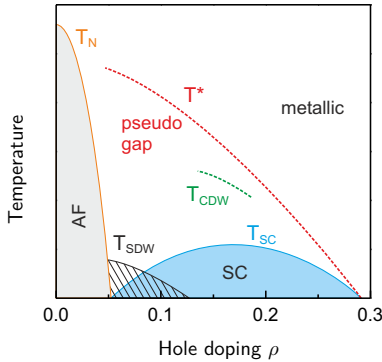


Figure 4.1: Crystal structure of orthorhombic $\text{YBa}_2\text{Cu}_3\text{O}_7$. The black frame contains a single unit cell. The doping level δ (here $\delta = 0$) is controlled by the amount of oxygen ions occupying the chains along the b crystal axis (O1). Cu2 and O3 atoms form the two-dimensional superconducting planes (highlighted by blue surfaces).

4.1.2. Cuprate superconductors and $\text{YBa}_2\text{Cu}_3\text{O}_{7-\delta}$

Cuprates are the most thoroughly studied class of high temperature superconductors and currently host the compound with the highest observed transition temperature [Gao94]. Cuprates have one or more CuO₂ planes in their structure which are separated by layers of other atoms (Ba, O, La, ...). In the planes, each copper ion is covalently bound to four oxygen ions. Unconventional superconductivity is most likely related to processes occurring in the CuO₂ planes, with the other layers solely forming charge reservoirs. Their chemistry determines the type and the amount of charge carriers in the planes. The critical temperature scales with the number of CuO₂ planes that are within a short distance of each other [Hot13].

Figure 4.1 depicts the unit cell of $\text{YBa}_2\text{Cu}_3\text{O}_{7-\delta}$. The lattice constants are $a = 3.82 \text{ \AA}$, $b = 3.89 \text{ \AA}$ and $c = 11.68 \text{ \AA}$ [Sax09]. O1 – Cu1 chains along the crystal b -axis constitute the charge reservoir. The superconducting CuO₂ planes (highlighted by blue surfaces in Figure 4.1) are formed by O3 and Cu2. Increasing of the amount of O1 leads to an increase in the effective valence of the plane coppers Cu2 due to a transfer of electrons from the planes to the chains. This is equivalent to a hole-doping of the superconducting planes (denoted by the hole concentration ρ per Cu2). When all O1 positions are filled (at $\delta = 0$, corresponding to $\rho = 0.21$), the hole doping can be further increased by partial substitution of the trivalent Y³⁺ ions with bivalent ions, e.g. Ca²⁺.

**Figure 4.2:**

Schematic phase diagram of $YBa_2Cu_3O_{7-\delta}$. Superconductivity (SC) occurs in the region covered by the superconducting dome (light blue area). The orange curve indicates the Néel temperature T_N of the antiferromagnetic (AF) insulating phase. T_{SDW} marks the critical temperature for a spin ordered phase (hatched area). T_{CDW} and T^* indicate the critical temperatures for a charge ordered and a pseudogap phase, respectively.

The value of ρ decisively influences the electronic properties of the system. Figure 4.2 schematically depicts the various phases of $YBa_2Cu_3O_{7-\delta}$ that can be reached by tuning of ρ and the temperature. Superconductivity occurs at doping levels $0.05 < \rho < 0.27$. The critical temperature strongly depends on ρ , forming the characteristic “superconducting dome” in the ρ - T phase diagram [Cav90, Hüf08]. An O1 oxygen deficiency of $\delta = 0.07$ is referred to as “optimal doping” since it yields the maximum transition temperature for superconductivity of $T_c = 93$ K. At doping levels that allow a superconducting phase, an incommensurate charge ordered phase exists in a temperature range above the critical temperature for superconductivity [Cha12]. At low hole-doping levels ($\rho < 0.05$), the system enters an antiferromagnetic insulating phase with the Néel temperature increasing with a further reduction of ρ . For doping levels $\sim 0.045 < \rho < 0.07$, an incommensurate spin ordered phase exists [Hau10]. This phase does not occur together with the antiferromagnetic phase but can be simultaneously present with superconductivity [Cha12]. The pseudogap “phase” is observed in a temperature region above the superconducting dome. For further details on the observed phases and quantitative phase diagrams of $YBa_2Cu_3O_{7-\delta}$ see e.g. [Hüf08, Hau10, Cha12, Hot13].

4.2. The spectral hallmarks of superconductivity in the dielectric response of $YBa_2Cu_3O_{6.93}$

Due to the layered structure, the dielectric response of $YBa_2Cu_3O_{7-\delta}$ is highly anisotropic. The in-plane response for an electric probe field \mathbf{E} perpendicular to the crystal c -axis is dominated by the superconducting planes. Figure 4.3(a) shows the real part of the in-plane ($\mathbf{E} \perp c$) optical conductivity σ in the normal and superconducting phases as measured

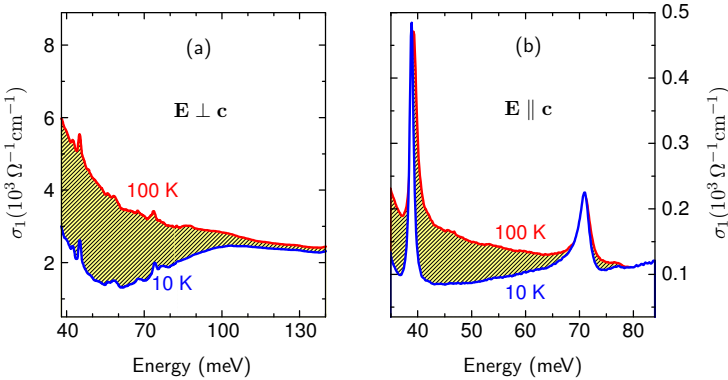


Figure 4.3: Optical conductivity $\sigma_1(\omega)$ of $YBa_2Cu_3O_{6.93}$ in the superconducting ($T = 10\text{ K}$, blue curve) and normal ($T = 100\text{ K}$, red curve) states for (a) $\mathbf{E} \perp c$ and (b) $\mathbf{E} \parallel c$ as measured by ellipsometry¹[Ber04]. The modes centered at 39 meV and 71 meV in (b) correspond to the bond-bending and apex oxygen vibrations, respectively. The yellow shaded areas mark the loss of conductivity induced by the opening of a superconducting gap.

by ellipsometry [Ber04]. Above T_c , the metallic conductivity of the cuprate planes yields a Drude-like conductivity. When the temperature is decreased below T_c , σ_1 drops at energies $\hbar\omega < 110\text{ meV}$ due to the opening of a superconducting gap [Bor04, Bas05]. A Drude-like contribution persists at the low-energy side of the response even at $T = 10\text{ K}$, as it is expected for a superconducting gap with d -wave symmetry [VH95, Tsu00], where nodal quasi-particles exist at finite temperatures. According to oscillator sum rules for the optical conductivity [Dre02], the spectral weight defined by the hatched area in Figure 4.3(a) is proportional to the density of condensed quasi-particles [Bas05].

While the in-plane response is dominated by electronic excitations, their contribution to the inter-plane optical conductivity ($\mathbf{E} \parallel c$) is reduced by one order of magnitude, as seen in Figure 4.3(b). This is why two infrared-active phonon modes of B_{1u} symmetry appear prominently on top of the electronic background: (i) The narrow resonance at an energy of 39 meV is caused by Cu-O bond bending involving an in-phase motion of all oxygen ions within the cuprate bilayers (O3 in Figure 4.1) against the central yttrium ion. (ii) Collective vibrations of the apical oxygen ions (O2 in Figure 4.1) located between the bilayers and the chains account for the conductivity maximum centered at an energy of 71 meV [Liu88, Bat89]. The bond-bending mode exhibits an anomalous blue shift and a slight broadening (see Figure 4.3(b)) as the system is heated towards T_c .

¹Data were provided by C. Bernhard, Dept. of Physics, Univ. of Fribourg, 1700 Fribourg, Switzerland.

[Lit92, Sch95, Ber00, Mun99]. At the same time the apex line changes from an asymmetric shape in the superconducting state to an almost symmetric one above T_c [Sch95]. The physical origin of the latter phenomenon is explained by the coupling between optical phonons and the interlayer Josephson plasmon [Mun99]. This collective oscillation of the superconducting condensate along the crystal c -axis, renormalizes the phonon parameters by modifying effective local fields. In the case of the apex mode, the dominant effect is a strong increase of the phonon asymmetry which, thus, quantifies the coupling of this mode to the Josephson plasmon and scales with the density of the superconducting condensate. The eigenfrequency of the apex phonon ω_0 , on the other hand, shows a continuous decrease with increasing temperature [Sch95]. This red-shift is characteristic of an anharmonic lattice potential which softens for larger vibrational amplitudes. Consequently, the frequency shift of the apex phonon may be exploited as a sensitive probe of its transient vibrational occupation after photoexcitation.

4.3. Preparations for two-time THz studies

The single crystal under study² of $YBa_2Cu_3O_{6.93}$ was grown by top-seeded solution growth [Yao97]. The sample was annealed for 72 hours in flowing oxygen at a temperature of 500 °C and returned to room temperature by furnace cooling to obtain optimally doped crystals. NIR-pump/THz-probe experiments are performed in reflection geometry (see Figure 4.4) on as-grown surfaces of the crystal with an area of about $2 \times 2 \text{ mm}^2$. One of these adjacent surfaces is oriented parallel, the other perpendicular, to the c -axis of the twinned crystal. The measurements are taken with s -polarized THz pulses and a p -polarized NIR pump, both incident at an angle of 30°. Thus, the pump is mostly polarized in the ab -plane. The polarization of the THz probe field can be chosen as $\mathbf{E} \perp c$ or $\mathbf{E} \parallel c$ by aligning the sample accordingly. A homogeneous lateral excitation profile is ensured

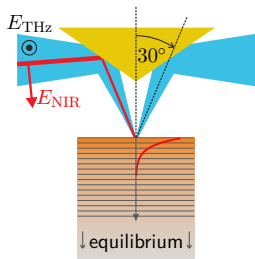


Figure 4.4:

Experimental arrangement for reflection-type NIR-pump/THz-probe studies. The setup is integrated into the LH₂ flow cryostat (see Figure 2.5). The red curve indicates the model excitation profile of the sample.

²Samples were provided by X. Yao, Dept. of Physics, Shanghai Jiao Tong Univ., Shanghai 200240, China.

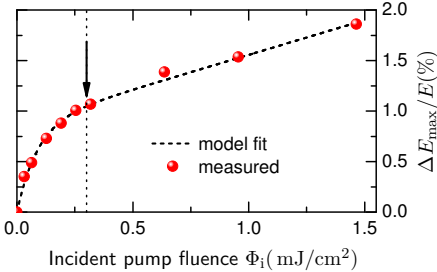


Figure 4.5:

Maximum pump-induced change of the reflected electric field for $\mathbf{E} \perp c$ as a function of the incident pump fluence. The arrow indicates the pump fluence of 0.3 mJ/cm^2 used for the two dimensional pump-probe experiments. The pump-probe delay time t_D is kept fixed at 0.2 ps .

by setting the diameter of the NIR pump focus twice the size of the THz probe focus of $\sim 75 \mu\text{m}$. In the following, the photoexcitation intensity is stated as incident fluence Φ_i .

A transfer-matrix formalism is employed to extract the optical conductivity $\sigma(\hbar\omega, t_D)$ in the photoexcited state from the measured pump-induced changes in the complex THz reflectivity. An inhomogeneously excited surface layer is treated as a stack of much thinner layers with a homogeneous refractive index as shown by gray lines in Figure 4.4. The model excitation profile in z -direction is described by an exponential decay with a length scale of $0.1 \mu\text{m}$ (sketched by the red curve in Figure 4.4) to account for the absorption length of the pump light [Kab99]. The transient THz optical response is determined by numerical inversion of the expression for the complex THz reflectivity, as described in section 2.2.2. Thereby, the dielectric response measured by ellipsometry is employed to describe the reflectivity of the unexcited system.

In order to determine the pump fluence that ensures full suppression of superconductivity and simultaneously keeps thermal heating of the sample low, the dependence of the maximal pump-induced change of the reflected THz transients ΔE_{\max} on Φ_i is studied prior to two-dimensional pump-probe experiments. As seen in Figure 4.5, the pump-induced change as a function of Φ_i shows a saturation behavior combined with a linear increase. This dependence can be phenomenologically fitted by the following equation

$$\Delta E_{\max}(\Phi_i) = A \left(1 - e^{-\Phi_i/\Phi_{\text{sat}}} \right) + B_{\text{lin}} \Phi_i. \quad (4.1)$$

The first term in equation (4.1) describes the depletion of the superconducting condensate characterized by the saturation fluence Φ_{sat} . The linear second term is related to a direct photoinduced change in the quasiparticle density and the suppression of a pseudogap (see section 4.4). Fitting the experimental data (red spheres in Figure 4.5) results in a saturation fluence of $\Phi_{\text{sat}} = 0.1 \text{ mJ/cm}^2$. A value of $\Phi_i = 0.3 \text{ mJ/cm}^2$ clearly exceeds the saturation threshold while it keeps thermal heating at a negligible level and thus is chosen for the detailed two dimensional experiments presented in the next sections.

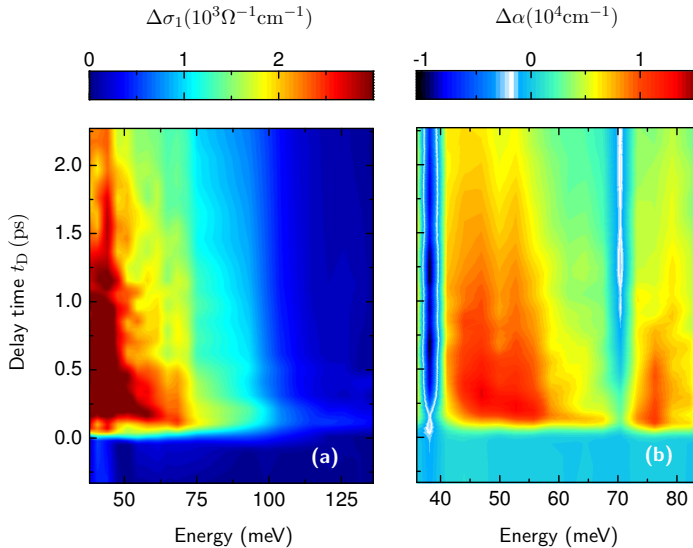


Figure 4.6: 2D NIR-pump/THz-probe data: (a) transient pump-induced changes of the real part of the optical conductivity $\Delta\sigma_1(\hbar\omega, t_D)$ as a function of the photon energy and the pump-probe delay time t_D for $\mathbf{E} \perp c$. (b) Corresponding changes of the absorption coefficient $\Delta\alpha(\hbar\omega, t_D)$, for $\mathbf{E} \parallel c$. Both measurements are performed at $T = 20$ K with $\Phi_i = 0.3$ mJ/cm².

4.4. Phonons and quasi-particles after photoexcitation

Figures 4.6 (a) and (b) depict the ultrafast pump-induced change in the optical response induced by NIR photoexcitation with a fluence of $\Phi_i = 0.3$ mJ/cm² at a sample temperature of $T = 20$ K.

The transient change of the in-plane response shown in panel (a) is discussed first. The pump pulse barely affects the high energy side of $\sigma_1(\hbar\omega)$ whereas the conductivity is enhanced below an energy of 110 meV due to the contribution of photogenerated quasiparticles. It is instructive to compare the absolute size and the spectral shape of the pump-induced conductivity changes to the conductivity difference between the superconducting and normal states (figure 4.7(a)). A snapshot of $\Delta\sigma_1$ taken at a delay time of $t_D = 1.5$ ps (red curve) perfectly matches the conductivity difference between the superconducting and the normal state (black curve), indicating a pump-induced phase transition to the normal phase and a full suppression of the superconducting gap.

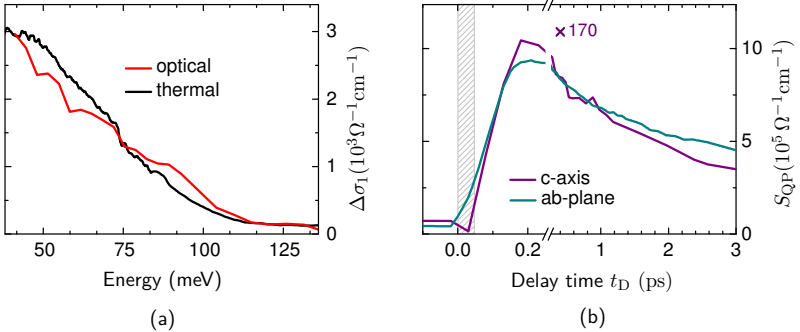


Figure 4.7: (a) Difference in the real part of the optical conductivity between normal and superconducting states (black curve) for $\mathbf{E} \perp c$ and pump-induced conductivity change $\Delta\sigma_1(\hbar\omega, t_D)$ measured at delay time $t_D = 1$ ps after photoexcitation (red curve). (b) Dynamics of the photo-induced quasi-particle spectral weight as a function the delay time t_D . Cyan curve: spectral weight for $\mathbf{E} \perp c$ integrated from 40 meV to 130 meV. Purple curve: spectral weight (scaled by factor 170) for $\mathbf{E} \parallel c$ between 45 meV and 60 meV. The experimental time resolution is indicated by the hatched area.

The temporal evolution of the change of the spectral weight, $S_{\text{QP}} = \int \Delta\sigma_1(\hbar\omega, t_D) d\omega$, in an energy window from 40 meV to 130 meV is shown in Figure 4.7(b). Interestingly, S_{QP} reaches its maximum with a delay of 150 fs, which is distinctly slower than the experimental time resolution of 40 fs. These data present a direct observation of the quasi-particle density generated during the pair-breaking cascade on the inherent time scale. The subsequent decay is described well by two exponential functions with time constants of 0.4 ps and 3.7 ps, respectively. The slow part corresponds to recondensation of quasi-particles into Cooper-pairs, whereas the fast component survives even above T_c and was associated to the recovery of a pseudogap [Dem99, Kai00].

As seen in Figure 4.6(b), the situation for $\mathbf{E} \parallel c$ is yet richer in detail. While all essential features discussed in the following are also evident in $\Delta\sigma_1(\omega, \tau)$, the 2D map of the transient absorption change $\Delta\alpha(\hbar\omega, t_D)$ illustrates the photoinduced dynamics most obviously: Besides a broadband quasi-particle contribution featuring a similar spectral profile as in the case of $\mathbf{E} \perp c$, two narrow minima are superimposed at energies of 38 meV and 72 meV. These are the fingerprints of pump-induced modifications of the two phonon resonances. As evident from the 2D data, the various contributions to the total response follow clearly different dynamics: The spectral weight of the quasi-particles integrated

in the energy range from 45 meV to 60 meV, i.e. between the phonon resonances, shows the same temporal trace as the in-plane conductivity (see Figure 4.7(b)). In contrast, the pump-induced changes of the phonons are delayed. The most striking difference is imprinted on the apex phonon which exhibits its maximum change as late as 1 ps after photoexcitation (figure 4.6(b)).

To go beyond this qualitative observation, the line shape of the phonons is analyzed to single out the microscopic mechanisms underlying the pump-induced phonon anomaly.

4.5. Analysis of the transient phonon lineshapes

4.5.1. Excitation dynamics of the apex mode

Figure 4.8 shows selected spectra of the real and imaginary part of the c -axis conductivity in the vicinity of the apex phonon resonance. Below T_c , $\sigma_1(\hbar\omega)$ features a characteristic asymmetric lineshape (Figure 4.8(a)).

For a quantitative description, the dielectric response is modeled as the sum of a broadband background electronic conductivity $\sigma_{\text{el}}(\omega)$ and a phenomenological model [Hum00] of the phonon resonance:

$$\sigma(\omega) = \sigma_{\text{el}}(\omega) - \epsilon_0 S \frac{(\omega A + i\omega_0^2)\omega}{\omega_0^2 - \omega^2 - i\omega\gamma}, \quad (4.2)$$

The phonon contribution (second term) is defined by the oscillator strength S , the eigenfrequency ω_0 , and the damping γ . The parameter A accounts for the peculiar asymmetry of the lineshape below T_c . The damping $\gamma = 2\pi \times 0.5 \text{ THz}$ is found to be almost temperature independent and is not considered here further. In order to reduce the number of free parameters, the quasi-particle background $\sigma_{\text{el}}(\omega)$ is considered as a locally linear function of frequency (first term in equation (4.2)).

The requirement to reproduce both real and imaginary parts of the spectra simultaneously imposes strict boundaries on the three remaining fit parameters S , ω_0 , and A . As seen in figures 4.8(a) and (b), the equilibrium mid infrared response of $YBa_2Cu_3O_{6.93}$ can be described convincingly with equation 4.2.

Figures 4.9 (a) and (b) show the resulting fit parameters A and ω_0 as a function of temperature. The asymmetry sharply decreases upon heating the system towards T_c . Above T_c , no further change is observed, owing to the absence of the Josephson plasmon. The increasing thermal occupation of the phonon mode upon heating manifests itself as a continuous decrease of its eigenfrequency, apart from a small anomaly around T_c .

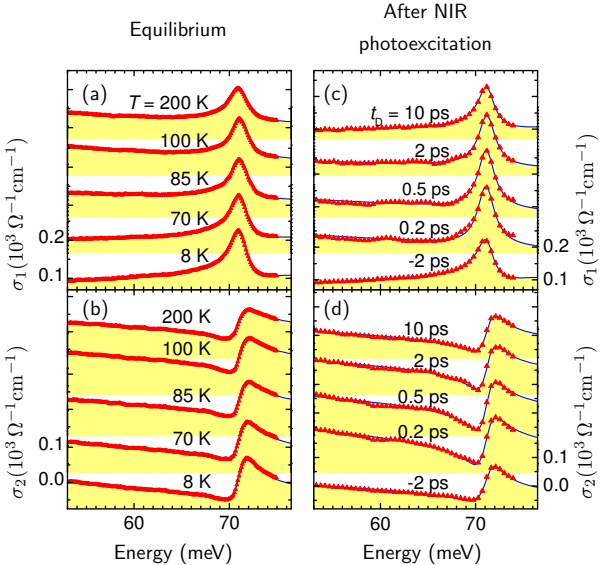


Figure 4.8: Spectra of the optical conductivity $\sigma_1(\hbar\omega)$ and $\sigma_2(\hbar\omega)$ of $\text{YBa}_2\text{Cu}_3\text{O}_{6.93}$ for $\mathbf{E} \parallel c$: (a) and (b) show the equilibrium spectra for selected temperatures. (c) and (d) show the transient spectra at selected pump-probe delay times t_D measured at $T = 20\text{ K}$ with $\Phi = 0.3\text{ mJ/cm}^2$. The solid lines show the numerically adapted curves according to equation (4.1).

The model function of equation 4.2 can also be numerically adapted to the transient complex conductivity spectra with high confidence, as shown in figures 4.8 (c) and (d) for representatively selected pump-probe delay times. This allows one to map out pump-induced modifications of the phonon parameters on a femtosecond scale.

Starting from the superconducting state (blue curve in Figure 4.9 (d)), the asymmetry of the apex mode decreases within $t_D \leq 150\text{ fs}$, following the depletion of the superconducting condensate. Analogously, the relaxation to the initial line shape asymmetry follows the recovery of the superconducting gap with a typical time constant of about 4 ps. This confirms a coupling to the Josephson plasmon as the microscopic origin of the asymmetry. Note that unlike in a thermal transition to above T_c , ultrafast optical excitation suppresses the asymmetry entirely for $t_D < 1\text{ ps}$. This indicates an extremely non-thermal state of the system at early pump-probe delay times. The eigenfrequency of the apex mode (blue curve in Figure 4.9(c)) experiences an abrupt red-shift within 150 fs after photoexcitation, i.e. during the onset of the electronic response, and reaches its extremum within 300 fs. The

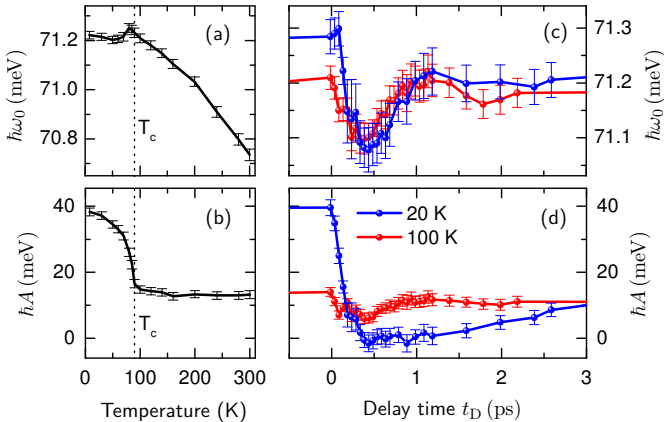


Figure 4.9: (a) Eigenfrequency and (b) asymmetry parameter of the apex mode as functions of temperature. (c) and (d) show the corresponding quantities as functions of the pump-probe delay time t_D after photoexcitation with $\Phi_i = 0.3 \text{ mJ/cm}^2$. The blue and red curves are obtained by photoexcitation of the superconducting ($T = 20 \text{ K}$) and the normal state ($T = 100 \text{ K}$), respectively. The error bars indicate 95% confidence intervals for the fitting parameters.

maximum photoinduced softening of the apex mode is comparable to the effect induced by a thermal phonon population at $T \approx 200 \text{ K}$. Thus, it can be inferred that the optical pump causes a hot phonon population of the apex mode within 150 fs. Subsequently, ω_0 relaxes to a value which is slightly reduced with respect to the equilibrium level at $T = 20 \text{ K}$. The relaxation time of 1 ps (see Figure 4.9(c)) is significantly faster than the quasi-particle recondensation, which further confirms that the phonon softening is not governed by the coupling to the Josephson plasmon. It is suggested [Pas10], that the rapid recovery of ω_0 is explained by a redistribution of the excess energy by phonon-phonon scattering into the large phase space of the entire Brillouin zone. The damping of the apex mode corresponds to a phonon lifetime of 2 ps which exceeds the observed relaxation time significantly. This finding shows that phonon-phonon scattering is faster during the hot non-equilibrium state after photoexcitation as compared to the situation in thermal equilibrium. Additional corroboration for a hot phonon population as the main cause of the red-shift of the apex mode is provided by the dynamics in the normal state (red curve in 4.9(c)) where ω_0 follows a quantitatively similar trace. The asymmetry parameter in the normal state, in contrast, shows a substantially reduced change owing to the absence of a macroscopic condensate (red curve in Figure 4.9(d)). These observations prove, that in the non-equilibrium system scattering processes between the apex mode

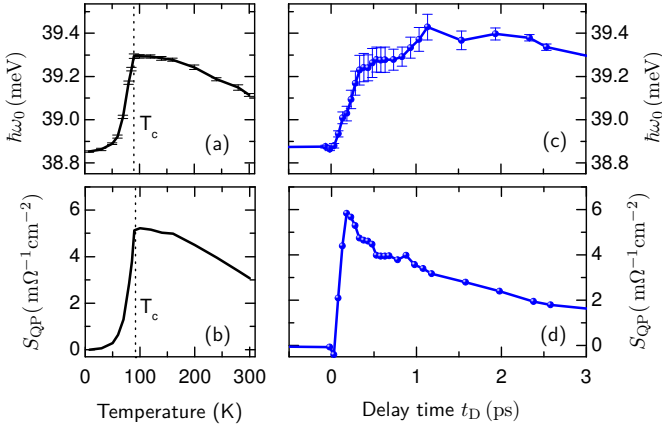


Figure 4.10: Temperature dependencies of (a) the eigenfrequency of the bond-bending mode and (b) the quasi-particle spectral weight for $\mathbf{E} \parallel c$ integrated between 45 meV and 60 meV. (c) and (d) show the corresponding quantities as functions of the pump-probe delay time t_D after photoexcitation of the superconducting state ($T = 20$ K) with $\Phi_i = 0.3$ mJ/cm². The error bars indicate 95% confidence intervals for the bond-bending mode eigenfrequency.

and the electronic system occur on the same timescale as electron-electron scattering. In the next step, it is studied whether this also holds for the bond-bending mode.

4.5.2. Excitation dynamics of the bond-bending mode

Since there exists an anomalously strong influence of the Josephson plasmon coupling on the frequency evolution of the bond-bending mode [Ber00], it is not possible to disentangle it from the anharmonic population effect as clearly as in the case of the apex mode. Nevertheless, it is instructive to compare its equilibrium properties and pump induced dynamics to the behavior of the apex mode. To this end, a Lorentzian oscillator is locally fitted on the resonance to obtain its eigenfrequency as a function of temperature and pump-probe delay time. In contrast to the apex mode, the asymmetry of the bond-bending mode is small and only weakly affected by the Josephson plasmon.

The dominant effect of coupling between the Josephson plasmon and the bond-bending phonon is given by a change of the phonon eigenfrequency ω_0 . As temperature increases towards T_c , the density of the superconducting condensate and its coupling to the bond-bending mode vanish, leading to the blue-shift of ω_0 as shown in Figure 4.10(a). Pump-induced suppression of the superconducting condensate also leads to a blue-shift of the

bond-bending mode (figure 4.10(c)). However, its dynamics does not reproduce the evolution of the quasi-particle response shown in Figure 4.10(d) although the temperature dependence of ω_0 below T_c clearly follows the quasi-particle spectral weight (compare figures 4.10(a) and (b)). The initial rapid increase of the eigenfrequency takes about 300 fs, which is two times slower than the depletion of the superconducting condensate. This stage is followed by a delayed growth of the eigenfrequency on the picosecond time scale. For $t_D > 2$ ps, the resonance frequency finally shifts back to its equilibrium value.

Above T_c , the bond-bending mode indicates a notable anharmonic red-shift (figure 4.10(a)) similar to the behavior of the apex phonon. Without Josephson coupling to the superconducting condensate, this phenomenon can be expected to persist also below T_c . The effective blue-shift of the bond-bending resonance below T_c , thus, results from the counteracting influence of Josephson coupling and lattice anharmonicities. The ultrafast dynamics depicted in Figure 4.10(c) may be understood as follows: Photoexcitation destroys the condensate and depletes phonon-plasmon coupling. The associated blue-shift of the phonon frequency is therefore expected to occur within 150 fs after the pump pulse. The delayed component of the onset dynamics of the eigenfrequency may be associated with the lattice anharmonicity induced by a hot phonon population. As the occupation number of the bond-bending mode decays, the red-shift relaxes and leads to a further increase of the phonon eigenfrequency on a picosecond time scale. Since the Josephson plasmon remains suppressed for a few picoseconds, the eigenfrequency may exceed the values observed in thermal equilibrium during this period, since the anomalous red-shift due to the Josephson coupling is suppressed while the phonon occupation number corresponds to a temperature below T_c . Together with the recovery of the Josephson resonance, the eigenfrequency ultimately starts to return to its equilibrium frequency.

Importantly, the relatively slow initial onset of the bond-bending mode anomaly within 300 fs indicates a different timescale of the electron-phonon interaction for this mode as compared to the apex mode.

4.6. Résumé: Electron-electron and electron-phonon scattering

The different timescales of the electron-phonon interaction observed for the two phonon modes under study permits one to exclude a scenario in which the phonon anomalies are caused by a photoinduced bond softening as observed, for example, in bismuth [Fri07]. In this case, the onset dynamics for all phonon modes would be the same since it is governed by the density of the photoexcited electrons. Such a behavior is in contrast to the experimental observation of the phonon dynamics in $YBa_2Cu_3O_{6.93}$.

Furthermore, the results clearly indicate that a major portion of the absorbed pump energy is transferred to the phonon subsystem within 150 fs after photoexcitation of the electronic system. Further evidence supporting this argumentation comes from an energy balance of the pump-induced transition into the normal state. The energy density of $\simeq 10 \text{ J/cm}^3$ required to suppress the superconducting phase optically (see section 4.3) is much higher than the thermodynamically determined condensation energy of 1.2 J/cm^3 [Lor93]. Following the lines of Kusar *et al.* [Kus08], only the phonon subsystem possesses sufficient heat capacity to dissipate the high excess energy of the pump pulse.

It is worth comparing this situation with the two- or three-temperature models [All87, Per07]. These theories have been established assuming the electron-phonon scattering rate to be negligible as compared to electron-electron interaction. In conclusion, this temporal hierarchy of scattering processes put forward in the context of normal metals [All87] or high-temperature superconductors such as $\text{Bi}_2\text{Sr}_2\text{CaCu}_2\text{O}_{8+\delta}$ [Per07] does not hold in case of $\text{YBa}_2\text{Cu}_3\text{O}_{7-\delta}$ where a hot phonon population and pair breaking occur on comparable time scales. In this work, it is found that for the case of $\text{YBa}_2\text{Cu}_3\text{O}_{7-\delta}$ electron-electron scattering and electron-phonon scattering processes occur on the same timescale.

Chapter 5

Non-adiabatic switching of ultrastrong light-matter coupling

The two previous chapters reported new insights into the microscopic mechanisms behind the formation of macroscopic states in bulk solids resulting from strongly correlated low-energy excitations defined by nature. In this chapter, an artificial type of interaction between tailor-cut elementary excitations is studied: Ultra-strong coupling between a custom designed electronic resonance and a tailored optical eigenmode of a microcavity. The incentive to engineer the coupling strength between light and matter resonances is mainly based on the prospect to observe novel quantum-electrodynamical phenomena in these systems. Such effects are expected to occur when the light-matter interaction strength is modulated on a sub-cycle timescale. In this work, it is demonstrated that the matter part of an ultrastrongly coupled system can be activated non-adiabatically by a NIR control pulse while a femtosecond multi-THz pulse monitors signatures of the interaction strength. The development of this technology aims to ultimately provide a route towards experimental observation of a phenomenon reminiscent of the dynamical Casimir effect: The emission of photons out of the quantum vacuum [Ciu05, Lib07].

The first sections of this chapter introduce the physics of ultrastrong light-matter interaction and the technology of the optically switchable ultrastrong light-matter coupling device. Next, it is demonstrated via femtosecond multi-THz spectroscopy of the device's photonic band structure that optical activation of an electronic resonance via a NIR pump pulse enables optical control of the light-matter interaction strength. Finally, it will be shown that optical excitation may be employed to switch ultrastrong light-matter interaction non-adiabatically. This part of the work has been published in *Physical Review B: Rapid Commun.* [Por12].

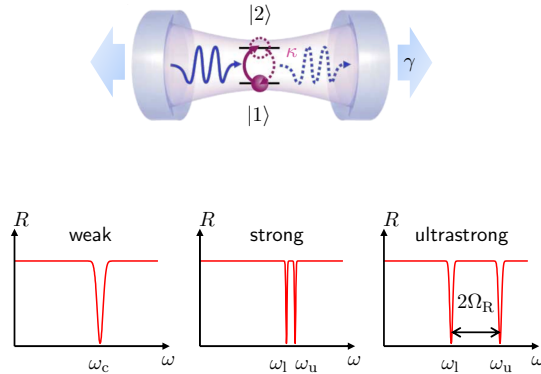


Figure 5.1: Regimes of light-matter interaction between a cavity mode (loss rate γ , eigenfrequency ω_c) and a cavity-embedded radiative matter transition (dephasing rate κ , eigenfrequency $\omega_{12} = \omega_c$, symbolized by a two-level system): Weak coupling (vacuum Rabi frequency $\Omega_R < \gamma, \kappa$), strong coupling ($\Omega_R > \gamma, \kappa$) and ultrastrong coupling ($\Omega_R > \gamma, \kappa$ & $\Omega_R \approx \omega_c$). The corresponding reflectivity spectra feature a single minimum (the bare cavity resonance at ω_c), two narrow-spaced polariton features (lower and upper polariton branches at ω_l and ω_u which are spaced by $2\Omega_R$) and two widely spaced polariton resonances, respectively. Figure adapted from [Gün09].

5.1. Regimes of light-matter coupling

One of the key challenges of modern quantum optics is to control the interaction of light with electronic excitations. A powerful technological approach to artificially enhance the strength of light-matter interaction is to couple an optical mode of a microcavity to a cavity-embedded matter resonance. Intuitively, the strength of light-matter interaction is quantified by the vacuum Rabi frequency Ω_R , the rate at which a virtual cavity photon is absorbed and spontaneously reemitted by the quantized emitter.

Three regimes of light-matter coupling are distinguished (compare Figure 5.1): (i) If the loss rate of the cavity γ and the dephasing rate of the radiative transition κ (reflected by the linewidths of the cavity and the matter resonance, respectively) exceed Ω_R , the system is in the *weak* coupling regime. In this case, the discrete density of photonic states modifies the lifetime of the matter excitation (Purcell effect [Pur46]). (ii) The system enters the regime of *strong* coupling, when Ω_R exceeds γ and κ . The eigenstates of the coupled system are then given by hybrid light-matter mixed modes, called cavity polaritons. A first demonstration of these quasi-particle excitations was achieved using atoms in metallic cavities [Rem87]. A few years later, this regime was reached via coupling of

an excitonic matter transition to a semiconductor microcavity [Wei92]. The distinctive dispersion of cavity polaritons [Kli07] described by two anti-crossing polariton-branches, which are separated by the characteristic energy of $2\hbar\Omega_R$, has facilitated fascinating solid-state quantum optics, including electrically driven inversionless lasing [Bha14] or Bose condensation of exciton-polaritons [Den02, Kas06, Mén14]. (iii) One of the most intriguing aspects is the limit of *ultrastrong* coupling, where Ω_R becomes comparable with the transition frequency ω_{12} of the matter excitation itself. This extreme case has been reached by hybridizing discrete transitions between electronic subbands in semiconductor quantum wells with the mid-infrared photonic mode of a planar waveguide structure [Din03, Dup07, Ana09, Gün09]. By exploiting the strong field enhancement in plasmonic metal structures, extremely high energy splitting of the two polariton branches by as much as $2\Omega_R = 0.5 \times \omega_{12}$ has been achieved [Tod09, Tod10, Zan10, Gei10]. Alternative approaches to reach the ultrastrong coupling regime involving superconducting circuits [Nie10, FD10] or large molecules [Sch11] have followed.

An appropriate quantum-mechanical description of ultrastrong light-matter coupling has to go beyond the rotating wave approximation. Such an approach includes the antiresonant terms of the light-matter coupling Hamiltonian and provides an adequate description of the polariton vacuum ground state $|G\rangle$ of the ultrastrongly coupled system. With this, it can be shown that $|G\rangle$, a two-mode squeezed vacuum state, is distinctly different from the vacuum ground state $|0\rangle$ of the uncoupled system [Ciu05]. The defining property of a vacuum ground state is that no eigenmode of the system is in an excited state. For the uncoupled system, this means that neither a photon (created by a^\dagger) nor a matter excitation (created by b^\dagger) is present, i.e.

$$\langle 0|a^\dagger a|0\rangle = 0 \quad \text{and} \quad \langle 0|b^\dagger b|0\rangle = 0. \quad (5.1)$$

In the polariton ground state, no polariton excitation (created by p^\dagger) exists:

$$\langle G|p^\dagger p|G\rangle = 0. \quad (5.2)$$

The expectation of non-classical effects mainly relies on the fact [Ciu05] that the polariton ground state of the ultrastrongly coupled system $|G\rangle$ is occupied with virtual cavity photons and that the ground state of the bare cavity mode $|0\rangle$ is populated with virtual polaritons:

$$\langle G|a^\dagger a|G\rangle \neq 0 \quad (5.3)$$

$$\langle 0|p^\dagger p|0\rangle \neq 0 \quad (5.4)$$

These excitations are called virtual since they do not correspond to an excitation of an eigenmode of the respective system and can only exist for a timespan allowed by the

energy-time uncertainty. They are unobservable since their detection would violate energy conservation. However, if the system is transformed non-adiabatically (i.e. on a timescale shorter than a single oscillation cycle of the involved modes) from one ground state to the other, the virtual excitations are predicted to suddenly become a real excitation of the system and should escape as entangled photons to the external space [Ciu05]. This process is comparable to the dynamical Casimir effect [Yab89, Ciu05, Lib07] and has been studied theoretically in detail for the case of a periodic modulation of Ω_R in an intersubband-polariton system [Ciu05, Lib07]. Recent publications report indications of quantum vacuum radiation emerging at an artificial event horizon [Bel10] and during rapid modulation of superconducting circuits [Wil11]. However, these remarkable findings remain controversially discussed and evidence of such non-classical radiation in the optical regime is still lacking.

Non-adiabatic dynamics of mid-infrared intersubband-polaritons entering the ultrastrong coupling regime has become accessible with field-resolved sub-cycle multi-THz spectroscopy in a seminal work by Günter *et al.* [Gün09]. This experiment demonstrated sub-cycle activation of ultrastrong light-matter coupling between a 2D waveguide mode and an embedded optically switchable intersubband [Yu10] resonance, for the first time. However, sub-cycle control of the light-matter interaction with NIR control pulses required elaborate tilting of the NIR pulse fronts. Furthermore, a complex prism-coupling geometry enabled only limited access on the relevant polariton modes. Since Casimir photons are expected to appear as excitations of the polariton modes, it is essential to obtain full femtosecond access to these modes in order to probe their population after the non-adiabatic switching event.

In the next section, a novel light-matter coupling device is introduced that enables to probe a coherent population of the relevant polaritonic bands by means of multi-THz electro-optic sampling in straightforward transmission geometry. This approach constitutes a further step towards the observation of the dynamical Casimir effect in intersubband-polariton systems.

5.2. A device for optical control of light-matter coupling

5.2.1. Design of the switchable matter excitation and the photonic mode

Intersubband transitions in quantum wells [Ros02a, Yu10] are naturally suited for engineering the enhancement of light-matter interaction: Due to the spatial extent of subband wavefunctions of typically 10 nm given by the dimensions of the quantum wells, the intersubband dipole moment is much larger than the dipole moment of interband transitions,

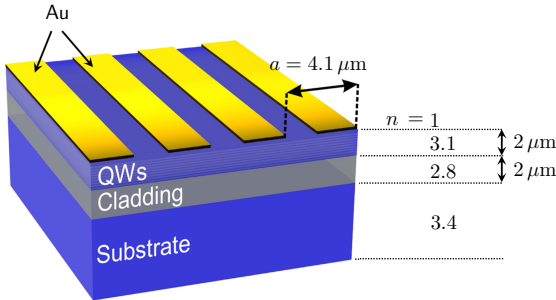


Figure 5.2: Design of the switchable ultrastrong light-matter coupling device. The refractive index contrast between vacuum, AlGaAs/GaAs heterostructure (quantum wells (QWs) and cladding layer) and GaAs substrate forms a planar refractive index waveguide. Together with a lateral gold grating, the structure constitutes a photonic crystal. Its optical eigenmodes with polarization components in the growth direction couple to an optically switchable intersubband transition located inside the quantum well region.

which is determined by the atomic dipoles of the underlying Bloch functions. To custom tailor also the light field for maximized light-matter interaction, photonic crystals ([Joa08]) provide an ideal solution. Furthermore, the dispersion of their optical eigenmodes can be precisely controlled to yield a design-cut photonic band structure. Zanotto *et al.* [Zan10] employed this concept to implement ultrastrong light-matter interaction between an intersubband transition and the custom tailored eigenmode of a one-dimensional photonic crystal. The photonic mode was engineered such that the polaritonic modes could be mapped out via equilibrium spectroscopy in simple reflection geometry.

This work combines the photonic crystal introduced by Zanotto *et al.* with a switchable intersubband transition [Gün09]. This way, full access to the polariton modes is obtained while light-matter interaction can be activated non-adiabatically with a NIR control pulse. The next paragraph summarizes the structure of the novel design. The specific choices of the structural and compositional parameters are explained in the subsequent paragraphs.

Figure 5.2 illustrates the switchable light-matter coupling device. The fabrication of the structure¹ is separated into two steps: First, a $4\text{ }\mu\text{m}$ thick AlGaAs/GaAs heterostructure is grown by molecular beam epitaxy onto a $350\text{ }\mu\text{m}$ thick GaAs substrate. The heterostructure is comprised of a $\text{Al}_{0.95}\text{Ga}_{0.05}\text{As}$ cladding layer with a thickness of $2\text{ }\mu\text{m}$ and

¹Samples were fabricated by S. Zanotto and G. Biasol (Laboratorio TASC, Trieste, Italy) as well as R. Degl'Innocenti, and L. Sorba (NEST, Istituto Nanoscience, Pisa, Italy).

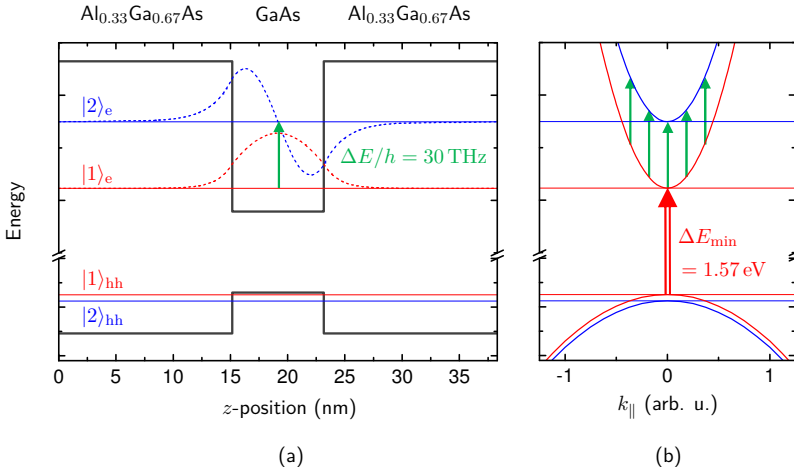


Figure 5.3: (a) Design of the multiple quantum well heterostructure. Upper and lower gray solid lines show the confinement potential given by the conduction and valence band edges as a function of the position z along the growth direction. Subband energy levels for zero in-plane electronic wave vector k_{\parallel} are indicated by horizontal lines. Dashed lines indicate the envelope wavefunctions of the electronic subband states². (b) Dispersion of the subbands. NIR optical pumping with a minimum photon energy of ΔE_{min} (red arrow) excites carriers from the uppermost heavy hole subband $|1\rangle_{\text{hh}}$ to the lowest electronic subband $|1\rangle_{\text{e}}$, activating the electronic intersubband transition $|1\rangle_{\text{e}} \rightarrow |2\rangle_{\text{e}}$ with a k_{\parallel} independent transition energy of $h \times 30 \text{ THz}$ (indicated by green arrows in (a) and (b)).

a quantum well structure on top consisting of 50 repetitions of 8.3 nm thick GaAs wells separated by 30 nm thick $\text{Al}_{0.33}\text{Ga}_{0.67}\text{As}$ barriers. In a second step, a one-dimensional gold grating (thickness: 40 nm, fill factor: 0.6) with period $a = 4.1 \mu\text{m}$ is fabricated on top of the structure via thermal evaporation of the gold layer and electron-beam lithography. This architecture defines the intersubband resonance and the surface plasmon photonic mode while enabling ultrastrong coupling between both.

Figure 5.3 illustrates the design of the quantum well heterostructure. The width of 8.3 nm of each GaAs quantum well is chosen such that the energetic distance between the lowest electronic conduction subbands amounts to $h\nu_{\text{ISB}} = 125 \text{ meV}$ corresponding to a photon frequency of $\nu_{\text{ISB}} = 30 \text{ THz}$. The width of 30 nm of the $\text{Al}_{0.33}\text{Ga}_{0.67}\text{As}$ barriers confines

²The spacing of the energy levels and the wavefunctions are calculated with the nextnano³ tool.

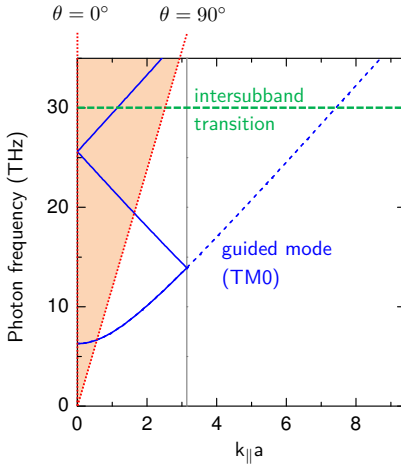


Figure 5.4: Schematic photonic band structure of the device for inactive light-matter interaction. The eigenfrequency of the planar transverse magnetic TM0 refractive index guided mode as a function of the in-plane wavevector k_{\parallel} is sketched as blue dashed curve. The Brillouin zone boundary at $k_{\parallel}a = \pi$ (solid vertical line) induced by the gold grating with period a folds the guided mode into the first Brillouin zone, yielding the photonic band structure of the device (blue curves). The dispersion of the intersubband transition (not activated) is indicated by a dashed green line. The red dotted lines show the dispersion of external vacuum plane waves for two extreme values of the angle of incidence θ . The orange shaded region can be probed experimentally.

the electronic envelope wavefunctions to a single quantum well, ensuring discrete subband states. Optical excitation of the undoped quantum well heterostructure with NIR pulses centered around a photon energy of 1.55 eV excites electrons from the uppermost heavy hole subband $|1\rangle_{hh}$ to the lowest electronic subband $|1\rangle_e$ (red arrow in Figure 5.3). Interband transitions are allowed only between hole and electron subbands with the same parity. Once the lowest energetic subband level is populated, the intersubband transition $|1\rangle_e \rightarrow |2\rangle_e$ (green arrows in Figure 5.3 (a) and (b)) is active. Its overall dipole moment is oriented in growth direction and scales with the density of photogenerated carriers ρ_{1e} in the $|1\rangle_e$ subband. To efficiently populate the $|1\rangle_e$ subband states with nonzero in-plane wavevector k_{\parallel} (compare Figure 5.3 (b)), the bandwidth of the NIR pump pulse needs to be sufficiently high.

For ultrastrong light-matter interaction, a confined optical mode with maximized coupling to the intersubband dipole moment is shaped inside the quantum well region. The first element for optical mode confinement is the planar refractive index waveguide formed by

the epitaxially grown layers and the substrate. The cladding layer serves to enhance the refractive index contrast. Transverse magnetic (TM) guided modes feature an electric field in growth direction and thus couple to the intersubband dipole moment. The second element for optical mode confinement is the one-dimensional gold grating on top of the planar waveguide. The purpose of this photonic crystal structure is two-fold. First, it enhances the field confinement itself (for details see section 5.2.2). Second, it tailors the dispersion of the guided modes in a way that they can be mapped out via straightforward transmission spectroscopy, as described in the following. Transmission or reflection spectroscopy can probe only photonic modes that share photon frequency and in-plane wavevector k_{\parallel} with external plane waves. To illustrate the situation, Figure 5.4 compares the photon frequency dispersion of the lowest energy planar TM mode (blue dashed line) with the dispersion of external plane waves given by $k_{\parallel} = 2\pi\nu \times \sin(\theta)/c$, where θ is the angle of incidence. Red dotted lines show the plane wave dispersion for normal ($\theta = 0^\circ$) and streaking ($\theta = 90^\circ$) incidence. In the case of streaking incidence, the dispersion indicates the maximum values of k_{\parallel} achievable with external plane waves. Thus, optical eigenmodes of the system with higher in-plane wavevector are totally confined within the structure and, in turn, cannot be probed via an external electromagnetic radiation (except via a disruption of the waveguide, e.g. by a prism-coupling geometry). In contrast, any eigenmode in the accessible “leaky” region of the photonic band structure (highlighted by an orange shading) can be fully accessed by appropriate tuning of the in-plane wavevector of the external plane waves by variation of θ . The one dimensional photonic crystal on top of the structure induces a Brillouin zone boundary for the planar waveguide mode and folds its dispersion back into the first Brillouin zone. The period of the grating is chosen such that the polariton forming of the intersubband transition (green dashed line in Figure 5.4) and the back folded mode (blue line in Figure 5.4) lies inside the leaky region that couples to the external radiation field.

In the next sections it is shown that the polaritonic dispersion of the ultrastrongly coupled system can be mapped out with multi-THz time-domain spectroscopy on a sub-cycle timescale while light-matter interaction is activated non-adiabatically.

5.2.2. A switchable photonic bandstructure

Figure 5.5 shows typical multi-THz field transmission spectra of the device as a function of k_{\parallel} captured by few-cycle THz-probe transients with a duration of 100 fs (generated and electro-optically sampled using 50 μm thick GaSe crystals). In the field transmission map of the unpumped device (Figure 5.5(a)), two photonic bands can be identified. Both modes are degenerate at $\nu = 26.6$ THz, in the center of the Brillouin zone, but split with

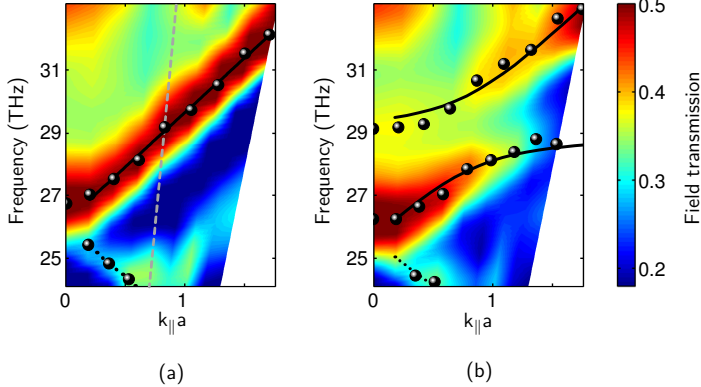


Figure 5.5: Experimental field-transmission spectra of the photonic crystal structure ($a = 4.1 \mu\text{m}$) as a function of k_{\parallel} for $0 \leq \theta \leq 40^\circ$. Results are measured (a) in equilibrium and (b) $t_D = 1 \text{ ns}$ after photo-activation of the intersubband transition with $\Phi = 1.6 \text{ mJ/cm}^2$. Black spheres: local transmission peaks indicating the eigenmodes. Solid black lines: numerically adapted linear dispersion in (a) and polariton dispersion in (b). Dotted black line in (a) and (b): dispersion of the lower photonic band. Dashed gray line in (a): Cross section indicating the spectrum measured at $\theta = 20^\circ$ studied in Figure 5.6.

increasing k_{\parallel} . Qualitatively these states arise from the planar waveguide mode which is Bragg scattered by the reciprocal lattice vectors π/a and $-\pi/a$, respectively (compare Figure 5.4). Photoinjecting electrons into the lowest electronic subband $|1\rangle_e$ of each quantum well with a NIR pump fluence of $\Phi = 1.6 \text{ mJ/cm}^2$ induces a strong modification of the band dispersion, as directly mapped out in Figure 5.5(b) for $t_D = 1 \text{ ns}$. The interaction between the intersubband resonance and the upper photon band causes the formation of two polariton branches (black spheres and black solid lines in Figure 5.5(b)). The minimum separation of the polariton branches occurring at the anticrossing point may be directly identified with the vacuum Rabi splitting $2\Omega_R/2\pi$. Experimentally, the minimum energy splitting of the polariton modes is observed for $\theta = 20^\circ$ and amounts to $h \times 3 \text{ THz}$. Furthermore, both polariton bands are strongly flattened as compared to the unperturbed photon dispersion.

To gain further insight into the microscopic nature of the eigenmodes, the spectral shape of a typical transmission resonance is compared with the results of a FDFD calculation³

³The calculations are based on the total field/scattered field formalism [Rum06]. The simulations employ parts of a tutorial FDFD Matlab code provided by R. Rumpf, EM Lab, University of Texas.

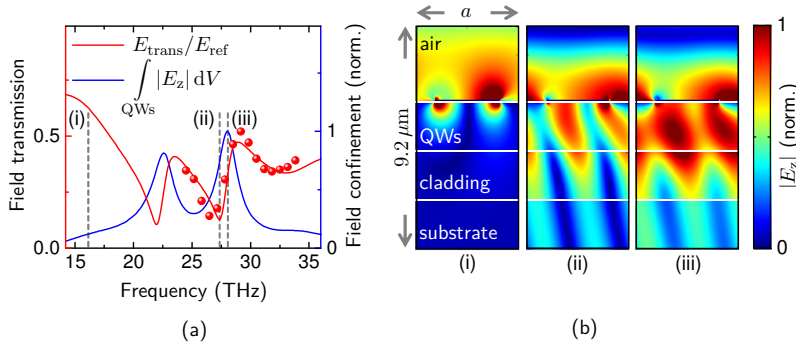


Figure 5.6: (a) Field transmission of the plasmonic crystal structure ($a = 4.1 \mu\text{m}$) as a function of photon frequency measured (red dots) and calculated via a FDFD simulation (red line) for an angle of incidence of $\theta = 20^\circ$. The blue curve shows the corresponding calculated electrical field in growth direction integrated inside the quantum wells as a function of frequency. (b) Analysis of the electric field enhancement inside the structure. The color maps show the electrical field in growth direction that couples to the intersubband transition inside the quantum well (QW) region. The situation is shown for three characteristic photon frequencies (indicated by vertical dashed lines in (a)): (i) Off-resonance and at the upper photonic band at its transmission minimum (ii) and its maximum field enhancement (iii).

[Rum06]. Figure 5.6 (a) shows the experimental transmission curve of the unpumped structure measured at $\theta = 20^\circ$ (red dots) and the corresponding simulated spectrum (red solid curve). The simulation quantitatively recovers the Fano-like line shape [Zan12] and, additionally, reveals the electrical field enhancement inside the quantum well region. The blue solid curve shows the electric field in growth direction integrated inside the quantum well region. The peaks at 22.5 THz and 27.3 THz correspond to the field confinement caused by the lower and the upper photonic band, respectively. Furthermore, the FDFD simulation enables to link the transmission spectra with the underlying electromagnetic modes. Figure 5.6 (b) illustrates the spatial profile of the electric field $|E_z|$, oriented along the growth direction for three characteristic frequencies. Off resonance (i) at $\nu = 16 \text{ THz}$, only a plasmonic field enhancement occurs at the edges of the gold stripes. The transmission minimum at $\nu = 27 \text{ THz}$ (ii) originates from the Fano-like resonance of the upper photon band. The field enhancement at this photon frequency is still mostly of plasmonic nature. Maximum field confinement occurs at $\nu = 27.3 \text{ THz}$ with the photonic mode strongly localized within the quantum well layers. Thus, the eigenmodes of the photonic

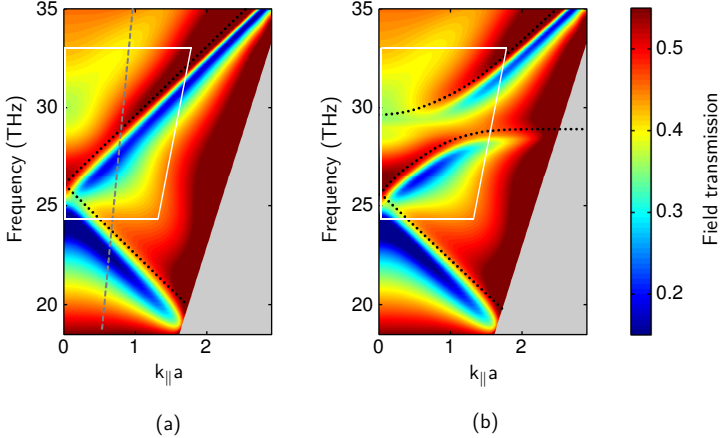
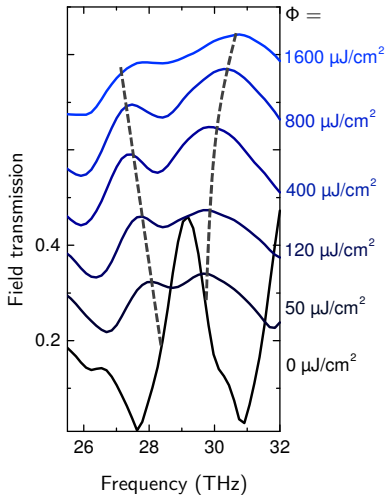


Figure 5.7: Calculated field-transmission spectra of the (a) unpumped and (b) pumped sample for $0 \leq \theta \leq 89.9^\circ$. In (b), the intersubband transition is active with a center frequency of 29 THz and an assumed electron density in the lowest electronic subband of $\rho_{1e} = 2 \times 10^{11} \text{ cm}^{-2}$. Black dotted curves indicate the eigenmodes. Dashed gray lines in (a): cross section displayed in Figure 5.6(a). White tetragons: experimentally covered area shown in Figure 5.5.

crystal are the result of the concerted action of surface plasmons and planar waveguiding by total internal reflection due to the refractive index contrast.

Repeating the simulation of the transmission spectrum for various angles of incidence, the full photonic band structure is recovered as seen in Figure 5.7 (a). In order to model the band structure of the strongly coupled system (Figure 5.7 (b)), the intersubband dipole moment is treated classically via an effective refractive index [Din03]. With a population of the lowest electronic subband of $\rho_{1e} = 2 \times 10^{11} \text{ cm}^{-2}$, good agreement with the experimental transmission map of Figure 5.5 (b) is achieved. The dispersion of all bands, the strength of light-matter coupling and the absolute value of field transmission are adequately reproduced. Furthermore, the FDFD analysis suggests that the surface plasmonic contribution increases Ω_R by 50% as compared to a structure supporting purely photonic propagation alone.

It may be noted, that under the action of extremely strong light-matter coupling, the slope of the polaritonic bands in the light matter coupling device is profoundly reduced as compared to the dispersion of the bare photonic mode (compare Figures 5.5 (a) and (b)). This effect gives rise to a slow-down of the group velocity $d\omega/dk_{\parallel}$ of the guided modes. For a quantitative discussion of this effect, see appendix E.

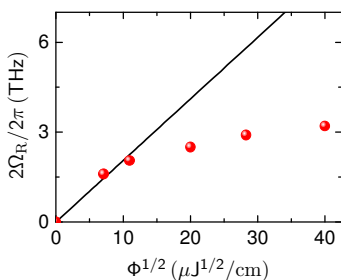
**Figure 5.8:**

Transmission spectra of the photonic crystal structure (substrate removed) showing the polariton formation at the anticrossing point ($\theta = 13^\circ$) measured at $t_D = 1\text{ ns}$ for various incident pump fluences Φ . To ensure that additional membrane guided modes are far above the measurement window, the intersubband transition is now coupled to the lower photon band by setting $a = 3.6\text{ }\mu\text{m}$. All curves are separated by a linearly increasing offset. Dashed vertical lines indicate the transmission maxima corresponding to the two polariton branches.

5.3. Optical control of the light-matter coupling strength

In preparation for time resolved experiments, the GaAs substrate of the heterostructure is locally removed by chemical etching with a citric acid/hydrogen peroxide mixture to obtain a free standing membrane with minimal dispersion for ultrafast laser pulses. Pump and probe beams are directed onto the rear side of the sample to inject a homogeneous distribution of carriers and prevent lateral diffusion effects from affecting the intrinsic dynamics. The increased refractive index contrast between the cladding layer and air gives rise to additional photonic bands of higher energy in the membrane. To ensure that the new resonances are far above the measurement window, the intersubband transition is now coupled to the original lower photonic band by setting the period of the gold grating to $a = 3.6\text{ }\mu\text{m}$.

In a first step towards femtosecond control of ultrastrong coupling it is investigated how the strength of optically induced light-matter interaction scales with the intensity of NIR photoexcitation. To this end, transmission spectra through the sample are recorded for various values of Φ at a fixed delay time $t_D = 1\text{ ns}$ with $\theta = 13^\circ$ set to the anticrossing point (Figure 5.8). In the unpumped case, a single resonance with its field transmission maximum at 29 THz and a narrow width of 1.4 THz (FWHM) is observed. The width

**Figure 5.9:**

Red dots: Vacuum Rabi splitting $2\Omega_R/2\pi$ in the structure (substrate removed, $a = 3.6 \mu\text{m}$) as a function of the square root of the incident pump fluence $\Phi^{1/2}$ measured $t_D = 1 \text{ ns}$ after photoexcitation. Solid black line: Functional dependency expected for planar waveguides without saturation effects.

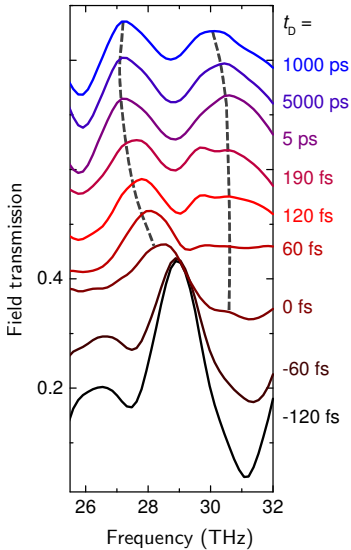
indicates a quality factor of $Q = 20$ of the uncoupled photonic cavity. With increasing pump fluence, the single peak splits into two polariton branches of comparable strength. The splitting of the polariton branches gradually increases with Φ . Since the spectra are acquired at the anticrossing point, the splitting is a direct measure of $2\Omega_R/2\pi$. As quantitatively studied in Figure 5.9, the vacuum Rabi splitting (red dots) scales with the square root of the pump fluence for $\Phi < 120 \mu\text{J}/\text{cm}^2$, analogously to the situation in planar waveguides [Ciu05, Gün09]. Yet Ω_R starts to saturate at $\Phi \approx 400 \mu\text{J}/\text{cm}^2$. A comparison with FDFD simulations suggests that a photogenerated carrier density of $\rho_{1e} = 3 \times 10^{11} \text{ cm}^{-2}$ is present in this situation.

The results presented so far demonstrate full spatial control of the photonic eigenmodes of the light-matter coupled device. In addition, all optical control of the light-matter coupling strength between the custom tailored photonic mode and the intersubband excitation is realized. In the next section, it is shown that this control can be extended towards the temporal dimension.

5.4. Nonadiabatic switching of a photonic bandstructure

Nonadiabatic control of ultrastrong light-matter interaction requires the duration of the control pulse to be distinctly shorter than the oscillation period of the coupled resonances. The NIR pulses derived from the Ti:Sapphire amplifier system with a duration of 12 fs readily fulfill this condition. In order to explore how rapidly the hybridization of the photonic band structure with the intersubband transition proceeds, the pump-probe delay time t_D is varied between -120 fs and 1000 ps (see Figure 5.10). The pump fluence is kept constant at $\Phi = 1.6 \text{ mJ}/\text{cm}^2$.

For negative delay times $t_D \leq -60 \text{ fs}$, the transmission spectra are dominated by a single eigenmode at $\nu = 29 \text{ THz}$, characteristic of the unpumped state. When the the pump

**Figure 5.10:**

Field-transmission spectra through the structure ($a = 3.6 \mu\text{m}$, substrate removed) showing the polariton formation at the anticrossing point ($\theta = 13^\circ$) for selected delay times t_D with $\Phi = 1.6 \text{ mJ/cm}^2$. A maximum splitting of 3.4 THz is reached at $\tau = 5 \text{ ps}$. All spectra are separated by a linearly increasing offset. Dashed vertical lines indicate the transmission maxima originating from the two polariton branches.

and probe pulses coincide at $t_D = 0 \text{ fs}$, an abrupt qualitative change of the transmission spectrum manifests itself. Instead of the bare eigenmode, two resonances emerge: a strong peak centered at $\omega_L/2\pi = 28.2 \text{ THz}$ and a weaker one at $\omega_U/2\pi = 30.5 \text{ THz}$, corresponding to the lower and upper polariton branch, respectively. Intriguingly, the upper branch exhibits a lower amplitude than the lower branch, it also remains spectrally much broader during the initial time window $0 \leq t_D \leq 340 \text{ fs}$. The observed ultrafast build-up dynamics of the polariton bands stands in stark contrast to an adiabatic increase of light-matter interaction, as observed for a gradual increase of ρ_{1e} (compare Figure 5.8). At $t_D = 340 \text{ fs}$, a maximum splitting of $2\Omega_R/2\pi = 3.4 \text{ THz}$ is reached. This is as much as 12% of ν_{ISB} exceeding even values demonstrated with static doping [Zan10]. At this point, both polariton branches are comparable in intensity and width. Between $t_D = 5 \text{ ps}$ and 1 ns , the vacuum Rabi frequency reduces slightly by 10% due to interband carrier recombination.

The surprising and consistently reproducible asymmetric buildup of the polaritons stands in contrast to the dynamics seen in planar waveguides [Gün09]. This qualitative discrepancy clearly indicates that the peculiar band structure of the photonic crystal sets a characteristic switch-on time for the formation of ultrastrong light-matter coupling. Due to energy-time uncertainty, abrupt switching events have to involve a broad spectrum of

eigenmodes. Contrary to planar waveguides, this spectrum is highly structured in the case of a photonic crystal. The simultaneous coherent interaction of intersubband transitions with higher photonic bands may lead to interference effects during the activation of ultrastrong coupling. It may be tentatively suggested [Por12] that nonadiabatic mixing of the upper polariton branch with the next higher photonic band plays a dominant role. A quantitative model of this fascinating new class of ultrafast quantum phenomena calls for a universal theory treating nonadiabatic quantum electrodynamics and quantum kinetic carrier dynamics, on equal footing.

In conclusion, non-adiabatic optical activation of ultrastrong light-matter interaction between a custom tailored plasmon assisted photonic mode and an intersubband transition of quantum wells is implemented. By means of sub-cycle multi-THz spectroscopy, the relevant photon and polariton modes of the novel device are fully mapped out in straightforward transmission geometry and their non-adiabatic switching dynamics is recorded on a femtosecond timescale. The novel light-matter coupling device presented in this work enhances the design introduced by Günter *et al.* [Gün09] by enabling full and simplified access to the polaritonic modes. Since Casimir photons are expected to emerge as excitations of the polaritonic modes upon non-adiabatic activation of ultrastrong light-matter interaction, the enhanced access to the polariton modes should help facilitate the detection of Casimir photons in future experiments based on shot-noise reduced ultrasensitive electro-optic sampling.

Chapter 6

Summary and outlook

The objective of this thesis is to elucidate the ultrafast dynamics of coupled low-energy excitations in both strongly correlated materials and artificially engineered quantum structures. With the aid of NIR pump/multi-THz probe spectroscopy and a series of technological innovations such as a novel collinear four-pass Ti:Sapphire amplifier and shot-noise reduced electro-optic sampling [Por14b], fundamentally new insights into the many-body physics of two representative strongly correlated materials are obtained:

Two coupled order parameters associated with the charge density wave in the transition-metal dichalcogenide $1T\text{-TiSe}_2$ are transiently separated on a femtosecond scale, for the first time [Por14a]. Following intense photoexcitation with a 12-fs near-infrared laser pulse, a novel non-thermal phase is observed in which the structural component of the charge density wave persists without exciton-like electronic order. This proves, that excitonic order is not the sole cause for the formation of a charge density wave in this material, solving a long standing mystery. The comprehensive femtosecond study of the far- to mid-infrared spectral fingerprints of electronic and lattice order presented in this work allows for a consistent identification of the elementary microscopic mechanisms underlying the formation of a charge density wave in this material: The data provide strong evidence for the joint action of excitonic electron-hole correlations and a structural Jahn-Teller-like effect to cause the charge density wave transition. This interpretation is backed up by a quantum-mechanical mean-field model, which is extended to describe the influence of photoexcitation on the excitonic and structural degrees of freedom. The results presented in this work may also serve as a benchmark to quantitatively test and advance recent three dimensional models of the charge density wave phase transition in $1T\text{-TiSe}_2$ [Zen13]. Furthermore, the refined picture of the many-body effects in $1T\text{-TiSe}_2$ may ultimately assist the identification of the mechanism that leads to (unconventional) superconductivity in

$1T$ -TiSe₂ [Mor06, Kus09] and possibly even other strongly correlated systems. From the experimental point of view, comparable studies in superconducting Cu_xTiSe₂ could further enhance the fundamental understanding of the interplay between charge ordered and superconducting phases in strongly correlated materials [Mor06, Li07a, Kis07, Cha12]. The availability of high-quality monolayers of transition-metal dichalcogenides [Wan12] paves the way for NIR-pump/THz-probe experiments to target the many-body physics also in these systems. For example, room temperature excitons in monolayered WSe₂ [Coe87] could be investigated via the excitons' internal degrees of freedom. With the introduction of silver thiogallate as THz emitter and detector reported in this work, the relevant spectral region that is expected to host internal transitions of the room temperature excitons (expected at ~ 40 THz [He14a]) is now accessible with the experimental tools employed in this work. In general, the concept to disentangle the ultrafast dynamics of structural and electronic components of an order parameter by probing back-folded phonon branches together with a purely electronic response should be universally applicable to a broad variety of other strongly correlated materials.

Furthermore, this work presents novel insights into the microscopic interaction processes in one of the most intensely studied cuprate superconductors. This experiment represents the first resonant femtosecond observation of both electronic and phononic degrees in a high-temperature superconductor [Pas10]. By recording a photoinduced superconducting-to-normal phase transition in YBa₂Cu₃O_{6.93} by means of femtosecond multi-THz spectroscopy, a qualitatively new insight into the electron-phonon interaction in this system is obtained. The lattice absorbs a large portion of the pump pulse energy while the photoexcited charge carriers thermalize and the condensate is depleted. This observation demonstrates, that there is no temporal hierarchy of electron-electron and electron-phonon scattering processes in this material. As a consequence, the applicability of two- or three temperature models [Kab08, Per07], which associate different timescales to the fundamental electron-phonon and electron-electron scattering mechanisms, can be ruled out for this case. Future experiments may target the novel class of iron-based pnictide superconductors in analogous studies. Such experiments could verify the current thinking that electron-phonon interaction does not play a primary role in the mechanism that yields superconductivity in these systems [Ste11]. Furthermore, some pnictide superconductors feature two simultaneously present superconducting gaps [Ste11]. Femtosecond THz spectroscopy appears to be ideally suited to disentangle these gaps via their intrinsic recovery dynamics and may provide valuable clues on their microscopic origins.

The last part of the work demonstrates full spatial and non-adiabatic temporal control of low-energy light-matter interaction in the limit of ultrastrong coupling [Por12]. The regime of ultrastrong light-matter coupling is of utmost interest for fundamental quan-

tum electrodynamics since it provides a unique test bed for intriguing quantum theoretical predictions. Thereof, the non-classical generation of photons out of the quantum-vacuum described by the dynamical Casimir effect [Ciu05, Lib07], which is related to Unruh-Hawking radiation of black holes [Yab89], is the most prominent example. This work takes a further step towards the observation of Casimir photons in intersubband cavity polariton systems [Gün09, Zan10]. It introduces a novel device that enables straightforward access to the photonic modes which are expected to be populated with Casimir photons upon non-adiabatic switching of ultrastrong light-matter interaction. The device features a refined control of ultrastrong light matter coupling in all four dimensions which is obtained by combining the spatial mode confinement and well-defined band structure of a photonic crystal with an optically switchable intersubband resonance. Femtosecond multi-THz spectroscopy is employed to demonstrate access to the relevant photonic modes of the device while ultrastrong coupling is activated non-adiabatically. The observed asymmetric formation dynamics of the light-matter mixed polariton modes calls for a novel theory accounting for both quantum kinetic carrier dynamics and non-adiabatic quantum-electrodynamics. Future experiments will primarily aim for the observation of the dynamical Casimir effect in this system. Thereby, the concept of shot-noise reduced electro-optic sampling developed in this work may prove helpful [Por14b].

In this work, NIR pump/multi-THz-probe spectroscopy has enabled the study of ultrafast low-energy dynamics of fundamentally different systems – strongly correlated materials and artificially engineered quantum structures. Recent advances in THz technology pave the way for entirely new types of experiments and can be anticipated to play a similarly outstanding role in the near future. High-field THz sources [Sel08a, Sch14] have been developed with the goal to not only study the low-energy degrees of freedom but to also coherently control them via both the electric and the magnetic fields of phase-stable THz radiation. This approach has already been successfully applied for the first observation of electric field induced dynamical Bloch-oscillations in a bulk semiconductor [Sch14] and may bring the observation of novel phenomena such as THz-magnetic-field-controlled spin switching into reach [Kam11]. Field resolved access to the oscillating THz near-field of nanostructures has become accessible recently with the novel technique of ultrafast near-field multi-THz nano-spectroscopy [Eis14]. One can envision to directly monitor how wavefunctions associated with eigenstates of nanostructures evolve on a femtosecond scale [Jac12] or to observe ultrafast formation processes of ordered domains in strongly correlated materials [Qaz07], just to name a few promising perspectives.

Appendix **A**

Raw data of a NIR-pump/THz-probe experiment

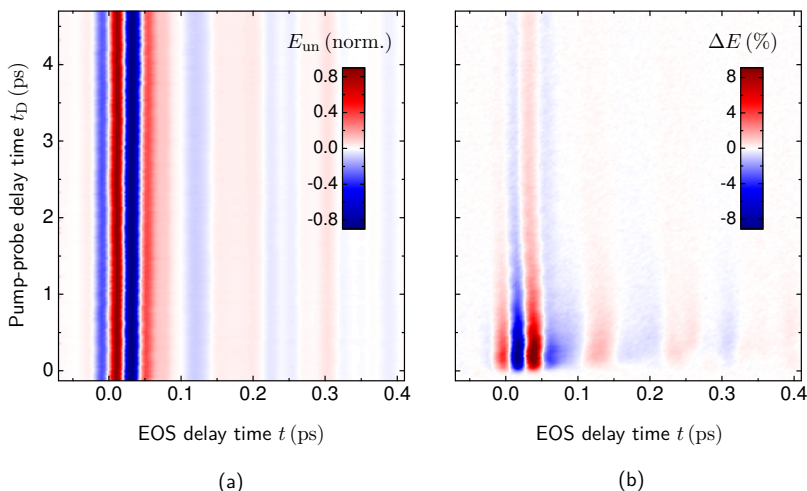


Figure A.1: Raw data of a NIR-pump/THz-probe experiment, corresponding to datasets shown in Figures 3.8, 3.9 and 3.10. (a) Electric field trace of single-cycle THz transients measured after transmission through an unexcited 80 nm thin film of 1T-TiSe₂. (b) Photoinduced change of the transmitted THz electric field. The temperature of the sample is kept at $T = 10$ K and the absorbed pump fluence is $\phi = 40 \mu\text{J}/\text{cm}^2$. This 2D dataset was acquired in less than four hours. Note the excellent long term stability of the reference transients throughout the measurement.

B

Appendix

Numerical analysis of the dielectric response of 1T-TiSe₂: Quality of the fits

As described in section section 3.3.2, the transient change in the free carrier density $\Delta n(t_D)$ and the transient free carrier scattering time $\tau(t_D)$ of 1T-TiSe₂ after photoexcitation are extracted from the time dependent energy loss function by numerical adaption of the model function given by equation (3.1). Thereby, both the real and imaginary part of $1/\varepsilon(\hbar\omega, t_D)$ are fitted simultaneously, with high confidence. Figure B.1 compares the measured (left panels) and fitted spectra (right panels) of a 2D dataset acquired with a pump fluence of $\phi = 40 \mu\text{J}/\text{cm}^2$ at $T = 10\text{ K}$ to highlight the quality of the fit curves.

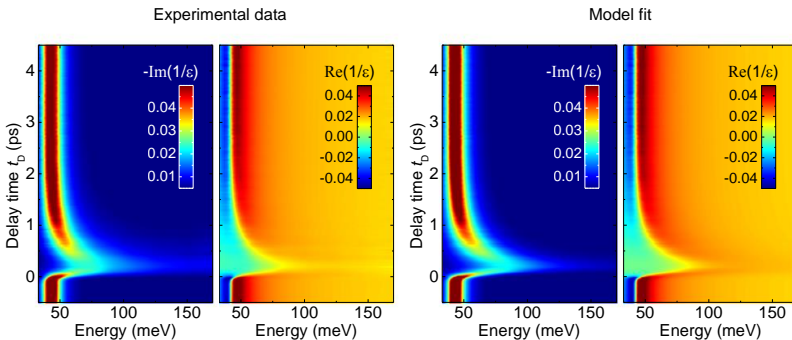


Figure B.1: Left panels: Imaginary and real part of $1/\varepsilon(\hbar\omega, t_D)$ of photoexcited 1T-TiSe₂ measured at $T = 10\text{ K}$ shown for a representatively selected pump fluence of $\phi = 40 \mu\text{J}/\text{cm}^2$. Right panels: Corresponding spectra of the numerically adapted model function (equation (3.1)) used to extract $n(t_D)$ and $\tau(t_D)$.

Extended analysis of the transient dielectric response of 1T-TiSe₂

As discussed in section 3.6, the multi-THz probe covers part of the interband transition across the CDW gap of 1T-TiSe₂. In this spectral region, coherent oscillations of the absorption coefficient are observed after NIR photoexcitation. To further corroborate the interpretation that the coherent dynamics reflects a modulation of the Jahn-Teller component of the CDW gap, the transient properties of the single-particle interband transition are studied quantitatively as far as possible. To this end, additional parameters of the model dielectric function (equation 3.1) are adapted to the measured dielectric response: The center energy E_{gap} and the damping γ_{gap} of the interband transition across the CDW gap. Even though only a small fraction of the resonance is captured, numerical adaption of four fit parameters proves possible for small pump induced changes at low pump fluence ($\phi \leq 20 \mu\text{J}/\text{cm}^2$). Since numerical fitting of $1/\varepsilon$ strongly suppresses numerical weight of the single particle transition and allows for reliable extraction n and τ , the numerical fit shown here is performed via adaption of the dielectric function ε . To further extend the numerical weight of the interband transition, the energy window for the fit is extended to 150 meV. For convergence of the fitting algorithm, it is necessary to keep the spectral weight of the interband resonance fixed, which can be considered legitimate for low Φ .

Figure C.1 shows the transient fit parameters extracted from $\varepsilon(\hbar\omega, t_{\text{D}})$ measured with $\Phi = 20 \mu\text{J}/\text{cm}^2$ at $T = 10 \text{ K}$. The transient free carrier density n (a) and free carrier scattering time τ (b) reproduce the results shown in figure 3.9. Panels (c) and (d) additionally show the transient damping γ_{gap} and center energy E_{gap} of the interband transition across the CDW gap. The pump-induced change in γ_{gap} mimics the change in n , suggesting that a broadening of the interband resonance is governed by the presence of photogenerated free carriers. The exponential decay dynamics of E_{gap} is essentially the same as observed for τ . Notably, the coherent oscillations of the absorption coefficient are entirely captured

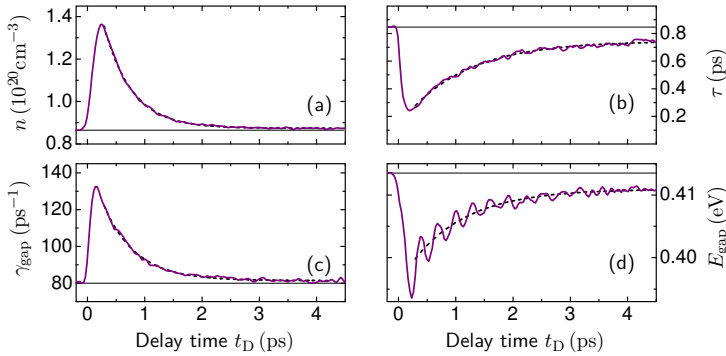


Figure C.1: Extended quantitative analysis of the transient dielectric response measured after photoexcitation with $\Phi = 20 \mu\text{J}/\text{cm}^2$ at $T = 10\text{ K}$. (a) and (b) show the Drude parameters n and τ describing the plasma response. (c) and (d) show the damping γ_{gap} and center energy E_{gap} of the interband transition across the CDW gap. Dashed lines show an exponential decay numerically adapted to the measured data.

by E_{gap} . Taken together, these observations fully corroborate the picture of combined action of excitonic and Jahn-Teller like mechanisms in the CDW formation and clearly indicate that the CDW gap is jointly formed by both contributions: On the one hand, the exponential recovery dynamics observed in both τ and E_{gap} can be associated with the recovery of the excitonic component of the CDW order. On the other hand, the oscillations superimposed to the exponential recovery of E_{gap} reflect modulations of the Jahn-Teller like energetic lowering of the Se4p bands caused by coherent oscillations of the A_{1g} amplitude mode. In fact, the modulation of E_{gap} due to Jahn-Teller effects is reproduced by the theoretical model (section 3.7).

Appendix D

The model phase diagram of 1T-TiSe₂: Constraints for ρ , τ_{in} and τ_{out}

As discussed in section 3.7, minimization of the total energy described by the mean-field model Hamiltonian (equation (3.8)) with the mean-fields ρ , τ_{in} , τ_{out} and u as free parameters yields the zero temperature model phase diagram. The parameters τ_{in} and τ_{out} are complex-valued, which, together with ρ , implies a total of five free parameters that describe the electronic degree of freedom.

To reproduce the results by van Wezel *et al.* [Wez10b], it turns out necessary to constrain ρ , τ_{in} and τ_{out} via conservation of the total particle number and translational invariance along the one-dimensional chain.

The following analysis is based on a general fermionic state describing the electronic degree of freedom of two neighboring unit cells with always two electrons present:

$$|\Psi_1\rangle = \alpha|1010\rangle + \beta|1001\rangle + \gamma|1100\rangle + \delta|0101\rangle + \epsilon|0110\rangle + \zeta|0011\rangle \quad (D.1)$$

The electron at the first position (Se orbital in unit cell i) is created with c^\dagger the second (Ti orbital in unit cell i) with d^\dagger , the third (Se orbital in unit cell $i+1$) with c_1^\dagger and the fourth (Ti orbital in unit cell $i+1$) with d_1^\dagger .

From translational invariance, the following constraints apply:

$$\langle \Psi | c^\dagger c | \Psi \rangle = \langle \Psi | c_1^\dagger c_1 | \Psi \rangle \quad (D.2)$$

$$\langle \Psi | d^\dagger d | \Psi \rangle = \langle \Psi | d_1^\dagger d_1 | \Psi \rangle \quad (D.3)$$

Following parametrization of $|\Psi\rangle$ fulfills these conditions:

$$|\Psi_2\rangle = \alpha|1010\rangle + \beta|1001\rangle + \gamma|1100\rangle + \delta|0101\rangle + \beta|0110\rangle + \gamma|0011\rangle \quad (D.4)$$

Again, from translational invariance, the phases of the coefficients can be either 0 or π . Taking into account that the state has to be normalized, three free parameters are left. The physically relevant choices of the phases are captured by the signs of the coefficients.

To obtain a parametrization that ensures normalization and is given by only three parameters, the state is described with real valued x , y and z as follows:

$$\begin{aligned}
 |\Psi\rangle = & \cos\left(\frac{x}{2}\right) \cos\left(\frac{y}{2}\right) |1010\rangle + \\
 & \frac{1}{\sqrt{2}} \left[\sin\left(\frac{x}{2}\right) \left(\cos\left(\frac{y}{2}\right) \cos(z) + \sin\left(\frac{y}{2}\right) \sin(z) \right) \right] (|1001\rangle + |0110\rangle) + \\
 & \frac{1}{\sqrt{2}} \left[\sin\left(\frac{x}{2}\right) \left(\sin\left(\frac{y}{2}\right) \cos(z) - \cos\left(\frac{y}{2}\right) \sin(z) \right) \right] (|1100\rangle + |0011\rangle) + \\
 & \cos\left(\frac{x}{2}\right) \sin\left(\frac{y}{2}\right) |0101\rangle
 \end{aligned} \tag{D.5}$$

With this parametrization, ρ , τ_{in} and τ_{out} are:

$$\begin{aligned}
 \rho &= \langle \Psi | c^\dagger c | \Psi \rangle - \langle \Psi | d^\dagger d | \Psi \rangle \\
 &= \frac{1}{4} \cos(x-y) + \frac{1}{4} \cos(x+y) + \frac{1}{2} \cos(y)
 \end{aligned} \tag{D.6}$$

$$\begin{aligned}
 \tau_{in} &= \langle \Psi | c^\dagger d | \Psi \rangle \\
 &= \frac{\sqrt{2}}{2} \cos\left(\frac{x}{2}\right) \sin\left(\frac{x}{2}\right) \cdot \\
 &\quad \left(\cos\left(\frac{y}{2}\right) + \sin\left(\frac{y}{2}\right) \right) \left(\cos\left(\frac{y}{2}\right) \cos(z) + \sin\left(\frac{y}{2}\right) \sin(z) \right)
 \end{aligned} \tag{D.7}$$

$$\begin{aligned}
 \tau_{out} &= \langle \Psi | c^\dagger d_1 | \Psi \rangle \\
 &= -\frac{\sqrt{2}}{2} \cos\left(\frac{x}{2}\right) \sin\left(\frac{x}{2}\right) \cdot \\
 &\quad \left(\cos\left(\frac{y}{2}\right) + \sin\left(\frac{y}{2}\right) \right) \left(\sin\left(\frac{y}{2}\right) \cos(z) - \cos\left(\frac{y}{2}\right) \sin(z) \right)
 \end{aligned} \tag{D.8}$$

Now, the parameters x , y and z substitute ρ , τ_{in} and τ_{out} upon minimization of the total energy. The values of the mean-field parameters ρ , τ_{in} and τ_{out} for minimum energy are then calculated with the above equations from the values of x , y and z for which the total energy is minimized.

Appendix E

Slow-down of light induced by nonadiabatic activation of ultrastrong light-matter coupling

The extremely strong light-matter coupling in the light-matter coupling device gives rise to a slow-down of the group velocity $d\omega/dk_{\parallel}$ of its guided modes. As a quantitative measure, the effective group index of refraction n_{eff} is extracted as a function of k_{\parallel} (Figure E.1) from a numerically adapted polariton dispersion curve [Hop58] on the experimental band structure (compare Figure 5.5), without resorting to a rotating wave approximation. While n_{eff} reflects the theoretical value of 3.15 in the unpumped sample, the extracted n_{eff} increases for the lower polariton branch to 41 at the highest k_{\parallel} -values covered in the experiment (vertical dashed line in Figure E.1). A coherent photon population which is initially prepared in the bare grating waveguide by the multi-THz transients is, thus, abruptly transferred into a polaritonic band decreasing its group velocity by a factor of 13.

Slow light reaching speeds down to only few tens of meters per second has been observed with a variety experimental methods [Big03, Ku04, Tur01]. Most of these techniques suffer from a limited bandwidth that hinders their practical applications. In this context, the present experimental scheme holds great potential because of its ability to slow down

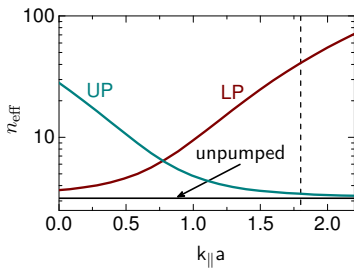


Figure E.1:

Effective refractive index n_{eff} at the upper photonic modes in the pumped and unpumped sample, as represented by the black curves in Figure 5.5. The solid curve is the theoretical $n_{\text{eff}} = 3.15$ of the light-mode propagating inside the unpumped quantum well region.

light over a bandwidth corresponding to a significant fraction of the carrier frequency. In this regards, the results presented here compare advantageously with state-of-the-art broadband generation of slow light in photonic crystal structures [Vla05, Set07]. The demonstrated control of the band structure may ultimately enable a broadband storage of light by transferring a coherent photon population from a leaky equilibrium photoplasmonic band to a non leaky polariton branch. Additionally, this scheme provides a novel possibility to investigate ultrafast switching of the slow light regime. One may even speculate that the presented concept may be employed to implement a spatially moving refractive index perturbation to generate an artificial event horizon that yields the emission of Hawking radiation, analogous to an experiment performed by Belgiorno *et al.* [Bel10].

Appendix F

Establishment of the femtosecond multi-THz laboratory

This work included the establishment of the femtosecond multi-THz laboratory at the Institute of Physics of the University of Regensburg. Parts of the NIR-pump/multi-THz-probe spectroscopy system (the cavity dumped Ti:sapphire oscillator and a series of mechanical actuators and optical components) were transferred from the University of Konstanz (Emmy Noether Group “Tera” of R. Huber at the chair of A. Leitenstorfer), where the experiments on $\text{YBa}_2\text{Cu}_3\text{O}_{6.93}$ were conducted. Building the experimental setup from scratch (compare Figure F.1 on page 112) provided the possibility to design the supporting infrastructure in the laboratory to facilitate long-term stability for high sensitivity experiments (compare Figure A.1 in appendix A). An air conditioning system stabilizes temperature and humidity in the laboratory (temperature stability: $\pm 0.1^\circ\text{C}$). Special care was taken to isolate the experimental setup from acoustic vibrations of the environment. To this end, the setup is placed on a vibration damped standard optical table. Acoustic noise induced by supporting hardware such as chillers and power supplies is minimized by placing these devices in a separate service room.

The optical table was installed in May 2011. First phase stable multi-THz pulses were generated and electro-optically detected in October 2011. Figure F.1(b) shows a current snapshot of the laboratory.

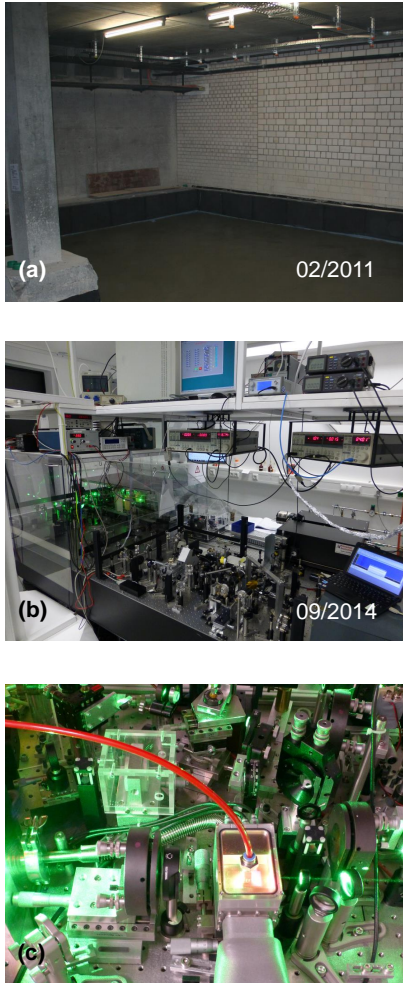


Figure F.1:

Impressions of the femtosecond multi-THz laboratory. (a) Refurbished basement room in early 2011 designated to host the femtosecond multi-THz laboratory (picture by Martin Furthmeier). (b) Laboratory in the present state. (c) Close-up view of part of the experimental setup (Ti:sapphire four-pass amplifier).

Appendix G

Publications in peer-reviewed journals

- J. M. Ménard, C. Poellmann, M. Porer, U. Leierseder, E. Galopin, A. Lemaître, A. Amo, J. Bloch, and R. Huber, *Revealing the dark side of a bright exciton-polariton condensate*, *Nature Communications* **5**, 4648 (2014).
- M. Porer, U. Leierseder, J.-M. Ménard, H. Dachraoui, L. Mouchliadis, I. E. Perakis, U. Heinzmann, J. Demsar, K. Rossnagel, and R. Huber, *Non-thermal separation of electronic and structural orders in a persisting charge density wave*, *Nature Materials* **13**, 857-861 (2014).
- M. Porer, J.-M. Ménard, and R. Huber, *Shot noise reduced terahertz detection via spectrally postfiltered electro-optic sampling*, *Optics Letters* **39**, 2435 (2014).
- H. Dachraoui, G. van der Laan, N. Müller, T. Milde, M. Porer, R. Manzke, R. Huber, S. Fritzsche and U. Heinzmann, *Mapping spin-orbit activated interchannel coupling*, *Europhysics Letters* **106**, 13001 (2014).
- K. W. Kim, A. Pashkin, H. Schäfer, M. Beyer, M. Porer, T. Wolf, C. Bernhard, J. Demsar, R. Huber, and A. Leitenstorfer, *Ultrafast transient generation of spin-density-wave order in the normal state of BaFe₂As₂ driven by coherent lattice vibrations*, *Nature Materials* **11**, 497 (2012).
- M. Porer, J.-M. Ménard, A. Leitenstorfer, R. Huber, R. Degl'Innocenti, S. Zanotto, G. Biasiol, L. Sorba, and A. Tredicucci, *Nonadiabatic switching of a photonic band structure: Ultrastrong light-matter coupling and slow-down of light*, *Physical Review B* (rapid communications) **85**, 081302 (2012).
- A. Pashkin, M. Porer, M. Beyer, K. Kim, A. Dubroka, C. Bernhard, X. Yao, Y. Dagan, R. Hackl, A. Erb, J. Demsar, R. Huber, and A. Leitenstorfer, *Femtosecond response of quasiparticles and phonons in superconducting YBa₂Cu₃O_{7-δ} studied by wideband terahertz spectroscopy*, *Physical Review Letters* **105**, 067001 (2010).

Invited and contributed talks at international conferences

- M. Porer, J.-M. Ménard, H. Dachraoui, U. Leierseder, K. Groh, J. Demsar, U. Heinzmann, and R. Huber, *A multi-terahertz view of ultrafast charge density wave dynamics in $TiSe_2$* , CLEO/QELS Fundamental Science 2013.
- M. Porer, J.-M. Ménard, H. Dachraoui, U. Leierseder, K. Groh, J. Demsar, U. Heinzmann, and R. Huber, *Femtosecond low-energy dynamics of a charge density wave in $TiSe_2$* , CLEO EUROPE/IQEC 2013.
- M. Porer, J.-M. Ménard, A. Leitenstorfer, R. Huber, S. Zanotto, R. Degl'Innocenti, G. Biasiol, L. Sorba, and A. Tredicucci, *Sub-Cycle Manipulation of a Photonic Band Structure via Femtosecond Activation of Ultrastrong Light Matter Interaction* (invited talk), PQE conference 2012.
- M. Porer, A. Pashkin, K.W. Kim, C. Bernhard, X. Yao, Y. Dagan, R. Hackl, A. Erb, M. Beyer, J. Demsar, A. Leitenstorfer, R. Huber, *Ultrafast Phonon and Quasiparticle Dynamics in Superconducting $YBa_2Cu_3O_{7-\delta}$ Studied by Multi-THz Spectroscopy*, Ultrafast Phenomena XVII: Proceedings of the 17th International Conference, Eds. M. Chergui, D.M. Jonas, E. Riedle, R.W. Schoenlein, A.J. Taylor, Oxford University Press, 137-139 (2011).
- M. Porer, A. Pashkin, M. Beyer, K. W. Kim, C. Bernhard, X. Yao, Y. Dagan, R. Hackl, A. Erb, J. Demsar, A. Leitenstorfer, and R. Huber, *Ultrabroadband THz Study of the Femtosecond Phonon and Quasiparticle Dynamics in Superconducting $YBa_2Cu_3O_{7-\delta}$* , EOS Annual Meeting 2010.
- M. Porer, A. Pashkin, M. Beyer, J. Hees, K. W. Kim, C. Bernhard, X. Yao, Y. Dagan, R. Hackl, A. Erb, J. Demsar, A. Leitenstorfer, and R. Huber, *A Femtosecond Multi-Terahertz View of the Phonon and Quasiparticle Dynamics in Superconducting $YBCO$* , CLEO/QELS Fundamental Science 2010.

Conference posters

- M. Porer, J.-M. Ménard, R. Degl'Innocenti, S. Zanotto, G. Biasol, L. Sorba, A. Tredicucci, A. Pashkin, A. Leitenstorfer, and R. Huber, *Nonadiabatic switching of a Photonic Band Structure by Sub-Cycle Activation of Ultrastrong Light-Matter Interaction*, Trends in Nanoscience 2013.
- M. Porer, J.-M. Ménard, A. Leitenstorfer, R. Huber, R. Degl'Innocenti, S. Zanotto, G. Biasol, L. Sorba, and A. Tredicucci, *Nonadiabatic build-up of ultrastrong light-matter coupling in a photonic band structure*, POLATOM-ESF summer school 2012.

Bibliography

- [All87] P. B. Allen, *Theory of thermal relaxation of electrons in metals*, Physical Review Letters **59**, 1460 (1987).
- [Ana09] A. A. Anappara, S. De Liberato, A. Tredicucci, C. Ciuti, G. Biasiol, L. Sorba, and F. Beltram, *Signatures of the ultrastrong light-matter coupling regime*, Physical Review B **79**, 201303(R) (2009).
- [And94] N. F. Andreyev, A. Z. Matveyev, A. A. Kocherov, O. Palashov, G. Pasmanik, and E. Khazanov, *Phase conjugation to upgrade efficiency of solid-state-laser energy conversion to narrow-band TEM00 mode pulses*, Quantum Electronics, IEEE Journal of **30**, 305 (1994).
- [And07] P. W. Anderson, *Is There Glue in Cuprate Superconductors?*, Science **316**, 1705 (2007).
- [Ave01] R. D. Averitt, G. Rodriguez, A. I. Lobad, J. L. W. Siders, S. A. Trugman, and A. J. Taylor, *Nonequilibrium superconductivity and quasiparticle dynamics in $YBa_2Cu_3O_{7-\delta}$* , Physical Review B **63**, 140502 (2001).
- [Bac95] S. Backus, J. Peatross, C. P. Huang, M. M. Murnane, and H. C. Kapteyn, *Ti:sapphire amplifier producing millijoule-level, 21-fs pulses at 1 kHz*, Optics Letters **20**, 2000 (1995).
- [Bal97] A. Baltuška, Z. Wei, M. Pshenichnikov, D. Wiersma, and R. Szipőcs, *All-solid-state cavity-dumped sub-5-fs laser*, Applied Physics B **65**, 175 (1997).
- [Bar57] J. Bardeen, L. N. Cooper, and J. R. Schrieffer, *Theory of Superconductivity*, Physical Review **108**, 1175 (1957).
- [Bar68] A. S. Barker, *Dielectric Dispersion and Phonon Line Shape in Gallium Phosphide*, Physical Review **165**, 917 (1968).
- [Bar08] H. Barath, M. Kim, J. F. Karpus, S. L. Cooper, P. Abbamonte, E. Fradkin,

- E. Morosan, and R. J. Cava, *Quantum and Classical Mode Softening Near the Charge-Density-Wave-Superconductor Transition of Cu_xTiSe_2* , Physical Review Letters **100**, 106402 (2008).
- [Bas05] D. N. Basov and T. Timusk, *Electrodynamics of high- T_c superconductors*, Reviews of Modern Physics **77**, 721 (2005).
- [Bat87a] B. Batlogg, R. J. Cava, A. Jayaraman, R. B. van Dover, G. A. Kourouklis, S. Sunshine, D. W. Murphy, L. W. Rupp, H. S. Chen, A. White, K. T. Short, A. M. Muisce, and E. A. Rietman, *Isotope Effect in the High- T_c Superconductors $Ba_2YC_{u3}O_7$ and $Ba_2EuCu_3O_7$* , Physical Review Letters **58**, 2333 (1987).
- [Bat87b] B. Batlogg, G. Kourouklis, W. Weber, R. J. Cava, A. Jayaraman, A. E. White, K. T. Short, L. W. Rupp, and E. A. Rietman, *Nonzero isotope effect in $La_{1.85}Sr_{0.15}CuO_4$* , Physical Review Letters **59**, 912 (1987).
- [Bat89] F. E. Bates, *Normal modes of tetragonal $YBa_2Cu_3O_6$ and orthorhombic $YBa_2Cu_3O_7$* , Physical Review B **39**, 322 (1989).
- [Bed86] G. Bednorz and A. Müller, *Possible high- T_c superconductivity in the $Ba-La-Cu-O$ system*, Zeitschrift für Physik B **64**, 189 (1986).
- [Bel10] F. Belgiorno, S. L. Cacciatori, M. Clerici, V. Gorini, G. Ortenzi, L. Rizzi, E. Rubino, V. G. Sala, and D. Faccio, *Hawking Radiation from Ultrashort Laser Pulse Filaments*, Physical Review Letters **105**, 203901 (2010).
- [Ber00] C. Bernhard, D. Munzar, A. Golnik, C. T. Lin, A. Wittlin, J. Humlíček, and M. Cardona, *Anomaly of oxygen bond-bending mode at 320 cm^{-1} and additional absorption peak in the c -axis infrared conductivity of underdoped $YBa_2Cu_3O_{7-\delta}$ single crystals revisited with ellipsometric measurements*, Physical Review B **61**, 618 (2000).
- [Ber04] C. Bernhard, J. Humlíček, and B. Keimer, *Far-infrared ellipsometry using a synchrotron light source—the dielectric response of the cuprate high T_c superconductors*, Thin Solid Films **455–456**, 143 (2004), The 3rd International Conference on Spectroscopic Ellipsometry.
- [Bha14] P. Bhattacharya, T. Frost, S. Deshpande, M. Z. Baten, A. Hazari, and A. Das, *Room Temperature Electrically Injected Polariton Laser*, Physical Review Letters **112**, 236802 (2014).
- [Big03] M. S. Bigelow, N. N. Lepeshkin, and R. W. Boyd, *Superluminal and slow light propagation in a room-temperature solid.*, Science **301**, 200 (2003).
- [Bla13] F. Blanchard, A. Doi, T. Tanaka, and K. Tanaka, *Real-Time, Subwavelength Terahertz Imaging*, Annual Review of Materials Research **43**, 237 (2013).

- [Bog47] N. N. Bogoliubov, *On the Theory of Superfluidity*, Journal of Physics (USSR) **11**, 23–32 (1947).
- [Bon95] A. Bonvalet, M. Joffre, J. L. Martin, and A. Migus, *Generation of ultrabroad-band femtosecond pulses in the mid-infrared by optical rectification of 15 fs light pulses at 100 MHz repetition rate*, Applied Physics Letters **67**, 2907 (1995).
- [Bor99] M. Born, E. Wolf, A. Bhatia, P. Clemmow, D. Gabor, A. Stokes, A. Taylor, P. Wayman, and W. Wilcock, *Principles of Optics: Electromagnetic Theory of Propagation, Interference and Diffraction of Light*, Cambridge University Press, 7th (extended) edition edition (1999).
- [Bor04] A. V. Boris, N. N. Kovaleva, O. V. Dolgov, T. Holden, C. T. Lin, B. Keimer, and C. Bernhard, *In-Plane Spectral Weight Shift of Charge Carriers in $YBa_2Cu_3O_{6.9}$* , Science **304**, 708 (2004).
- [Bra00] T. Brabec and F. Krausz, *Intense few-cycle laser fields: Frontiers of nonlinear optics*, Reviews of Modern Physics **72**, 545 (2000).
- [Bre02] G. Bressi, G. Carugno, R. Onofrio, and G. Ruoso, *Measurement of the Casimir Force between Parallel Metallic Surfaces*, Physical Review Letters **88**, 041804 (2002).
- [Bus93] T. Buslaps, R. Johnson, and G. Jungk, *Spectroscopic ellipsometry on 1T-TiSe₂, Thin Solid Films* **234**, 549 (1993).
- [Cal11] M. Calandra and F. Mauri, *Charge-Density Wave and Superconducting Dome in TiSe₂ from Electron-Phonon Interaction*, Physical Review Letters **106**, 196406 (2011).
- [Car03] D. Cardwell and D. Ginley, *Handbook of Superconducting Materials*, Handbook of Superconducting Materials. CRC Press (2003).
- [Cav90] R. Cava, A. Hewat, E. Hewat, B. Batlogg, M. Marezio, K. Rabe, J. Krajewski, W. Peck Jr., and L. Rupp Jr., *Structural anomalies, oxygen ordering and superconductivity in oxygen deficient $Ba_2 YCu_3 O_x$* , Physica C: Superconductivity **165**, 419 (1990).
- [Cer07] H. Cercellier, C. Monney, F. Clerc, C. Battaglia, L. Despont, M. Garnier, H. Beck, P. Aebi, L. Patthey, H. Berger, and Forró, *Evidence for an Excitonic Insulator Phase in 1T-TiSe₂*, Physical Review Letters **99**, 146403 (2007).
- [Cha12] J. Chang, E. Blackburn, A. T. Holmes, N. B. Christensen, J. Larsen, J. Mesot, R. Liang, D. A. Bonn, W. N. Hardy, A. Watenphul, M. v. Zimmermann, E. M. Forgan, and S. M. Hayden, *Direct observation of competition between superconductivity and charge density wave order in $YBa_2Cu_3O_{6.67}$* , Nature Physics **8**, 672 (2012).

- 8, 871 (2012).
- [Chh13] M. Chhowalla, H. S. Shin, G. Eda, L.-J. Li, K. P. Loh, and H. Zhang, *The chemistry of two-dimensional layered transition metal dichalcogenide nanosheets*, Nature Chemistry **5**, 263 (2013).
- [Ciu05] C. Ciuti, G. Bastard, and I. Carusotto, *Quantum vacuum properties of the intersubband cavity polariton field*, Physical Review B **72**, 115303 (2005).
- [Coe87] R. Coehoorn, C. Haas, and R. A. de Groot, *Electronic structure of MoSe₂, MoS₂, and WSe₂. II. The nature of the optical band gaps*, Physical Review B **35**, 6203 (1987).
- [Coh14] Coherent, *Data Sheet RegA 9000-9050, "RegA, High Repetition-Rate, Femtosecond Ti:Sapphire Amplifiers"*, Coherent, Inc., 5100 Patrick Henry Drive, Santa Clara, CA 95054 (2014).
- [Cra78] R. Craven, F. D. Salvo, and F. Hsu, *Mechanisms for the 200 K transition in TiSe₂: A measurement of the specific heat*, Solid State Communications **25**, 39 (1978).
- [Cuk04] T. Cuk, F. Baumberger, D. H. Lu, N. Ingle, X. J. Zhou, H. Eisaki, N. Kaneko, Z. Hussain, T. P. Devereaux, N. Nagaosa, and Z.-X. Shen, *Coupling of the B_{1g} Phonon to the Antinodal Electronic States of Bi₂Sr₂Ca_{0.92}Y_{0.08}Cu₂O_{8+δ}*, Physical Review Letters **93**, 117003 (2004).
- [Dag05] E. Dagotto, *Complexity in Strongly Correlated Electronic Systems*, Science **309**, 257 (2005).
- [Dai06] J. Dai, X. Xie, and X.-C. Zhang, *Detection of Broadband Terahertz Waves with a Laser-Induced Plasma in Gases*, Physical Review Letters **97**, 103903 (2006).
- [Dai12] P. Dai, J. Hu, and E. Dagotto, *Magnetism and its microscopic origin in iron-based high-temperature superconductors*, Nature Physics **8**, 709 (2012).
- [Dan07] A. Dantan, J. Laurat, A. Ourjoumtsev, R. Tualle-Brouri, and P. Grangier, *Femtosecond Ti:sapphire cryogenic amplifier with high gain and MHz repetition rate*, Optics Express **15**, 8864 (2007).
- [Dar11] J. Darmo, D. Dietze, M. Martl, and K. Unterrainer, *Nonorthodox heterodyne electro-optic detection for terahertz optical systems*, Applied Physics Letters **98**, 161112 (2011).
- [Dem99] J. Demsar, B. Podobnik, V. V. Kabanov, T. Wolf, and D. Mihailovic, *Superconducting Gap Δ_c , the Pseudogap Δ_p , and Pair Fluctuations above T_c in Overdoped $Y_{1-x}Ca_xBa_2Cu_3O_{7-\delta}$ from Femtosecond Time-Domain Spec-*

- troscopy*, Physical Review Letters **82**, 4918 (1999).
- [Den02] H. Deng, G. Weihs, C. Santori, J. Bloch, and Y. Yamamoto, *Condensation of Semiconductor Microcavity Exciton Polaritons*, Science **298**, 199 (2002).
- [Din03] D. Dini, R. Köhler, A. Tredicucci, G. Biasiol, and L. Sorba, *Microcavity Polariton Splitting of Intersubband Transitions*, Physical Review Letters **90**, 116401 (2003).
- [Dre02] M. Dressel and G. Grüner, *Electrodynamics of Solids: Optical Properties of Electrons in Matter*, Cambridge University Press (2002).
- [DS76] F. J. Di Salvo, D. E. Moncton, and J. V. Waszczak, *Electronic properties and superlattice formation in the semimetal $TiSe_2$* , Physical Review B **14**, 4321 (1976).
- [Dup07] E. Dupont, J. A. Gupta, and H. C. Liu, *Giant vacuum-field Rabi splitting of intersubband transitions in multiple quantum wells*, Physical Review B **75**, 205325 (2007).
- [Eis14] M. Eisele, L. T. Cocker, A. M. Huber, M. Plankl, L. Viti, D. Ercolani, L. Sorba, S. M. Vitiello, and R. Huber, *Ultrafast multi-terahertz nano-spectroscopy with sub-cycle temporal resolution*, Nature Photonics **8**, 841–845 (2014).
- [Ell01] R. Ell, U. Morgner, F. X. Kärtner, J. G. Fujimoto, E. P. Ippen, V. Scheuer, G. Angelow, T. Tschudi, M. J. Lederer, A. Boiko, and B. Luther-Davies, *Generation of 5-fs pulses and octave-spanning spectra directly from a Ti:sapphire laser*, Optics Letters **26**, 373 (2001).
- [Fan84] Y. X. Fan, R. C. Eckardt, R. L. Byer, R. K. Route, and R. S. Feigelson, *$AgGaS_2$ infrared parametric oscillator*, Applied Physics Letters **45**, 313 (1984).
- [Fau11] D. Fausti, R. I. Tobey, N. Dean, S. Kaiser, A. Dienst, M. C. Hoffmann, S. Pyon, T. Takayama, H. Takagi, and A. Cavalleri, *Light-Induced Superconductivity in a Stripe-Ordered Cuprate*, Science **331**, 189 (2011).
- [Faw88] E. Fawcett, *Spin-density-wave antiferromagnetism in chromium*, Reviews of Modern Physics **60**, 209 (1988).
- [FD10] P. Forn-Díaz, J. Lisenfeld, D. Marcos, J. J. García-Ripoll, E. Solano, C. J. P. M. Harmans, and J. E. Mooij, *Observation of the Bloch-Siegert Shift in a Qubit-Oscillator System in the Ultrastrong Coupling Regime*, Physical Review Letters **105**, 237001 (2010).
- [Fer02] B. Ferguson and X.-C. Zhang, *Materials for terahertz science and technology*, Nature Materials **1**, 26 (2002).

- [Fri07] D. M. Fritz, D. A. Reis, B. Adams, R. A. Akre, J. Arthur, C. Blome, P. H. Bucksbaum, A. L. Cavalieri, S. Engemann, S. Fahy, R. W. Falcone, P. H. Fuoss, K. J. Gaffney, M. J. George, J. Hajdu, M. P. Hertlein, P. B. Hillyard, M. Horn-von Hoegen, M. Kammler, J. Kaspar, R. Kienberger, P. Krejcik, S. H. Lee, A. M. Lindenberg, B. McFarland, D. Meyer, T. Montagne, E. D. Murray, A. J. Nelson, M. Nicoul, R. Pahl, J. Rudati, H. Schlarb, D. P. Siddons, K. Sokolowski-Tinten, T. Tschentscher, D. von der Linde, and J. B. Hastings, *Ultrafast Bond Softening in Bismuth: Mapping a Solid's Interatomic Potential with X-rays*, *Science* **315**, 633 (2007).
- [Ful76] S. A. Fulling and P. C. W. Davies, *Radiation from a Moving Mirror in Two Dimensional Space-Time: Conformal Anomaly*, *Proceedings of the Royal Society of London. A. Mathematical and Physical Sciences* **348**, 393 (1976).
- [Gal99] G. Gallot and D. Grischkowsky, *Electro-optic detection of terahertz radiation*, *Journal of the Optical Society of America B: Optical Physics* **16**, 1204 (1999).
- [Gan05] S. Ganichev and W. Prettl, *Intense Terahertz Excitation of Semiconductors*, Series on Semiconductor Science and Technology. Oxford University Press (2005).
- [Gao94] L. Gao, Y. Y. Xue, F. Chen, Q. Xiong, R. L. Meng, D. Ramirez, C. W. Chu, J. H. Eggert, and H. K. Mao, *Superconductivity up to 164 K in $HgBa_2Ca_{m-1}Cu_mO_{2m+2+\delta}$ ($m=1, 2$, and 3) under quasihydrostatic pressures*, *Physical Review B* **50**, 4260 (1994).
- [Ged07] N. Gedik, D.-S. Yang, G. Logvenov, I. Bozovic, and A. H. Zewail, *Nonequilibrium Phase Transitions in Cuprates Observed by Ultrafast Electron Crystallography*, *Science* **316**, 425 (2007).
- [Gei07] A. K. Geim and K. S. Novoselov, *The rise of graphene*, *Nature Materials* **6**, 183 (2007).
- [Gei10] M. Geiser, C. Walther, G. Scalari, M. Beck, M. Fischer, L. Nevou, and J. Faist, *Strong light-matter coupling at terahertz frequencies at room temperature in electronic LC resonators*, *Applied Physics Letters* **97**, 191107 (2010).
- [Grü94] G. Grüner, *Density Waves in Solids*, Frontiers in physics. Addison-Wesley Publishing Company, Advanced Book Program (1994).
- [Gün09] G. Günter, A. A. Anappara, J. Hees, A. Sell, G. Biasiol, L. Sorba, S. De Liberato, C. Ciuti, A. Tredicucci, A. Leitenstorfer, and R. Huber, *Sub-cycle switch-on of ultrastrong lightmatter interaction*, *Nature* **458**, 178 (2009).
- [Has14] M. Hashimoto, E. A. Nowadnick, R.-H. He, I. M. Vishik, B. Moritz, Y. He, K. Tanaka, R. G. Moore, D. Lu, Y. Yoshida, M. Ishikado, T. Sasagawa, K. Fu-

- jita, S. Ishida, S. Uchida, H. Eisaki, Z. Hussain, T. P. Devereaux, and Z.-X. Shen, *Direct spectroscopic evidence for phase competition between the pseudogap and superconductivity in $Bi_2Sr_2CaCu_2O_{8+\delta}$* , Nature Materials **advance online publication**, (2014).
- [Hau10] D. Haug, V. Hinkov, Y. Sidis, P. Bourges, N. B. Christensen, A. Ivanov, T. Keller, C. T. Lin, and B. Keimer, *Neutron scattering study of the magnetic phase diagram of underdoped $YBa_2Cu_3O_{6+x}$* , New Journal of Physics **12**, 105006 (2010).
- [Hay14] L. E. Hayward, D. G. Hawthorn, R. G. Melko, and S. Sachdev, *Angular Fluctuations of a Multicomponent Order Describe the Pseudogap of $YBa_2Cu_3O_{6+x}$* , Science **343**, 1336 (2014).
- [He14a] K. He, N. Kumar, L. Zhao, Z. Wang, K. F. Mak, H. Zhao, and J. Shan, *Tightly Bound Excitons in Monolayer WSe₂*, Physical Review Letters **113**, 026803 (2014).
- [He14b] Y. He, Y. Yin, M. Zech, A. Soumyanarayanan, M. M. Yee, T. Williams, M. C. Boyer, K. Chatterjee, W. D. Wise, I. Zeljkovic, T. Kondo, T. Takeuchi, H. Ikuta, P. Mistark, R. S. Markiewicz, A. Bansil, S. Sachdev, E. W. Hudson, and J. E. Hoffman, *Fermi Surface and Pseudogap Evolution in a Cuprate Superconductor*, Science **344**, 608 (2014).
- [Heb04] J. Hebling, A. Stepanov, G. Almási, B. Bartal, and J. Kuhl, *Tunable THz pulse generation by optical rectification of ultrashort laser pulses with tilted pulse fronts*, Applied Physics B **78**, 593 (2004).
- [Hel12] S. Hellmann, T. Rohwer, M. Kalláne, K. Hanff, C. Sohrt, A. Stange, A. Carr, M. Murnane, H. Kapteyn, L. Kipp, M. Bauer, and K. Rossnagel, *Time-domain classification of charge-density-wave insulators*, Nature Communications **3**, 1069 (2012).
- [Hol77] J. Holy, K. Woo, M. Klein, and F. Brown, *Raman and infrared studies of superlattice formation in TiSe₂*, Physical Review B **16**, 3628 (1977).
- [Hol01] M. Holt, P. Zschack, H. Hong, M. Y. Chou, and T.-C. Chiang, *X-Ray Studies of Phonon Softening in TiSe₂*, Physical Review Letters **86**, 3799 (2001).
- [Hop58] J. J. Hopfield, *Theory of the Contribution of Excitons to the Complex Dielectric Constant of Crystals*, Physical Review **112**, 1555 (1958).
- [Hot13] R. Hott, R. Kleiner, T. Wolf, and G. Zwicknagl, *Review on Superconducting Materials*, arXiv:1306.0429 [cond-mat.supr-con], to be published in “Handbook of Applied Superconductivity”, Wiley-VCH (2013).

- [Hub00] R. Huber, A. Brodschelm, F. Tauser, and A. Leitenstorfer, *Generation and field-resolved detection of femtosecond electromagnetic pulses tunable up to 41 THz*, Applied Physics Letters **76**, 3191 (2000).
- [Hub01] R. Huber, F. Tauser, A. Brodschelm, M. Bichler, G. Abstreiter, and A. Leitenstorfer, *How many-particle interactions develop after ultrafast excitation of an electron-hole plasma*, Nature **414**, 286 (2001).
- [Hub03] R. Huber, F. Adler, A. Leitenstorfer, M. Beutter, P. Baum, and E. Riedle, *12-fs pulses from a continuous-wave-pumped 200-nJ Ti:sapphire amplifier at a variable repetition rate as high as 4 MHz*, Optics Letters **28**, 2118 (2003).
- [Hub04] R. Huber, *Ultraschneller Aufbau von Coulomb Korrelationen untersucht mit Femtosekunden-THz-Spektroskopie*, Ph.D. thesis (2004).
- [Hüf08] S. Hüfner, M. A. Hossain, A. Damascelli, and G. A. Sawatzky, *Two gaps make a high-temperature superconductor?*, Reports on Progress in Physics **71**, 062501 (2008).
- [Hug77] H. P. Hughes, *Structural distortion in $TiSe_2$ and related materials-a possible Jahn-Teller effect?*, Journal of Physics C: Solid State Physics **10**, L319 (1977).
- [Hum00] J. Humliček, R. Henn, and M. Cardona, *Infrared vibrations in $LaSrGaO_4$ and $LaSrAlO_4$* , Physical Review B **61**, 14554 (2000).
- [Hut72] M. T. Hutchings and E. J. Samuelsen, *Measurement of Spin-Wave Dispersion in NiO by Inelastic Neutron Scattering and Its Relation to Magnetic Properties*, Physical Review B **6**, 3447 (1972).
- [Ish10] J. Ishioka, Y. H. Liu, K. Shimatake, T. Kurosawa, K. Ichimura, Y. Toda, M. Oda, and S. Tanda, *Chiral Charge-Density Waves*, Physical Review Letters **105**, 176401 (2010).
- [Iwa08] H. Iwasawa, J. F. Douglas, K. Sato, T. Masui, Y. Yoshida, Z. Sun, H. Eisaki, H. Bando, A. Ino, M. Arita, K. Shimada, H. Namatame, M. Taniguchi, S. Tajima, S. Uchida, T. Saitoh, D. S. Dessau, and Y. Aiura, *Isotopic Fingerprint of Electron-Phonon Coupling in High- T_c Cuprates*, Physical Review Letters **101**, 157005 (2008).
- [Jac12] R. Jacob, S. Winnerl, M. Fehrenbacher, J. Bhattacharyya, H. Schneider, M. T. Wenzel, H.-G. v. Ribbeck, L. M. Eng, P. Atkinson, O. G. Schmidt, and M. Helm, *Intersublevel Spectroscopy on Single InAs-Quantum Dots by Terahertz Near-Field Microscopy*, Nano Letters **12**, 4336 (2012).
- [Jér67] D. Jérôme, T. M. Rice, and W. Kohn, *Excitonic Insulator*, Physical Review **158**, 462 (1967).

- [Joa08] J. D. Joannopoulos, S. G. Johnson, J. N. Winn, and R. D. Meade, *Photonic Crystals: Molding the Flow of Light (second edition)*, Princeton University Press, Princeton, NJ, USA (2008).
- [Joe14] Y. I. Joe, X. M. Chen, P. Ghaemi, K. D. Finkelstein, G. A. de la Pena, Y. Gan, J. C. T. Lee, S. Yuan, J. Geck, G. J. MacDougall, T. C. Chiang, S. L. Cooper, E. Fradkin, and P. Abbamonte, *Emergence of charge density wave domain walls above the superconducting dome in 1T-TiSe₂*, *Nature Physics* **10**, 421 (2014).
- [Joh08] M. D. Johannes and I. I. Mazin, *Fermi surface nesting and the origin of charge density waves in metals*, *Physical Review B* **77**, 165135 (2008).
- [Kab99] V. V. Kabanov, J. Demsar, B. Podobnik, and D. Mihailovic, *Quasiparticle relaxation dynamics in superconductors with different gap structures: Theory and experiments on YBa₂Cu₃O_{7-δ}*, *Physical Review B* **59**, 1497 (1999).
- [Kab08] V. V. Kabanov and A. S. Alexandrov, *Electron relaxation in metals: Theory and exact analytical solutions*, *Physical Review B* **78**, 174514 (2008).
- [Kai00] R. A. Kaindl, M. Woerner, T. Elsaesser, D. C. Smith, J. F. Ryan, G. A. Farnan, M. P. McCurry, and D. G. Walmsley, *Ultrafast Mid-Infrared Response of YBa₂Cu₃O_{7-δ}*, *Science* **287**, 470 (2000).
- [Kam08] Y. Kamihara, T. Watanabe, M. Hirano, and H. Hosono, *Iron-Based Layered Superconductor La[O_{1-x}F_x]FeAs (x = 0.05-0.12) with T_c = 26 K*, *Journal of the American Chemical Society* **130**, 3296 (2008).
- [Kam11] T. Kampfrath, A. Sell, G. Klatt, A. Pashkin, S. Mährlein, T. Dekorsy, M. Wolf, M. Fiebig, A. Leitenstorfer, and R. Huber, *Coherent terahertz control of antiferromagnetic spin waves*, *Nature Photonics* **5**, 31 (2011).
- [Kam13] T. Kampfrath, K. Tanaka, and K. A. Nelson, *Resonant and nonresonant control over matter and light by intense terahertz transients*, *Nature Photonics* **7**, 680 (2013).
- [Kas06] J. Kasprzak, M. Richard, S. Kundermann, A. Baas, P. Jeambrun, J. M. J. Keeling, F. M. Marchetti, M. H. Szymanska, R. Andre, J. L. Staehli, V. Savona, P. B. Littlewood, B. Deveaud, and L. S. Dang, *Bose-Einstein condensation of exciton polaritons*, *Nature* **443**, 409 (2006).
- [Kid02] T. E. Kidd, T. Miller, M. Y. Chou, and T.-C. Chiang, *Electron-Hole Coupling and the Charge Density Wave Transition in TiSe₂*, *Physical Review Letters* **88**, 226402 (2002).
- [Kim12] K. W. Kim, A. Pashkin, H. Schäfer, M. Beyer, M. Porer, T. Wolf, C. Bernhard, J. Demsar, R. Huber, and A. Leitenstorfer, *Ultrafast transient generation of*

- spin-density-wave order in the normal state of $BaFe_2As_2$ driven by coherent lattice vibrations*, Nature Materials **11**, 497 (2012).
- [Kin99] J. T. Kindt and C. A. Schmuttenmaer, *Theory for determination of the low-frequency time-dependent response function in liquids using time-resolved terahertz pulse spectroscopy*, The Journal of Chemical Physics **110**, 8589 (1999).
- [Kis07] T. Kiss, T. Yokoya, A. Chainani, S. Shin, T. Hanaguri, M. Nohara, and H. Takagi, *Charge-order-maximized momentum-dependent superconductivity*, Nature Physics **3**, 720 (2007).
- [Kit04] C. Kittel, *Introduction to Solid State Physics*, Wiley (2004).
- [Kli07] C. Klingshirn, *Semiconductor Optics*, Advanced texts in physics. Springer (2007).
- [Kme91] J. D. Kmetec, J. J. Macklin, and J. F. Young, *0.5-TW, 125-fs Ti:sapphire laser*, Optics Letters **16**, 1001 (1991).
- [Kog72] H. Kogelnik, E. Ippen, A. Dienes, and C. Shank, *Astigmatically compensated cavities for CW dye lasers*, IEEE Journal of Quantum Electronics **8**, 373 (1972).
- [Kra10] G. Krauss, S. Lohss, T. Hanke, A. Sell, S. Eggert, R. Huber, and A. Leitenstorfer, *Synthesis of a single cycle of light with compact erbium-doped fibre technology*, Nature Photonics **4**, 33 (2010).
- [Ku04] P.-C. Ku, F. Sedgwick, C. J. Chang-Hasnain, P. Palinginis, T. Li, H. Wang, S.-W. Chang, and S.-L. Chuang, *Slow light in semiconductor quantum wells*, Optics Letters **29**, 2291 (2004).
- [Küb04] C. Kübler, R. Huber, S. Tübel, and A. Leitenstorfer, *Ultrabroadband detection of multi-terahertz field transients with GaSe electro-optic sensors: Approaching the near infrared*, Applied Physics Letters **85**, 3360 (2004).
- [Küb05] C. Kübler, R. Huber, and A. Leitenstorfer, *Ultrabroadband terahertz pulses: generation and field-resolved detection*, Semiconductor Science and Technology **20**, S128 (2005).
- [Küb07] C. Kübler, *Femtosecond Terahertz Studies of Many-Body Correlations: From Ultrafast Phonon-Plasmon Dynamics to an Insulator-Metal Transition*, Ph.D. thesis, Universität Konstanz (2007).
- [Kus08] P. Kusar, V. V. Kabanov, J. Demsar, T. Mertelj, S. Sugai, and D. Mihailovic, *Controlled Vaporization of the Superconducting Condensate in Cuprate Superconductors by Femtosecond Photoexcitation*, Physical Review Letters **101**, 227001 (2008).

- [Kus09] A. F. Kusmartseva, B. Sipos, H. Berger, L. Forró, and E. Tutíš, *Pressure Induced Superconductivity in Pristine 1T-TiSe₂*, Physical Review Letters **103**, 236401 (2009).
- [Lan01] A. Lanzara, P. V. Bogdanov, X. J. Zhou, S. A. Kellar, D. L. Feng, E. D. Lu, T. Yoshida, H. Eisaki, A. Fujimori, K. Kishio, J.-I. Shimoyama, T. Noda, S. Uchida, Z. Hussain, and Z.-X. Shen, *Evidence for ubiquitous strong electron-phonon coupling in high-temperature superconductors*, Nature **412**, 510 (2001).
- [Lee00] Y.-S. Lee, T. Meade, V. Perlin, H. Winful, T. B. Norris, and A. Galvanauskas, *Generation of narrow-band terahertz radiation via optical rectification of femtosecond pulses in periodically poled lithium niobate*, Applied Physics Letters **76**, 2505 (2000).
- [Lee06] J. Lee, K. Fujita, K. McElroy, J. A. Slezak, M. Wang, Y. Aiura, H. Bando, M. Ishikado, T. Masui, J.-X. Zhu, A. V. Balatsky, H. Eisaki, S. Uchida, and J. C. Davis, *Interplay of electron-lattice interactions and superconductivity in Bi₂Sr₂CaCu₂O_{8+δ}*, Nature **442**, 546 (2006).
- [Lei08] S. Leinss, T. Kampfrath, K. v. Volkmann, M. Wolf, J. T. Steiner, M. Kira, S. W. Koch, A. Leitenstorfer, and R. Huber, *Terahertz Coherent Control of Optically Dark Paraexcitons in Cu₂O*, Physical Review Letters **101**, 246401 (2008).
- [Li07a] G. Li, W. Hu, J. Dong, D. Qian, D. Hsieh, M. Hasan, E. Morosan, R. Cava, and N. Wang, *Anomalous Metallic State of Cu_{0.07}TiSe₂: An Optical Spectroscopy Study*, Physical Review Letters **99** (2007).
- [Li07b] G. Li, W. Hu, D. Qian, D. Hsieh, M. Hasan, E. Morosan, R. Cava, and N. Wang, *Semimetal-to-Semimetal Charge Density Wave Transition in 1T-TiSe₂*, Physical Review Letters **99**, 027404 (2007).
- [Lia79] W. Y. Liang, G. Lucovsky, J. C. Mikkelsen, and R. H. Friend, *Infra-red studies of TiSe₂: IR phonons and free carriers*, Philosophical Magazine Part B **39**, 133 (1979).
- [Lib07] S. D. Liberato, C. Ciuti, and I. Carusotto, *Quantum Vacuum Radiation Spectra from a Semiconductor Microcavity with a Time-Modulated Vacuum Rabi Frequency*, Physical Review Letters **98**, 103602 (2007).
- [Lit92] A. Litvinchuk, C. Thomsen, and M. Cardona, *Phonon anomalies above T_c in YBa₂Cu₄O₈ and YBa₂Cu₃O_{7-δ} superconductors: An effect of coupling to spin excitations*, Solid State Communications **83**, 343 (1992).
- [Liu88] R. Liu, C. Thomsen, W. Kress, M. Cardona, B. Gegenheimer, F. W. de Wette, J. Prade, A. D. Kulkarni, and U. Schröder, *Frequencies, eigenvectors, and*

- single-crystal selection rules of $k=0$ phonons in $YBa_2Cu_3O_{7-\delta}$: Theory and experiment*, Physical Review B **37**, 7971 (1988).
- [Liu04] K. Liu, J. Xu, and X.-C. Zhang, *GaSe crystals for broadband terahertz wave detection*, Applied Physics Letters **85**, 863 (2004).
- [Lor93] J. W. Loram, K. A. Mirza, J. R. Cooper, and W. Y. Liang, *Electronic specific heat of $YBa_2Cu_3O_{6+x}$ from 1.8 to 300 K*, Physical Review Letters **71**, 1740 (1993).
- [Mat12] E. Matsubara, M. Nagai, and M. Ashida, *Ultrabroadband coherent electric field from far infrared to 200 THz using air plasma induced by 10 fs pulses*, Applied Physics Letters **101**, 011105 (2012).
- [McI93] I. McIntyre, *Multiple-pass method and apparatus for laser amplification*, US Patent No. 5,268,787 (1993).
- [Mén14] J. M. Ménard, C. Pöllmann, M. Porer, U. Leierseder, E. Galopin, A. Lemaître, A. Amo, J. Bloch, and R. Huber, *Revealing the dark side of a bright exciton-polariton condensate*, Nature Communications **5**, (2014).
- [Mil10] P. W. Milonni and J. H. Eberly, *Laser Physics*, Wiley (2010).
- [Mon07] P. Monthoux, D. Pines, and G. G. Lonzarich, *Superconductivity without phonons*, Nature **450**, 1177 (2007).
- [Mon09] C. Monney, H. Cercellier, F. Clerc, C. Battaglia, E. Schwier, C. Didiot, M. Garnier, H. Beck, P. Aebi, H. Berger, L. Forró, and L. Patthey, *Spontaneous exciton condensation in 1T-TiSe₂: BCS-like approach*, Physical Review B **79**, 045116 (2009).
- [Mon10] C. Monney, E. F. Schwier, M. G. Garnier, N. Mariotti, C. Didiot, H. Cercellier, J. Marcus, H. Berger, A. N. Titov, H. Beck, and P. Aebi, *Probing the exciton condensate phase in 1T-TiSe₂ with photoemission*, New Journal of Physics **12**, 125019 (2010).
- [Mon11] C. Monney, C. Battaglia, H. Cercellier, P. Aebi, and H. Beck, *Exciton Condensation Driving the Periodic Lattice Distortion of 1T-TiSe₂*, Physical Review Letters **106**, 106404 (2011).
- [Moo70] G. T. Moore, *Quantum Theory of the Electromagnetic Field in a Variable-Length One-Dimensional Cavity*, Journal of Mathematical Physics **11**, 2679 (1970).
- [Moo12] K. Moon, Y. Do, M. Lim, G. Lee, H. Kang, K.-S. Park, and H. Han, *Quantitative coherent scattering spectra in apertureless terahertz pulse near-field microscopes*,

- Applied Physics Letters **101**, 011109 (2012).
- [Mor06] E. Morosan, H. W. Zandbergen, B. S. Dennis, J. W. G. Bos, Y. Onose, T. Klimczuk, A. P. Ramirez, N. P. Ong, and R. J. Cava, *Superconductivity in $Cu_x TiSe_2$* , Nature Physics **2**, 544 (2006).
- [Mor10] E. Morosan, K. E. Wagner, L. L. Zhao, Y. Hor, A. J. Williams, J. Tao, Y. Zhu, and R. J. Cava, *Multiple electronic transitions and superconductivity in $Pd_x TiSe_2$* , Physical Review B **81**, 094524 (2010).
- [Mou86] P. F. Moulton, *Spectroscopic and laser characteristics of $Ti:Al_2O_3$* , Journal of the Optical Society of America B: Optical Physics **3**, 125 (1986).
- [Mul08] T. D. Mulder, R. P. Scott, and B. H. Kolner, *Amplitude and envelope phase noise of a modelocked laser predicted from its noise transfer function and the pump noise power spectrum*, Optics Express **16**, 14186 (2008).
- [Mun99] D. Munzar, C. Bernhard, A. Golnik, J. Humliček, and M. Cardona, *Anomalies of the infrared-active phonons in underdoped $YBa_2Cu_3O_y$ as evidence for the intra-bilayer Josephson effect*, Solid State Communications **112**, 365 (1999).
- [MV11] E. Möhr-Vorobeva, S. Johnson, P. Beaud, U. Staub, R. De Souza, C. Milne, G. Ingold, J. Demsar, H. Schaefer, and A. Titov, *Nonthermal Melting of a Charge Density Wave in $TiSe_2$* , Physical Review Letters **107**, 036403 (2011).
- [Nat12] P. D. Nation, J. R. Johansson, M. P. Blencowe, and F. Nori, *Colloquium: Stimulating uncertainty: Amplifying the quantum vacuum with superconducting circuits*, Reviews of Modern Physics **84**, 1 (2012).
- [Ném02] H. Némec, F. Kadlec, and P. Kužel, *Methodology of an optical pump-terahertz probe experiment: An analytical frequency-domain approach*, The Journal of Chemical Physics **117**, 8454 (2002).
- [Ném05] H. Némec, F. Kadlec, S. Surendran, P. Kužel, and P. Jungwirth, *Ultrafast far-infrared dynamics probed by terahertz pulses: A frequency domain approach. I. Model systems*, The Journal of Chemical Physics **122**, 104503 (2005).
- [Nie10] T. Niemczyk, F. Deppe, H. Huebl, E. P. Menzel, F. Hocke, M. J. Schwarz, J. J. Garcia-Ripoll, D. Zueco, T. Hummer, E. Solano, A. Marx, and R. Gross, *Circuit quantum electrodynamics in the ultrastrong-coupling regime*, Nature Physics **6**, 1745 (2010).
- [Onn11] H. K. Onnes, *The Superconductivity of Mercury*, Comm. Leiden pages 120b,122b,124c (1911).
- [Ope99] M. Opel, R. Hackl, T. P. Devereaux, A. Virosztek, A. Zawadowski, A. Erb,

- E. Walker, H. Berger, and L. Forró, *Physical origin of the buckling in CuO₂: Electron-phonon coupling and Raman spectra*, Physical Review B **60**, 9836 (1999).
- [Oza10] A. Ozawa, T. Udem, U. D. Zeitner, T. W. Hänsch, and P. Hommelhoff, *Modeling and optimization of single-pass laser amplifiers for high-repetition-rate laser pulses*, Physical Review A **82**, 033815 (2010).
- [Pag10] J. Paglione and R. L. Greene, *High-temperature superconductivity in iron-based materials*, Nature Physics **6**, 645 (2010).
- [Pas10] A. Pashkin, M. Porer, M. Beyer, K. Kim, A. Dubroka, C. Bernhard, X. Yao, Y. Dagan, R. Hackl, A. Erb, *et al.*, *Femtosecond response of quasiparticles and phonons in superconducting YBa₂Cu₃O_{7-δ} studied by wideband terahertz spectroscopy*, Physical Review Letters **105**, 067001 (2010).
- [Pei55] R. Peierls, *Quantum Theory of Solids*, Oxford University Press (1955).
- [Per07] L. Perfetti, P. A. Loukakos, M. Lisowski, U. Bovensiepen, H. Eisaki, and M. Wolf, *Ultrafast Electron Relaxation in Superconducting Bi₂Sr₂CaCu₂O_{8+δ} by Time-Resolved Photoelectron Spectroscopy*, Physical Review Letters **99**, 197001 (2007).
- [Pil00] T. Pillo, J. Hayoz, H. Berger, F. Lévy, L. Schlapbach, and P. Aebi, *Photoemission of bands above the Fermi level: The excitonic insulator phase transition in 1T - TiSe₂*, Physical Review B **61**, 16213 (2000).
- [Por12] M. Porer, J.-M. Ménard, A. Leitenstorfer, R. Huber, R. Degl'Innocenti, S. Zanotto, G. Biasiol, L. Sorba, and A. Tredicucci, *Nonadiabatic switching of a photonic band structure: Ultrastrong light-matter coupling and slow-down of light*, Physical Review B **85**, 081302 (2012).
- [Por14a] M. Porer, U. Leierseder, J.-M. Ménard, H. Dachraoui, L. Mouchliadis, I. E. Perakis, U. Heinzmann, J. Demsar, K. Rossnagel, and R. Huber, *Non-thermal separation of electronic and structural orders in a persisting charge density wave*, Nature Materials **13**, 857–861 (2014).
- [Por14b] M. Porer, J.-M. Ménard, and R. Huber, *Shot noise reduced terahertz detection via spectrally postfiltered electro-optic sampling*, Optics Letters **39**, 2435 (2014).
- [Pro92] B. Proctor and F. Wise, *Quartz prism sequence for reduction of cubic phase in a mode-locked Ti:Al₂O₃ laser*, Optics Letters **17**, 1295 (1992).
- [Psh94] M. S. Pshenichnikov, W. P. de Boeij, and D. A. Wiersma, *Generation of 13-fs, 5-MW pulses from a cavity-dumped Ti:sapphire laser*, Optics Letters **19**, 572 (1994).

- [Pur46] E. M. Purcell, *Proceedings of the American Physical Society*, Phys. Rev. **69**, 674 (1946).
- [Qaz07] M. M. Qazilbash, M. Brehm, B.-G. Chae, P.-C. Ho, G. O. Andreev, B.-J. Kim, S. J. Yun, A. V. Balatsky, M. B. Maple, F. Keilmann, H.-T. Kim, and D. N. Basov, *Mott Transition in VO₂ Revealed by Infrared Spectroscopy and Nano-Imaging*, Science **318**, 1750 (2007).
- [Ram97] A. P. Ramirez, *Colossal magnetoresistance*, Journal of Physics: Condensed Matter **9**, 8171 (1997).
- [Rei07] K. Reimann, *Table-top sources of ultrashort THz pulses*, Reports on Progress in Physics **70**, 1597 (2007).
- [Rem87] G. Rempe, H. Walther, and N. Klein, *Observation of quantum collapse and revival in a one-atom maser*, Physical Review Letters **58**, 353 (1987).
- [Rez06] D. Reznik, L. Pintschovius, M. Ito, S. Iikubo, M. Sato, H. Goka, M. Fujita, K. Yamada, G. D. Gu, and J. M. Tranquada, *Electron-phonon coupling reflecting dynamic charge inhomogeneity in copper oxide superconductors*, Nature **440**, 1170 (2006).
- [Rie76] C. Riekel, *Structure refinement of TiSe₂ by neutron diffraction*, Journal of Solid State Chemistry **17**, 389 (1976).
- [Roh11] T. Rohwer, S. Hellmann, M. Wiesenmayer, C. Sohrt, A. Stange, B. Slomski, A. Carr, Y. Liu, L. M. Avila, M. Kallane, S. Mathias, L. Kipp, K. Rossnagel, and M. Bauer, *Collapse of long-range charge order tracked by time-resolved photoemission at high momenta*, Nature **471**, 490 (2011).
- [Ros02a] E. Rosencher and B. Vinter, *Optoelectronics*, Cambridge University Press (2002).
- [Ros02b] K. Rossnagel, L. Kipp, and M. Skibowski, *Charge-density-wave phase transition in 1T – TiSe₂: Excitonic insulator versus band-type Jahn-Teller mechanism*, Physical Review B **65**, 235101 (2002).
- [Rot00] F. Rotermund, V. Petrov, and F. Noack, *Difference-frequency generation of intense femtosecond pulses in the mid-IR using HgGa₂S₄ and AgGaS₂*, Optics Communications **185**, 177 (2000).
- [Rum06] R. C. Rumpf, *Design and optimization of nano-optical elements by coupling fabrication to optical behavior*, Ph.D. thesis, University of Central Florida (2006).
- [Sai09] R. P. Saichu, I. Mahns, A. Goos, S. Binder, P. May, S. G. Singer, B. Schulz, A. Rusydi, J. Unterhinninghofen, D. Manske, P. Guptasarma, M. S. Williamsen,

- and M. Rübhausen, *Two-Component Dynamics of the Order Parameter of High Temperature $\text{Bi}_2\text{Sr}_2\text{Ca}\text{Cu}_2\text{O}_{8+\delta}$ Superconductors Revealed by Time-Resolved Raman Scattering*, Physical Review Letters **102**, 177004 (2009).
- [Sax09] A. Saxena, *High-Temperature Superconductors*, Springer Series in Materials Science. Springer (2009).
- [Sch94] U. Schlarb and B. Sugg, *Refractive Index of Terbium Gallium Garnet*, Physica Status Solidi (b) **182**, K91 (1994).
- [Sch95] J. Schützmann, S. Tajima, S. Miyamoto, Y. Sato, and R. Hauff, *Doping and temperature dependence of c-axis optical phonons in $\text{YBa}_2\text{Cu}_3\text{O}_y$ single crystals*, Physical Review B **52**, 13665 (1995).
- [Sch03] B. Schenkel, J. Biegert, U. Keller, C. Vozzi, M. Nisoli, G. Sansone, S. Stagira, S. D. Silvestri, and O. Svelto, *Generation of 3.8-fs pulses from adaptive compression of a cascaded hollow fiber supercontinuum*, Optics Letters **28**, 1987 (2003).
- [Sch04] C. A. Schmuttenmaer, *Exploring Dynamics in the Far-Infrared with Terahertz Spectroscopy*, Chemical Reviews **104**, 1759 (2004).
- [Sch11] T. Schwartz, J. A. Hutchison, C. Genet, and T. W. Ebbesen, *Reversible Switching of Ultrastrong Light-Molecule Coupling*, Physical Review Letters **106**, 196405 (2011).
- [Sch14] O. Schubert, M. Hohenleutner, F. Langer, B. Urbanek, C. Lange, U. Huttner, D. Golde, T. Meier, M. Kira, S. W. Koch, and R. Huber, *Sub-cycle control of terahertz high-harmonic generation by dynamical Bloch oscillations*, Nature Photonics **8**, 119 (2014).
- [Sci11] G. Sciaiani and R. J. D. Miller, *Femtosecond electron diffraction: heralding the era of atomically resolved dynamics*, Reports on Progress in Physics **74**, 096101 (2011).
- [Sel08a] A. Sell, A. Leitenstorfer, and R. Huber, *Phase-locked generation and field-resolved detection of widely tunable terahertz pulses with amplitudes exceeding 100 MV/cm*, Optics Letters **33**, 2767 (2008).
- [Sel08b] A. Sell, R. Scheu, A. Leitenstorfer, and R. Huber, *Field-resolved detection of phase-locked infrared transients from a compact Er:fiber system tunable between 55 and 107 THz*, Applied Physics Letters **93**, 251107 (2008).
- [Sel09] A. Sell, G. Krauss, R. Scheu, R. Huber, and A. Leitenstorfer, *8-fs pulses from a compact Er:fiber system: quantitative modeling and experimental implementation*, Optics Express **17**, 1070 (2009).

- [Set07] M. D. Settle, R. J. P. Engelen, M. Salib, A. Michaeli, L. Kuipers, and T. F. Krauss, *Flatband slow light in photonic crystals featuring spatial pulse compression and terahertz bandwidth*, Optics Express **15**, 219 (2007).
- [Sha00] J. Shan, A. S. Weling, E. Knoesel, L. Bartels, M. Bonn, A. Nahata, G. A. Reider, and T. F. Heinz, *Single-shot measurement of terahertz electromagnetic pulses by use of electro-optic sampling*, Optics Letters **25**, 426 (2000).
- [Sip08] B. Sipos, A. F. Kusmartseva, A. Akrap, H. Berger, L. Forro, and E. Tutis, *From Mott state to superconductivity in 1T-TaS₂*, Nature Materials **7**, 960 (2008).
- [Smi88] P. Smith, D. Auston, and M. Nuss, *Subpicosecond photoconducting dipole antennas*, IEEE J. Quantum Electron. **24**, 255 (1988).
- [Sno03] C. Snow, J. Karpus, S. Cooper, T. Kidd, and T.-C. Chiang, *Quantum Melting of the Charge-Density-Wave State in 1T-TiSe₂*, Physical Review Letters **91**, 136402 (2003).
- [Spe91] D. E. Spence, P. N. Kean, and W. Sibbett, *60-fsec pulse generation from a self-mode-locked Ti:sapphire laser*, Optics Letters **16**, 42 (1991).
- [Ste11] G. R. Stewart, *Superconductivity in iron compounds*, Reviews of Modern Physics **83**, 1589 (2011).
- [Str85] D. Strickland and G. Mourou, *Compression of amplified chirped optical pulses*, Optics Communications **56**, 219 (1985).
- [Sud05] A. Suda, M. Hatayama, K. Nagasaka, and K. Midorikawa, *Generation of sub-10-fs, 5-mJ-optical pulses using a hollow fiber with a pressure gradient*, Applied Physics Letters **86**, 111116 (2005).
- [Sug80] S. Sugai, K. Murase, S. Uchida, and S. Tanaka, *Raman studies of lattice dynamics in 1T-TiSe₂*, Solid State Communications **35**, 433 (1980).
- [Tod09] Y. Todorov, A. M. Andrews, I. Sagnes, R. Colombelli, P. Klang, G. Strasser, and C. Sirtori, *Strong Light-Matter Coupling in Subwavelength Metal-Dielectric Microcavities at Terahertz Frequencies*, Physical Review Letters **102**, 186402 (2009).
- [Tod10] Y. Todorov, A. M. Andrews, R. Colombelli, S. De Liberato, C. Ciuti, P. Klang, G. Strasser, and C. Sirtori, *Ultrastrong Light-Matter Coupling Regime with Polariton Dots*, Physical Review Letters **105**, 196402 (2010).
- [Tom05] H. G. Tompkins and E. A. Irene, *Handbook of Ellipsometry*, edited by H. G. Tompkins and E. A. Irene, Springer, (2005) (2005).
- [Ton07] M. Tonouchi, *Cutting-edge terahertz technology*, Nature Photonics **1**, 97 (2007).

- [Tsu00] C. C. Tsuei and J. R. Kirtley, *Pairing symmetry in cuprate superconductors*, Reviews of Modern Physics **72**, 969 (2000).
- [Tur01] A. V. Turukhin, V. S. Sudarshanam, M. S. Shahriar, J. A. Musser, B. S. Ham, and P. R. Hemmer, *Observation of Ultraslow and Stored Light Pulses in a Solid*, Physical Review Letters **88**, 023602 (2001).
- [Ulb11] R. Ulbricht, E. Hendry, J. Shan, T. F. Heinz, and M. Bonn, *Carrier dynamics in semiconductors studied with time-resolved terahertz spectroscopy*, Reviews of Modern Physics **83**, 543 (2011).
- [VH95] D. J. Van Harlingen, *Phase-sensitive tests of the symmetry of the pairing state in the high-temperature superconductors: Evidence for $d_{x^2-y^2}$ symmetry*, Reviews of Modern Physics **67**, 515 (1995).
- [Vla05] Y. A. Vlasov, M. O'Boyle, H. F. Hamann, and S. J. McNab, *Active control of slow light on a chip with photonic crystal waveguides*, Nature **438**, 65 (2005).
- [Wan12] Q. H. Wang, K. Kalantar-Zadeh, A. Kis, J. N. Coleman, and M. S. Strano, *Electronics and optoelectronics of two-dimensional transition metal dichalcogenides*, Nature Nanotechnology **7**, 699 (2012).
- [Web11] F. Weber, S. Rosenkranz, J.-P. Castellan, R. Osborn, G. Karapetrov, R. Hott, R. Heid, K.-P. Bohnen, and A. Alatas, *Electron-Phonon Coupling and the Soft Phonon Mode in $TiSe_2$* , Physical Review Letters **107**, 266401 (2011).
- [Wei92] C. Weisbuch, M. Nishioka, A. Ishikawa, and Y. Arakawa, *Observation of the coupled exciton-photon mode splitting in a semiconductor quantum microcavity*, Physical Review Letters **69**, 3314 (1992).
- [Wes14] N. Westerberg, S. Cacciatori, F. Belgiorno, F. D. Piazza, and D. Faccio, *Experimental quantum cosmology in time-dependent optical media*, New Journal of Physics **16**, 075003 (2014).
- [Wez10a] J. van Wezel, P. Nahai-Williamson, and S. S. Saxena, *An alternative interpretation of recent ARPES measurements on $TiSe_2$* , Europhysics Letters **89**, 47004 (2010).
- [Wez10b] J. van Wezel, P. Nahai-Williamson, and S. S. Saxena, *Exciton-phonon-driven charge density wave in $TiSe_2$* , Physical Review B **81**, 165109 (2010).
- [Wha91] M. H. Whangbo, E. Canadell, P. Foury, and J. P. Pouget, *Hidden Fermi Surface Nesting and Charge Density Wave Instability in Low-Dimensional Metals*, Science **252**, 96 (1991).
- [Wha92] M. H. Whangbo and E. Canadell, *Analogy between the concepts of molecular*

- chemistry and solid-state physics concerning structural instabilities. Electronic origin of the structural modulations in layered transition metal dichalcogenides,* Journal of the American Chemical Society **114**, 9587 (1992).
- [Wil69] J. Wilson and A. Yoffe, *The transition metal dichalcogenides discussion and interpretation of the observed optical, electrical and structural properties*, Advances in Physics **18**, 193 (1969).
- [Wil75] J. Wilson, F. Di Salvo, and S. Mahajan, *Charge-density waves and superlattices in the metallic layered transition metal dichalcogenides*, Advances in Physics **24**, 117 (1975).
- [Wil78a] J. Wilson, A. Barker, F. Salvo, and J. Ditzenberger, *Infrared properties of the semimetal $TiSe_2$* , Physical Review B **18**, 2866 (1978).
- [Wil78b] J. A. Wilson, *Modelling the contrasting semimetallic characters of TiS_2 and $TiSe_2$* , Physica Status Solidi (b) **86**, 11 (1978).
- [Wil11] C. M. Wilson, G. Johansson, A. Pourkabirian, M. Simoen, J. R. Johansson, T. Duty, F. Nori, and P. Delsing, *Observation of the Dynamical Casimir Effect in a Superconducting Circuit*, Nature **479**, 376–379 (2011).
- [Wu87] M. K. Wu, J. R. Ashburn, C. J. Torng, P. H. Hor, R. L. Meng, L. Gao, Z. J. Huang, Y. Q. Wang, and C. W. Chu, *Superconductivity at 93 K in a new mixed-phase $Y\text{-Ba}\text{-Cu}\text{-O}$ compound system at ambient pressure*, Physical Review Letters **58**, 908 (1987).
- [Wu95] Q. Wu and X.-C. Zhang, *Free-space electro-optic sampling of terahertz beams*, Applied Physics Letters **67**, 3523 (1995).
- [Yab89] E. Yablonovitch, *Accelerating reference frame for electromagnetic waves in a rapidly growing plasma: Unruh-Davies-Fulling-DeWitt radiation and the nonadiabatic Casimir effect*, Physical Review Letters **62**, 1742 (1989).
- [Yao97] X. Yao and Y. Shiohara, *Large REBCO single crystals: growth processes and superconducting properties*, Superconductor Science and Technology **10**, 249 (1997).
- [Yok01] T. Yokoya, T. Kiss, A. Chainani, S. Shin, M. Nohara, and H. Takagi, *Fermi Surface Sheet-Dependent Superconductivity in 2H- $NbSe_2$* , Science **294**, 2518 (2001).
- [Yu10] P. Yu and M. Cardona, *Fundamentals of Semiconductors: Physics and Materials Properties*, Graduate Texts in Physics. Springer (2010).
- [Zan10] S. Zanotto, G. Biasiol, R. Degl'Innocenti, L. Sorba, and A. Tredicucci, *In-*

- tersubband polaritons in a one-dimensional surface plasmon photonic crystal*, Applied Physics Letters **97**, 231123 (2010).
- [Zan12] S. Zanotto, R. Degl'Innocenti, L. Sorba, A. Tredicucci, and G. Biasiol, *Analysis of line shapes and strong coupling with intersubband transitions in one-dimensional metallo dielectric photonic crystal slabs*, Physical Review B **85**, 035307 (2012).
- [Zee99] E. Zeek, K. Maginnis, S. Backus, U. Russek, M. Murnane, G. Mourou, H. Kapteyn, and G. Vdovin, *Pulse compression by use of deformable mirrors*, Optics Letters **24**, 493 (1999).
- [Zen13] B. Zenker, H. Fehske, H. Beck, C. Monney, and A. R. Bishop, *Chiral charge order in 1T-TiSe₂: Importance of lattice degrees of freedom*, Physical Review B **88**, 075138 (2013).
- [Zha12] X. Zhang, E. Schneider, G. Taft, H. Kapteyn, M. Murnane, and S. Backus, *Multi-microjoule, MHz repetition rate Ti:sapphire ultrafast regenerative amplifier system*, Optics Express **20**, 7015 (2012).
- [Zhu12] Z. Zhu, Y. Cheng, and U. Schwingenschlögl, *Origin of the charge density wave in 1T-TiSe₂*, Physical Review B **85**, 245133 (2012).
- [Zim78] R. Zimmermann, K. Kilmann, W. D. Kraeft, D. Kremp, and G. Röpke, *Dynamical screening and self-energy of excitons in the electron-hole plasma*, Physica Status Solidi (b) **90**, 175 (1978).
- [Zun78] A. Zunger and A. J. Freeman, *Band structure and lattice instability of TiSe₂*, Physical Review B **17**, 1839 (1978).

Acknowledgments

This work would not have been possible without the help of numerous people and I am grateful to everybody who contributed to its successful completion. Special thanks are due to:

- Prof. Dr. Rupert Huber for giving me the opportunity to pursue several highly interesting projects during my doctoral studies and the freedom to implement my own ideas. Many thanks for the trust he put in me, the continuous support and for being available for inspiring scientific discussions at any time.
- Dr. Jean-Michel Ménard and Dr. Alexej Pashkin for the teamwork in the lab and in publishing the results.
- Prof. Dr. Alfred Leitenstorfer, for his support during the initial period of this work at the University of Konstanz.
- Prof. Dr. Jure Demsar for the interesting and fruitful discussions about non-thermal phases in strongly correlated materials.
- Prof. Dr. Sergey Ganichev for agreeing to referee this work.
- Dr. Kai Rossnagel, Dr. Hatem Dachraoui and Prof. Dr. Ulrich Heinzmann for providing the bulk samples of $1T\text{-TiSe}_2$ and for discussing the experimental results.
- Dr. Simone Zanotto, Dr. Riccardo Degl'Innocenti, Dr. Giorgio Biasol, Prof. Dr. Lucia Sorba and Prof. Dr. Alessandro Tredicucci for the close collaboration in the cavity-polariton project and for fabricating the samples.
- Prof. Dr. Ilias E. Perakis and Dr. Leonidas Mouchliadis for the collaboration in developing the theoretical model of the CDW phase transition in $1T\text{-TiSe}_2$.
- Dr. Markus Beyer, Prof. Dr. Kyungwan Kim, Dr. Adam Dubroka, Prof. Dr. Christian Bernhard, Prof. Dr. Xin Yao, Dr. Yoram Dagan, Dr. Rudi Hackl and Dr. Andreas Erb for their collaboration in the YBCO project.

- Martin Furthmeier for his efforts in establishing and maintaining the laboratory infrastructure and his collaboration in implementing the four-pass amplifier.
- Thomas Maag for his cooperation in establishing the laboratory.
- Ursula Leierseder and Christoph Pöllmann for the collaboration in the lab and the excellent atmosphere in the office.
- Sebastian Baierl, Dr. Tyler Cocker, Max Eisele, Matthias Hohenleutner and Fabian Langer for the excellent working atmosphere, numerous scientific discussions, proof-reading this thesis and the many recreational activities.
- Ulla Franzke for her assistance in all administrative tasks.
- All the other current and former members of the chair of Prof. Huber for the good atmosphere, technical assistance and discussions.
- Christine, for being by my side.